The Development of a SQUID-based Gradiometer

by

Benjamin John Frederick Muller

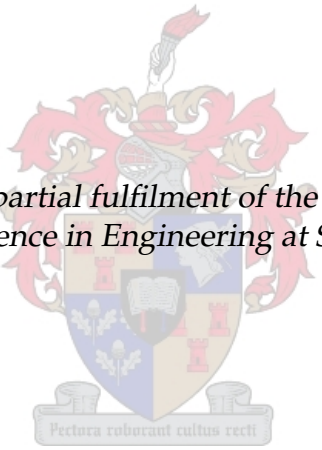

Thesis presented in partial fulfilment of the requirements for the degree of Master of Science in Engineering at Stellenbosch University

Supervisor: Prof. Willem Jacobus Perold
Department of Electrical and Electronic Engineering

March 2010

Declaration

By submitting this thesis electronically, I declare that the entirety of the work contained therein is my own, original work, that I am the owner of the copyright thereof (unless to the extent explicitly otherwise stated) and that I have not previously in its entirety or in part submitted it for obtaining any qualification.

March 2010

Abstract

This thesis presents an attempt at creating a fully functional SQUID for the purposes of a predefined application. The goal of the work is to provide a method of development, primarily utilising the facilities of the Engineering Faculty of the University of Stellenbosch, with minimal assistance from other departments. This method is then analysed and the successes and failures discussed in order to provide guidelines and recommendations for future research.

The device consists of a gradiometric SQUID, as well as electronics which provide the SQUID bias current, output linearisation and output signal filtering. YBCO is used for the superconducting material, allowing the use of liquid nitrogen as coolant which eases the operation and portability of the device. Various methods of creating Josephson junctions are tested, such as constriction bridges using AFM lithography and step-edge junctions, with and without different buffer layers.

Proof of concept simulations demonstrate the viability of the device. Unfortunately, a functional device could not be constructed, mostly due to the design requiring higher levels of resolution and process control than some of the available facilities can provide. Recommendations are provided for future researchers.

Opsomming

Hierdie tesis beskryf 'n poging om 'n volledige funksionele SQUID te vervaardig vir die doeleindes van 'n vasgestelde toepassing. Die doel van die werk is om 'n metode te voorsien wat hoofsaaklik gebruik maak van die fasiliteite van die Ingenieurswese Fakulteit van die Universiteit van Stellenbosch, met minimale hulp van ander departemente. Hierdie metode word dan ondersoek en die suksesse en mislukkings bespreek om riglyne en voorstellings te voorsien vir toekomstige navorsing.

Die toestel bestaan uit 'n gradiometriese SQUID, sowel as elektronika wat voorsiening maak vir voorspanning, uittree-linearisering en 'n uittree-filter. YBCO is as supergeleidende materiaal gebruik, wat die gebruik van vloeibare stikstof as verkoeler moontlik maak en dus die hantering en draagbaarheid van die toestel vergemaklik. Verskillende metodes om Josephson-vlakke te vervaardig is getoets, onder andere vernouingsbrugvlakke deur middel van AFM litografie en stapvlakke met en sonder bufferlae.

Bewys van konsep simulasies demonstreer die lewensvatbaarheid van die toestel. Ongelukkig kon 'n funksionele weergawe van die toestel nie vervaardig word nie, hoofsaaklik as gevolg van die ontwerp wat hoër resolusievlakke en beter prosesbeheer benodig as wat sekere van die beskikbare fasiliteite kan voorsien. Aanbevelings word voorsien vir toekomstige navorsers.

Acknowledgements

I would like to express my sincere gratitude to the following people and organisations who have contributed to making this work possible:

- Prof W. J. Perold as my study leader for his limitless optimism and encouragement.
- Ulrich Büttner for his technical expertise and willingness to assist in any aspect of the laboratory work.
- Akram Elkaseh for his help in getting to understand the deposition and milling processes.
- The National Research Foundation for their financial support.
- The Physics department of the University of Stellenbosch for usage of their PLD.
- Alwyn Botha, Carlo Schenke and Stanley van der Heever for various assistances in and around the laboratories.
- Finally, my family for their endless support and encouragement.

Contents

Declaration i

Abstract ii

Opsomming iii

Acknowledgements iv

Contents v

Abbreviations vii

List of Figures ix

List of Tables xiv

1 Introduction 1
- 1.1 Problem Statement . . . 1
- 1.2 Thesis Overview . . . 2

2 History of Superconductivity 4

3 Theory of Superconductivity 6
- 3.1 Fundamental Observations . . . 6
- 3.2 London Equations . . . 9
- 3.3 Ginzburg-Landau Theory . . . 10
- 3.4 BCS Theory . . . 11
- 3.5 Type II Superconductors . . . 11

4 Josephson Junctions 13
- 4.1 Theory of Josephson Junctions . . . 13
- 4.2 Types of Josephson Junctions . . . 20

5 SQUIDs **25**
5.1 Theory of SQUIDs . . . 25
5.2 Gradiometers . . . 30

6 Electronics **35**
6.1 Flux-locked Loop . . . 35
6.2 Current Source . . . 46
6.3 Output Filter . . . 47

7 Manufacturing of a SQUID **50**
7.1 Photolithography . . . 50
7.2 Thin Film Deposition . . . 53
7.3 Atomic Force Microscopy . . . 58
7.4 Argon Ion Mill . . . 58
7.5 Specific Manufacturing Processes of Different Types of SQUIDs . . . 62
7.6 Buffer Layer . . . 65

8 Results **67**
8.1 YBCO Deposition . . . 67
8.2 Josephson Junctions . . . 69
8.3 Gradiometer Designs . . . 73

9 Conclusions and Recommendations **76**

Appendices **78**

A Gradiometer Schematics **79**

B WRSPICE Code **83**
B.1 Flux-locked Loop Proof of Concept . . . 83
B.2 Output Bandpass Filter . . . 85

C FastHenry Code **89**
C.1 Original G-SQUID . . . 89
C.2 Variant G-SQUID . . . 92

Bibliography **94**

Abbreviations

- AC - Alternating Current
- AFM - Atomic Force Microscope
- APF - Additional Positive Feedback
- BCJ - Bicrystal Junction
- BEJ - Bi-epitaxial Junction
- BSCCO - $Bi_2Sr_2Ca_nCu_{n+1}O_{2n+6-d}$
- DC - Direct Current
- FLL - Flux-locked Loop
- G-SQUID - Gradiometric SQUID
- HTS - High Temperature Superconductors
- IBE/IBM - Ion Beam Etching/Ion Beam Milling
- ICM - Inverted Cylindrical Magnetron
- IJ - Intrinsic Josephson Junction
- JJ - Josephson Junction
- LTS - Low Temperature Superconductors
- MQS - Magnetoquasistatic
- PBCO - $P_1Ba_2Cu_3O_{7-\delta}$
- PLD - Pulsed Laser Deposition
- RCSJ - Resistively and Capacitively Shunted Junction
- RF - Radio Frequency

- RPM - Revolutions per Minute
- SEJ - Step-edge Junction
- SIS - Superconductor/Insulator/Superconductor
- SLG - Single-layer Thin Film Gradiometer
- SQUID - Superconducting Quantum Interference Device
- STM - Scanning Tunneling Microscope
- UV - Ultra-violet Light
- VLSI - Very-large-scale Integration
- YBCO - $Y_1Ba_2Cu_3O_{7-\delta}$

List of Figures

3.1 Temperature dependance of resistivity of a normal metal (dashed line) as given by Mattheissen's rule, and of a superconductor (solid line). . . . 7
3.2 Temperature dependance of the critical magnetic field. The normal and superconductive state is above and below $H_c(T)$ respectively. 8

4.1 Dependence of the critical current of a Josephson junction as a function of flux threading the junction. 15
4.2 The variation of current density in a Josephson junction for different values of flux penetrating the junction. The solid arrows indicate the current density and direction. 16
4.3 The circuit diagram of a Josephson junction as according to the RCSJ model. The three channels are each represented by an appropriate circuit element. 17
4.4 I–V behaviour of a fully overdamped (solid line) and highly underdamped (broken line) Josephson junction. 18
4.5 I–V behaviour of a Josephson junction with $\beta_c \approx 50$. 19
4.6 Ideal voltage source with zero internal impedance. 19
4.7 I–V behaviour according to the AC voltage source model. 21
4.8 Ideal current source with infinite internal impedance. 21
4.9 A simulation of the I–V behaviour of a Josephson junction according to the AC current source model. The Shapiro steps are clearly visible. . . . 22
4.10 A few examples of Josephson junction topologies: (a) nanobridge, (b) step-edge and (c) bicrystal junction. The broken lines in (b) and (c) indicate the grain boundaries where the junctions will form. The arrows in (c) indicate the different grain angles that result in a grain boundary. In each case, blue represents the crystal substrate, and green represents the superconducting thin film. 23

5.1 The DC SQUID loop. The SQUID is biased with a DC current I_t, and threaded by a magnetic flux Φ. 26

5.2 The modulation of maximum critical current of a SQUID as a function of externally applied flux. 27
5.3 The I–V characteristics of a SQUID threaded by integer and half-integral numbers of flux quanta. 28
5.4 Dependence of the maximum and minimum values of the critical current of a SQUID as a function of the SQUID loop inductance. These values determine the modulation depth achievable from an external magnetic field. 29
5.5 Variation of SQUID voltage due to the modulation of the critical current from externally applied flux. 30
5.6 Two common pickup loop configurations for SQUID gradiometers, namely (a) axial and (b) planar. 31
5.7 The layout schematic of the G-SQUID. The broken line indicate the grain boundary where the Josephson junctions will form. The inner pads are connected to ground and the tracks going out to the sides connect the SQUID to the pickup loops. 32
5.8 An alternative layout schematic of the G-SQUID. The design is intended for use with a single grain boundary, indicated by the broken line, forming both junctions. 33

6.1 The V–Φ characteristic of a SQUID. 35
6.2 The direct readout flux-locked loop. The SQUID and the feedback coil are both cooled at cryogenic temperatures. 36
6.3 The flux modulation readout flux-locked loop. The SQUID, feedback coil and step-up transformer are cooled at cryogenic temperatures. . . . 37
6.4 The V–Φ characteristic of a SQUID with a flux modulation FLL. The output voltage of the SQUID is shown on the right. The SQUID is switched between working points W^+ and W^-, resulting in an applied flux being reflected as a square wave voltage either in phase or out of phase with the modulation signal, depending on whether the applied flux was positive or negative. 37
6.5 The direct readout flux-locked loop with additional positive feedback. The SQUID, feedback coil, APF coil and resistor are all cooled at cryogenic temperatures. 38
6.6 The V–Φ characteristic of a SQUID with a FLL with APF. The effect of the APF increases the transfer coefficient on the positive slope of the characteristic, and lowers it on the negative slope. 39
6.7 The equivalent small-signal amplifier which can be used to represent the APF circuit. 39

6.8 The effects of applied flux to the V–Φ characteristic of the SQUID compared to the effects of I_c,R_n fluctuations for a positive SQUID bias. The solid lines indicate the unaltered characteristic and the broken lines indicate the affected cases. 40
6.9 The effects of applied flux to the V–Φ characteristic of the SQUID compared to the effects of I_c,R_n fluctuations for both a positive and negative SQUID bias. The solid lines indicate the unaltered characteristic and the broken lines indicate the affected cases. 41
6.10 The schematic of the FLL proof of concept simulation. 42
6.11 Simulation of a direct readout FLL with APF. The external excitation signal represents a 3 μT magnetic field oscillating at 2.5 MHz. 44
6.12 Simulation of a direct readout FLL with APF. The external excitation signal represents a triangle wave oscillating at 1 MHz. 45
6.13 A Wilson current source. The three transistors Q_1, Q_2 and Q_3 are assumed to be identical. 46
6.14 A narrowband bandpass filter. 47
6.15 The output of the bandpass filter as a function of frequency. The unity gain at 50 Hz, although less than expected, is still sufficient for the SQUID output. 48

7.1 The basic steps involved in the photolithography process. In all cases, the substrate is indicated in blue, the superconducting film in green, and the photoresist in red. The mask is indicated in (b) as a transparent plate with an opaque pattern. The broken lines indicate the UV radiation. Finally, the exposed parts of the resist is indicated in orange. 51
7.2 A basic DC sputtering configuration. 54
7.3 The inverted cylindrical magnetron (ICM) sputtering deposition chamber used to deposit YBCO at the Engineering Faculty. 55
7.4 Basic operation of a PLD. 56
7.5 The pulsed laser deposition system used at the University of Stellenbosch. 57
7.6 The Nanosurf easyScan 2 AFM. 59
7.7 A schematic of an ion mill in a triode configuration using an RF plasma source [1]. 60
7.8 Examples of the various imperfections that may occur during etching. In all examples, the substrate is indicated in blue, and the mask in green. 61
7.9 The Argon Ion Mill used at the University of Stellenbosch. 62
7.10 The important angles during step-edge fabrication. 63
7.11 A buffer layer is used to create the epitaxial template for a step-edge junction. 65

8.1 The substrate heater profile used during YBCO deposition. 67
8.2 Three YBCO samples deposited under the same conditions. From the reflections it can be seen that the sample surfaces vary greatly, despite being deposited under identical conditions. 68
8.3 The susceptibility tests of the three samples shown in Figure 8.2. The susceptibility meter had faulty temperature sensor circuitry, resulting in incorrect temperature measurements below 115 K. 69
8.4 AFM scan showing the step profile of an early PBCO sample intended for use with the original G-SQUID design. 70
8.5 AFM scan showing the step profile of an early PBCO sample intended for use with the alternative G-SQUID design. 70
8.6 An AFM surface scan of a sample in which a constriction junction is scratched. The junction is located in the centre of the blue rectangle, the area of which exhibits significant image noise compared to the area indicated in green. 72
8.7 One of the scratching test samples before and after milling. 72
8.8 The difference between the two levels of focus required when aligning the circuit pattern with the step. The incorrect version of the G-SQUID was unintentionally used in this alignment, however the purpose of the image was to demonstrate the difficulty of the alignment, which is still the same. 73
8.9 Here the step is directly below the pattern in the centre. The blurring effect renders proper alignment of the step to the pattern impossible. Even at higher magnification the step cannot be seen. 74
8.10 The alternative G-SQUID design is also affected by the same problem. Here the step must remain in the centre of the two tracks that connect the SQUID loop to the pickup loop. The step is currently shown crossing the rightmost pad. 74
8.11 The result of attempting to align the mask required for silver pad deposition with the YBCO pattern. 75

A.1 Dimensions of the original G-SQUID design. The tracks extending toward the left and right connect the SQUID loop to the pickup loop. . . . 79
A.2 Dimensions of the variant G-SQUID design. The tracks extending toward the left and right connect the SQUID loop to the pickup loop. . . . 80
A.3 Schematic of the pickup and feedback loops. The outermost and innermost feedback loops are used for the APF and the FLL respectively. Either SQUID is located in the centre of the layout. 81

A.4 Dimensions of the pickup and feedback loops, as well as the connection pads. The track extending to the right connects the pickup loop to the SQUID loop. Both feedback loops are 100 μm wide and 50 μm apart. The pickup loop is 1 mm wide. 82

List of Tables

6.1 The mutual inductance coupling factors of the schematic in Figure 6.10. 43
6.2 The final scaled values of the bandpass filter. 49

7.1 Energy requirements of different effects of ion bombardment. 59
7.2 General parameter set used during testing of photoresist AFM constriction junctions. 64

Chapter 1

Introduction

For many years, SQUIDs were known as the most sensitive magnetic field sensors, achieving sensitivity levels of 1 fT $Hz^{-1/2}$. Only recently have spin-exchange relaxation-free (SERF) atomic magnetometers proven to be potentially more sensitive, reaching levels of 0.54 fT $Hz^{-1/2}$ [2]. This attribute allows the detection of magnetic fields as weak as that exhibited from the brain and heart, however it also affords the opportunity to detect fields that can already be sensed from standard devices, but from greater ranges. In cases where sufficient detection would require proximity to hazards using standard magnetic field sensors, the extra range that can be provided from SQUID detectors may prove to be an indispensable asset. Such cases would typically require the SQUID to be operated in unshielded environments, therefore, proper SQUID layout and electronic design is critical.

1.1 Problem Statement

Although Josephson junctions have been successfully created at the University of Stellenbosch, no one has managed to manufacture a fully functional SQUID yet. Two goals are set in this thesis:

- Design and manufacture a complete SQUID for the purposes of a specific application.
- Manufacture the entire device using only the facilities at the Engineering Faculty of the University of Stellenbosch.

The application for which the SQUID is to be designed, is the detection of 50 Hz currents in overhead power transmission lines. This will require that the device be portable and easily used. Therefore, the design must eliminate unnecessary equipment, such as complex cryocoolers, shielding, and power supplies. In order to

compensate for the lack of shielding, the SQUID is designed to be gradiometric. This will only measure the gradients of magnetic fields, ignoring static fields such as the earth's magnetic field, or long distance interference. An output bandpass filter will also help in signal selectivity. Further electronics, such as a constant current source should allow the device to be operated from a simple power source, such as a 9 V battery.

The reason for the second goal is to determine the viability of creating fully operational SQUIDs using the facilities immediately available. These facilities include an ICM, argon ion mill, AFM, cryocooler for testing and the facilities for a complete photolithography process. A PLD for deposition and a laser for constriction junction fabrication is available, but only from other departments, which slows the overall process.

Finally, the choice of YBCO as a superconductor allows the use of liquid nitrogen as coolant, which is easily aquired and utilised.

1.2 Thesis Overview

The following is an overview of the rest of this thesis:

- *Chapter 2 (History of Superconductivity)* — A brief explanation of the history of superconductivity is given.
- *Chapter 3 (Theory of Superconductivity)* — This chapter provides an explanation of basic superconductor theory, including important theories such as the London equations, BCS theory, and type II superconductors.
- *Chapter 4 (Josephson Junctions)* — The theory of Josephson junctions are explained in this chapter, followed by an overview of different Josephson junction types.
- *Chapter 5 (SQUIDs)* — This chapter discusses SQUID theory, as well as the concept and design of gradiometric SQUIDs.
- *Chapter 6 (Electronics)* — The supporting electronics for SQUID devices are detailed in this chapter. The components discussed are the biasing current source, the flux-locked loop, and the output filter.
- *Chapter 7 (Manufacturing of a SQUID)* — This chapter explains the various processes involved with the manufacture of a SQUID, including thin film deposition, photolithography, and milling, as well as the various methods of Josephson junction creation.

- *Chapter 8 (Results)* — The results of the various attempts at Josephson junction creation are discussed in this chapter, as well as a summary of the problems that were encountered in the manufacturing processes.

- *Chapter 9 (Conclusions and Recommendations)* — This chapter presents the conclusions that were drawn from the results of the previous chapter. Finally, recommendations for future researchers are provided based on these conclusions.

Chapter 2

History of Superconductivity

The events that led to the discovery of superconductivity can be traced back to 10 July 1908. It was then that Heike Kammerlingh Onnes succeeded in liquefying helium. This allowed him to investigate the electrical resistance of pure metals at very low temperatures. Mercury was among the purest of metals that Onnes could obtain, due to it being a liquid at room temperature and, thus, being able to redistill it multiple times to increase its purity. Initial results of the experiments on mercury were as predicted. The resistance decreased as the temperature dropped. Once the temperature reached 4.2 K, which is the temperature at which helium becomes a liquid, the resistance suddenly dropped to zero.

At first, this was attributed to a short somewhere in the system, however, repeated experiments with differing configurations all yielded the same results. It was confirmed not to be a short when a laboratory assistant that was meant to monitor and keep the temperature below 4.2 K, fell asleep and allowed the temperature to rise. Once this happened, the resistance reappeared. In order to eliminate the possibility that the effect was somehow caused by the helium liquefying, similar experiments were performed on lead and tin, which showed the same results at 7.2 K and 3.7 K respectively. The temperature at which the effect occurs was named the *critical temperature* (T_c), and the effect was named *superconductivity*. Onnes received the Nobel prize in 1913 for the discovery of superconductivity and the liquefaction of helium.

Onnes attempted to find uses for superconductivity, however, he discovered another effect that severely impacted its usefulness. He found that magnetic fields above a certain field strength destroys a material's superconductivity. This value became known as the *critical magnetic field* (H_c), and is different for each material. Onnes realised that for superconductivity to become truly useful, T_c and H_c had to be increased.

In the search for more superconducting elements, it was found that the strong

magnetic fields found in ferromagnetic elements would prevent such elements from becoming superconductive. Noble metals, such as copper, gold or silver, showed no evidence of superconductivity either [3].

1933 heralded the discovery of another interesting effect. W. Meissner and R. Oschenfield observed that superconductors expel any applied magnetic fields while in the superconducting state. Superconductivity was thus also a reaction to an external magnetic field. This phenomenon was called the *Meissner effect*. Since then, proving a material to possess superconducting qualities required that the material obtain both zero resistance and the Meissner effect when it is cooled below its critical temperature [4].

In 1935, Fritz and Heinz London attempted to formulate an emperically based, phenomenological model of superconductivity called the London theory [5]. Vitaly Ginzburg and Lev Landau extended this theory in 1950 and introduced the idea of an order parameter and the concept of a coherence length.

It was only in 1957 that Bardeen, Cooper and Schrieffer formulated a theory that could describe all the known features of superconductivity [3]. It was named the BCS theory and its formulation earned them the Nobel Prize in 1972 [6].

Up until 1986, superconductivity could only be obtained at very low temperatures, with a record high of 23.2 K for a Nb_3Ge compound in 1973 [7]. In 1986, Alex Müller and George Bednorz first observed high-temperature superconductivity when they found that a lanthanum-barium-copper-oxide compound exhibited superconductive properties in the 30 K range [8]. This earned them the Nobel prize in physics in 1987. To date, this is still the shortest time between a discovery and a Nobel award. The observation came particularly unexpected since scientists did not really expect superconductive properties in brittle copper-oxides [7].

Another important breakthrough in the search for higher critical temperatures happened in 1987 when Wu et al discovered that a certain yttrium-barium-copper-oxide compound had a critical temperature of 93 K and could thus be cooled using liquid nitrogen (77 K) [9]. The specific compound, $YBa_2Cu_3O_7$, is commonly referred to as YBCO [7] and is the most commonly used high-T_c superconductor today.

Kresin et al predicted an upper limit to cuprate superconductivity at approximately 160 – 170 K, but not superconductivity in general [10]. Therefore, the possibility of room temperature superconductivity should be a driving source for researchers for many more years.

Chapter 3

Theory of Superconductivity

3.1 Fundamental Observations

The phenomenon of superconductivity has two distinct characteristics: Superconductors exhibit zero resistivity and perfect diamagnetism. The resistivity of a normal metal is caused by the scattering of electrons. This is due to collisions between electrons as well as elementary excitations in the system such as lattice vibrations, also known as phonons. Defects in the material such as impurities or grain boundaries can also be the source of resistance. The total resistivity of a material can be described by *Mattheissen's rule*

$$\rho(T) = \rho_i + \rho_{def} \tag{3.1.1}$$

where ρ_i and ρ_{def} is the resistivity caused by scattering and defects respectively.

According to the Drude model, ρ_i can be described as

$$\rho_i(T) = \frac{m}{ne^2\tau} \tag{3.1.2}$$

where m is the electron mass, n is the electron density, e is the elementary electron charge and τ is the mean time between electron collisions, which is temperature dependant. This description of ρ_i can be seen in Figure 3.1 as the dashed line [11]. Superconductors, however, do not exhibit this behaviour. Instead, it exhibits the behaviour as displayed by the solid line. At a specific temperature T_c, known as the *critical temperature*, the resistivity of the superconductor abruptly drops to zero. This state is known as *perfect conductivity*. Experiments to detect any resistance have been limited to the sensitivity of modern testing equipment, and is indeed remarkably small, at least in the order of 10^{-24} Ωcm. By comparison, high purity copper has a resistivity in the order of 10^{-9} Ωcm [12].

Another method of demonstrating the absence of resistance is to induce a current in a superconductive ring. The experiment is performed as follows: A closed

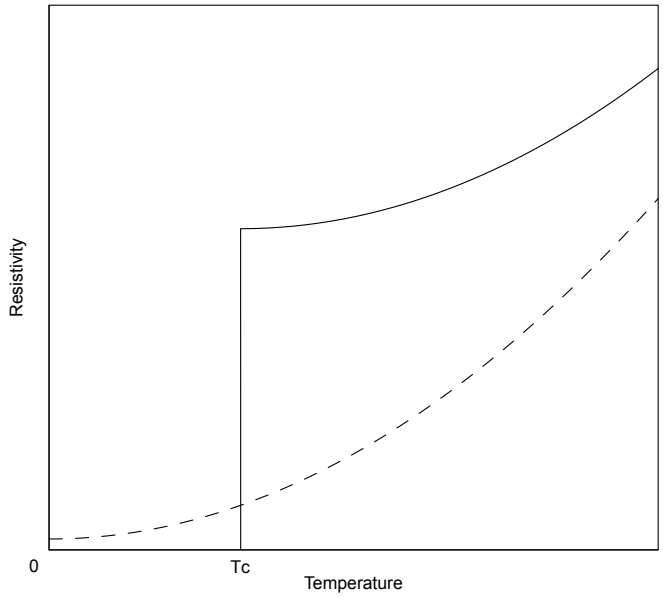

Figure 3.1: Temperature dependance of resistivity of a normal metal (dashed line) as given by Mattheissen's rule, and of a superconductor (solid line).

ring of superconductive material is subjected to an exterior magnetic field, while $T > T_c$. The temperature of the ring is then lowered to below T_c, after which the external field is removed. This decrease in magnetic flux will induce a current in the ring, according to Faraday's law of electromagnetic induction. The current will induce its own magnetic flux, which will prevent further decrease of the flux through the centre of the ring. Normally, such flux would decay with a time constant of L/R, however, since $R = 0$, the decay time is infinite. Thus, the flux is locked in the centre of the ring. Attempts to measure any decrease in the magnetic field and, by extension, current flow using nuclear resonance indicate a characteristic decay time of at least 10^5 years, and in many circumstances it can be expected that no change in current or field will occur in $10^{10^{10}}$ years [13].

This experiment has lead to an important observation. It is reasonable to assume that the trapped flux would be of any value, however, experiments have shown that the trapped flux are always integer multiples of 2.067×10^{-15} Wb. This specific value is known as the *magnetic flux quantum*, which can also be calculated as $\Phi_0 = h/2e$ [11].

Once in a superconductive state, raising the temperature of the material is not the only way to remove the superconductivity. Subjecting the material to a strong

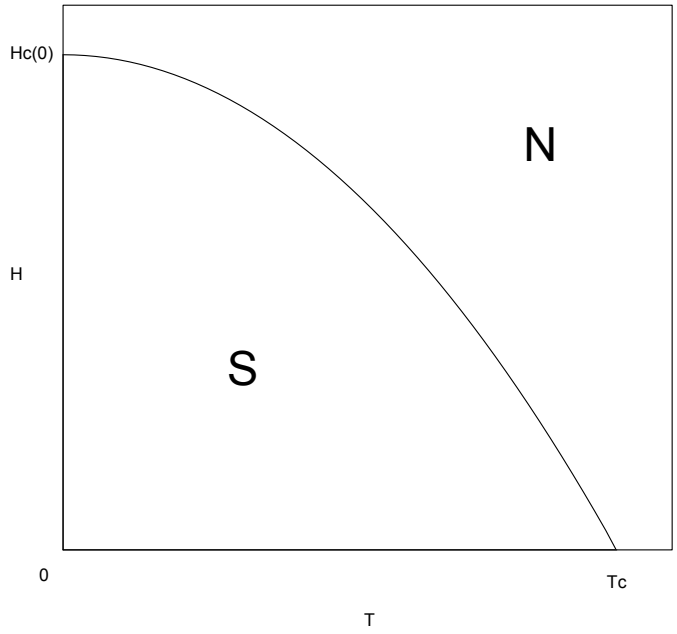

Figure 3.2: Temperature dependance of the critical magnetic field. The normal and superconductive state is above and below $H_c(T)$ respectively.

enough magnetic field will also return it to the normal state. This field is known as the *critical magnetic field*, H_c. The temperature dependance of H_c can be accurately described by the empirical formula

$$H_c(T) = H_c(0)[1 - (T/T_c)^2] \tag{3.1.3}$$

where $H_c(0)$ is an extrapolation of a given material's critical field to absolute zero [12]. The temperature dependance is shown in Figure 3.2.

As mentioned earlier, zero resistivity is one of two characteristics of superconductors. The other, perfect diamagnetism, is what seperates superconductors from perfect conductors. One can predict the magnetic behaviour of a perfect conductor by considering Ohm's law $\mathbf{E} = \rho\mathbf{J}$ and Faraday's law $\nabla \times \mathbf{E} = \partial\mathbf{B}/\partial t$. Since, for a perfect conductor, $\rho = 0$, it follows that

$$\mathbf{E} = 0, \tag{3.1.4}$$

$$\nabla \times \mathbf{E} = 0, \tag{3.1.5}$$

$$\frac{\partial \mathbf{B}}{\partial t} = 0. \tag{3.1.6}$$

If a superconductor was merely a perfect conductor, then it would trap any existing flux penetrating the material when it is cooled below T_c. This is, however, not the

case.

Superconductors only obey (3.1.6) when initially not subjected to any magnetic field at the time of becoming superconductive. If a superconductor was subjected to a magnetic field at the time, then it will not trap the flux as predicted by (3.1.6), but will expel it instead [12]. Surface currents will form which will generate opposing magnetic fields. This is known as the *Meissner-Ochsenfeld effect* [14].

3.2 London Equations

The London equations are used to describe superconductivity on a phenomenological level. The equations were not derived in a typical sense, but formulated from intuition for the purposes of describing the physical phenomenon.

The Drude model for electrical conductivity, which describes electron motion using classical mechanics, can be written as

$$m\frac{d\mathbf{v}}{dt} = e\mathbf{E} - \frac{m\mathbf{v}}{\tau} \tag{3.2.1}$$

where $\mathbf{v}$ is the average drift velocity of the electrons and τ is the mean time for the electron drift velocity to reach zero due to scattering from defects in the material. The Drude model leads to a specific formulation of Ohm's law:

$$\mathbf{J} = \frac{ne^2\tau}{m}\mathbf{E}. \tag{3.2.2}$$

Considering that a current can be induced in a superconductor without generating a potential difference across it, one can postulate that a certain density of charge carriers n_s does not exhibit the scattering term in (3.2.1). Therefore, for these carriers, $\tau \to \infty$ [13]. One can now rewrite the Drude model for these superconductive carriers as

$$m\frac{d\mathbf{v}_s}{dt} = e\mathbf{E}. \tag{3.2.3}$$

Substituting the supercurrent density, $\mathbf{j}_s = n_s e\mathbf{v}_s$, into Equation (3.2.3), it follows that

$$\mathbf{E} = \frac{d}{dt}\left[\frac{m}{n_s e^2}\mathbf{j}_s\right], \tag{3.2.4}$$

$$= \frac{d}{dt}\left(\Lambda\mathbf{j}_s\right) \tag{3.2.5}$$

where $\Lambda = m/(n_s e^2)$. This is known as the first London equation, or simply, London I [12].

In order to attain the second London equation, one starts with the curl of Ampère's law:

$$\nabla \times \nabla \times \mathbf{H} = \nabla \times \mathbf{J}, \tag{3.2.6}$$

$$-\nabla^2\mathbf{H} = \nabla \times \mathbf{J} \tag{3.2.7}$$

Applying the time derivative and substituting (3.2.5) yields

$$-\nabla^2 \frac{\partial \mathbf{H}}{\partial t} = \nabla \times \frac{\partial \mathbf{J}}{\partial t}, \tag{3.2.8}$$

$$= \nabla \times \mathbf{E} \cdot \frac{1}{\Lambda}. \tag{3.2.9}$$

Finally, applying the Maxwell-Farady equation yields

$$-\nabla^2 \frac{\partial \mathbf{H}}{\partial t} = -\frac{\partial \mathbf{H}}{\partial t} \cdot \frac{\mu_0}{\Lambda}, \tag{3.2.10}$$

$$\left(\frac{\mu_0}{\Lambda} - \nabla^2\right) \frac{\partial \mathbf{H}}{\partial t} = 0. \tag{3.2.11}$$

It is simple to see that, for a stationary field, Equation (3.2.11) can be written as

$$\left(\frac{\mu_0}{\Lambda} - \nabla^2\right) \mathbf{H} = 0, \tag{3.2.12}$$

however, in order to comply with the Meissner-Ochsenfeld effect, assume that this expression holds for all frequencies. Applying the vector identity $-\nabla^2 \mathbf{H} = \nabla \times \nabla \times \mathbf{H}$, Equation (3.2.12) can then be written as

$$\nabla \times \nabla \times \mathbf{H} = -\frac{\mu_0}{\Lambda} \mathbf{H}, \tag{3.2.13}$$

which, using the MQS form of Ampère's law, can then be written as

$$\nabla \times \mathbf{J} = \frac{\mu_0 \mathbf{H}}{\Lambda}, \tag{3.2.14}$$

$$\nabla \times (\Lambda \mathbf{J}) = -\mathbf{B}. \tag{3.2.15}$$

This is known as the second London equation, or London II. Solving Equation (3.2.12) for different situations yields a characteristic length λ, defined as

$$\lambda = \sqrt{\frac{\Lambda}{\mu_0}}. \tag{3.2.16}$$

This is known as the *London penetration depth* and is an indication of how far into a superconductor a magnetic field can penetrate. It is similar to the magnetic skin depth parameter δ, but is not frequency dependant [15].

3.3 Ginzburg-Landau Theory

The Ginzburg-Landau theory is also phenomenological, however, it contains quantum mechanics as part of the description of superconductivity phenomena. A single parameter wavefunction $\boldsymbol{\psi}(\mathbf{r})$ is assigned to all superconductive electrons as an order parameter. The idea expressed by the theory is that n_s identical electrons behaving coherently can be described by a single wavefunction of only one

spatial coordinate. The local density of superconductive electrons can be described as $n_s = |\psi(\mathbf{r})|^2$ [12].

The theory allows two conditions to be treated that could not be addressed via the London equations, namely, the non-linear effects of fields strong enough to change n_s, and the spatial variation of n_s. A new characteristic length parameter $\xi(T)$ is introduced, known as the *Ginzburg-Landau coherence length*, which describes the distance over which $\psi(\mathbf{r})$ can vary without an undue increase in energy [13].

Another important parameter is $\kappa = \lambda/\xi$, known as the *Ginzburg-Landau parameter* and can be used to describe the type of a superconductor (discussed below). Typical values of λ and ξ of classic (Type I) superconductors are approximately 500 Å and 3000 Å respectively, leading to a typical value of $\kappa < 1$ [13].

3.4 BCS Theory

The London and GL theories collectively give a good description of the behaviour of a superconductor, however, they do not give a reason. Being formulated from observed phenomena, the theories do not explain the physics governing superconductors. Such an explanation is given by the BCS theory.

Once its temperature drops below T_c, the supercurrent of a superconductor is considered to consist of Cooper pairs. Cooper pairs are electron pairs that are bound by an attractive force due to electron-phonon interactions, which is also stronger than the Coulomb repulsion force. Such a pair has a charge of $2e$. The two electrons have opposite spin directions, thus zero total spin, and can therefore be represented as a Bose particle. The further the temperature is below T_c, the more difficult it is for such a particle to become scattered. Thus the condensate of the particles become superfluid.

The pairing of electrons due to interactions with phonons may seem counter-intuitive at first, as intrinsic phonons decrease at lower temperatures. A pair is formed when an electron itself creates a phonon, which is then absorbed by the second electron [12].

3.5 Type II Superconductors

As previously mentioned, classic superconductors have a GL parameter value of $\kappa < 1$. Alexei Abrikosov investigated the cases where $\kappa \gg 1$ and found behaviour different enough to warrant a new class of superconductors, namely, Type II superconductors. The seperation between Type I and II was found to be at $\kappa = 1/\sqrt{2}$. The most prominent difference between the two types is that instead of losing superconductivity when subjected to a magnetic field of field strength $H > H_c$, Type

II superconductors exhibit gradual flux penetration starting from a lower critical field H_{c1}, increasing up to an upper critical field H_{c2}, after which superconductivity disappears. H_{c2} can be significantly larger than typical values of H_c for Type I superconductors. Between H_{c1} and H_{c2} the superconductor is in a mixed state, also known as the *Schubnikov phase* [13, 16].

While in the mixed state, the superconductor is no longer perfectly diamagnetic. Flux penetrates the material as vortex filaments. Each vortex has a radius of order ξ. The cores of the vortices are normal regions, each carrying exactly one flux quantum. The vortices form in a triangular lattice. Once the external magnetic field reaches $H > H_{c2}$, the vortex density has become so high that the cores overlap, and the entire interior of the material has become a normal region. At this point, the superconductivity is lost [12].

Chapter 4

Josephson Junctions

The active device of superconductor electronics is known as a Josephson junction (JJ). It is described as a junction between two superconductive electrodes that is weak enough to allow a slight overlap of the present electron pair wavefunctions. The most prominent characteristic of such a junction is that electron pairs can pass through it without requiring an applied voltage, and that one can pass a current up to a certain critical value through the junction without generating a voltage across it.

4.1 Theory of Josephson Junctions

4.1.1 Fundamental Relations

The tunneling current of a junction is dependent on the phase difference between the two wavefunctions. These wavefunctions can be presented as

$$\boldsymbol{\psi} = |\psi(\mathbf{r})|\, e^{i\theta(\mathbf{r})}. \tag{4.1.1}$$

If two superconductive electrodes are brought close enough, the two wavefunctions will couple, reducing the system energy. At any arbitrary location in the plane of a junction, the time evolution of the wavefunctions at each side of the junction can be written as

$$i\hbar\frac{\partial\psi_1}{\partial t} = U_1\psi_1 + K\psi_2 \tag{4.1.2}$$

$$i\hbar\frac{\partial\psi_2}{\partial t} = U_2\psi_2 + K\psi_1 \tag{4.1.3}$$

where U_1 and U_2 represent the energies of the wavefunctions, and K is a coupling constant representing interaction between the wavefunctions.

Assume now that a voltage e^*V is applied over the junction, where $e^* = -2e$ is the charge of an electron pair. This will impose an energy difference across the

junction of $e^*V = (U_2 - U_1)$. Taking the zero of energy midway between U_1 and U_2, (4.1.2) and (4.1.3) can be written as

$$i\hbar\frac{\partial\psi_1}{\partial t} = \frac{-e^*V}{2}\psi_1 + K\psi_2 \tag{4.1.4}$$

$$i\hbar\frac{\partial\psi_2}{\partial t} = \frac{-e^*V}{2}\psi_2 + K\psi_1. \tag{4.1.5}$$

The wavefunctions can be further expanded by expressing them as $\psi_k = \sqrt{(n^*_{sk})}e^{i\theta_k}$, where k = 1 or 2, and seperating the real and imaginary parts into

$$\frac{\partial n^*_{s1}}{\partial t} = \frac{2}{\hbar}K\sqrt{n^*_{s1}n^*_{s2}}\sin\phi \tag{4.1.6}$$

$$\frac{\partial n^*_{s2}}{\partial t} = -\frac{2}{\hbar}K\sqrt{n^*_{s1}n^*_{s2}}\sin\phi \tag{4.1.7}$$

$$\frac{\partial\theta_1}{\partial t} = -\frac{K}{\hbar}\sqrt{\frac{n^*_{s2}}{n^*_{s1}}}\cos\phi + \frac{e^*V}{2\hbar} \tag{4.1.8}$$

$$\frac{\partial\theta_2}{\partial t} = -\frac{K}{\hbar}\sqrt{\frac{n^*_{s1}}{n^*_{s2}}}\cos\phi - \frac{e^*V}{2\hbar} \tag{4.1.9}$$

where $\phi = \theta_2 - \theta_1$. Equations (4.1.6) and (4.1.7) indicate that the pair density increases and decreases on the two respective sides of the junction at the same rate. This would create a charge imbalance, however, the balance is negated by the current flowing through the junction. Therefore, from (4.1.6) and (4.1.7) it can be deduced that

$$J = J_c\sin\phi \tag{4.1.10}$$

where $J_c = \frac{2}{\hbar}K\sqrt{n^*_{s1}n^*_{s2}}$ is the critical current density. Considering for simplicity that $n^*_{s1} = n^*_{s2}$, Equations (4.1.8) and (4.1.9) can be subtracted from each other to attain

$$\frac{\partial\phi}{\partial t} = \frac{2e}{\hbar}V. \tag{4.1.11}$$

Equations (4.1.10) and (4.1.11) are known as the Josephson relations.

With no applied voltage across the junction, the phase difference and, by extension, the current in the junction is constant. Applying a DC voltage, however, yields

$$J = J_c\sin\left(\frac{2e}{\hbar}Vt + \phi_0\right) \tag{4.1.12}$$

where Equation (4.1.11) has been integrated and substituted into Equation (4.1.10). From (4.1.12) it is evident that an AC component will result with frequency $\frac{1}{2\pi}\cdot\frac{2e}{\hbar}V = 483.6\times10^{12}$ Hz/V [17].

4.1.2 Magnetic Effects

The critical current I_c of a Josephson junction is not necessarily uniform. In a magnetic field I_c varies as

$$I_c(\Phi_J) = I_c(0)\left|\frac{\sin\left(\frac{\pi\Phi_J}{\Phi_0}\right)}{\frac{\pi\Phi_J}{\Phi_0}}\right| \tag{4.1.13}$$

where Φ_J is the flux penetrating the junction, for the simple case of an initially uniform distribution of zero voltage current density across the entire junction when $\Phi_J = 0$. This variation of I_c is shown in Figure 4.1.

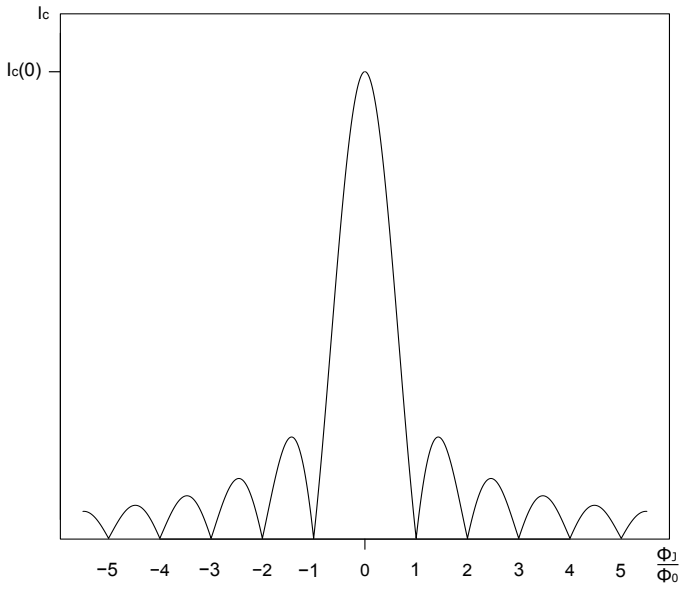

Figure 4.1: Dependence of the critical current of a Josephson junction as a function of flux threading the junction.

A more physical depiction is given in Figure 4.2. In part (a), where no magnetic field is applied to the junction, the current distribution is uniform. The junction in part (b) is threaded by one half of a flux quantum. Here the density starts to vary and the total I_c is reduced as a result. Part (c) shows a junction threaded by one flux quantum. This junction has as much current flowing upward as it does downward, resulting in a circulating current and zero net I_c. Larger integer multiples of Φ_0 will result in more complete circulations, keeping I_c at zero, as seen in Figure 4.1. In part

(d), the junction is threaded by $1.5\Phi_0$ of magnetic flux, further demonstrating the pattern that the current density follows [17].

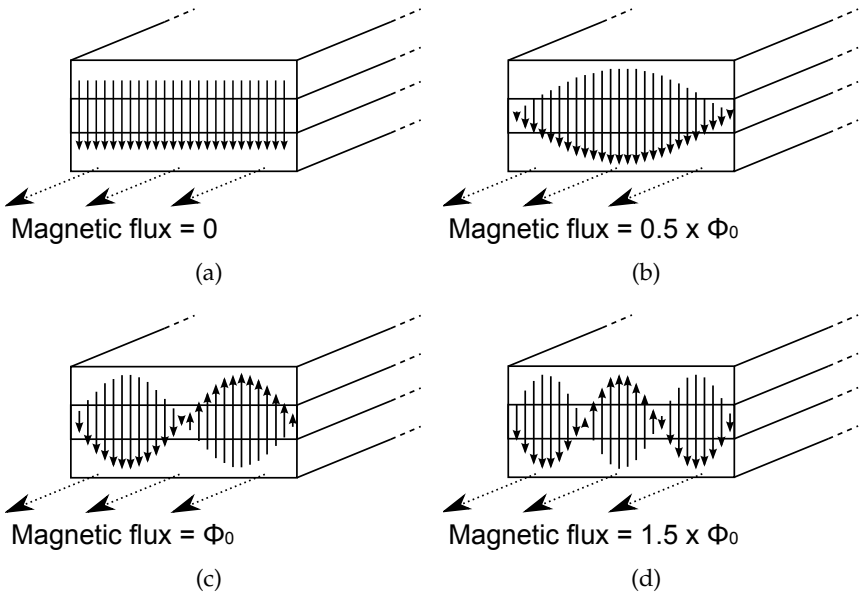

Figure 4.2: The variation of current density in a Josephson junction for different values of flux penetrating the junction. The solid arrows indicate the current density and direction.

4.1.3 RCSJ Model

It is convenient to establish a simple model for Josephson junctions in order to easily describe a given junction's I–V characteristics. Consider a junction subjected to a constant current. While the current flowing through the junction remains below I_c, it will flow as a supercurrent and no voltage will be generated across the junction. However, at finite voltages, quasiparticles will flow through the junction. All junctions also have a finite capacity that must be considered.

Keeping these aspects in mind, the total current I_{tot} through a junction can be written as

$$I_{tot} = I_J + I_d + I_q \tag{4.1.14}$$

where I_J is the Josephson supercurrent, I_q is the quasiparticle current, and I_d is the displacement current of the capacitance. I_J and I_d can easily be defined: $I_J = I_c \sin\phi$ from Equation (4.1.10) and $I_d = C\frac{dv}{dt}$ where C is the junction capacitance and v is the voltage across the junction [18]. I_q is dependent on the conductance of the junction. The conductance itself is a function of the junction voltage and can be defined as

$$G(v) = \begin{cases} \frac{1}{R_{sg}(T)} & \text{for } |v| < \frac{2\Delta(T)}{e} \\ \frac{1}{R_n} & \text{otherwise} \end{cases} \tag{4.1.15}$$

where $\Delta(T)$ is the energy gap. R_{sg}, known as the subgap resistance, can be attributed to the fact that normal electrons already exist at nonzero temperatures. 2Δ represents the energy required to break a superconductive Cooper pair. $\frac{\Delta}{e}$ is known as the gap voltage, and R_n represents the resistance due to the normal electrons after all the Cooper pairs had been broken apart [15].

One can now model the Josephson junction using three channels, each analogous to one of the three currents comprising I_{tot}. This model, shown in Figure 4.3, is known as the *Resistively and Capacitively Shunted Junction*, or RCSJ model. If the capacitance is negligible, then its channel may be removed to form the RSJ model.

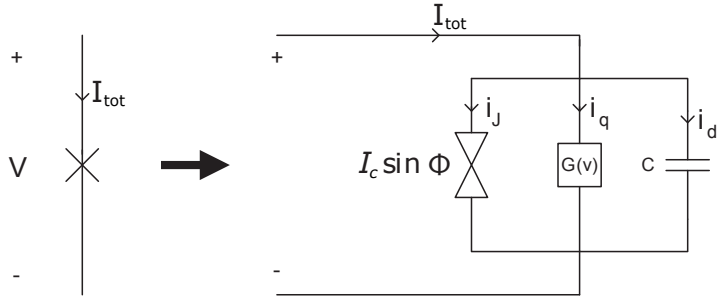

Figure 4.3: The circuit diagram of a Josephson junction as according to the RCSJ model. The three channels are each represented by an appropriate circuit element.

4.1.4 DC Effects

The RCSJ model is particularly useful for characterising the I–V characteristics of a Josephson junction. Consider a junction driven by a current source. According to Kirchhoff's current law, the differential equation for the circuit will be

$$I_{tot} = I_c \sin\phi + GV + C\frac{dV}{dt}, \tag{4.1.16}$$

into which Equation (4.1.11) can be substituted to give

$$I_{tot} = I_c \sin\phi + \frac{\hbar G}{2e}\frac{d\phi}{dt} + \frac{\hbar C}{2e}\frac{d^2\phi}{dt^2} \tag{4.1.17}$$

Dividing by I_c yields

$$\frac{I_{tot}}{I_c} = \beta_c \frac{d^2\phi}{d\theta^2} + \frac{d\phi}{d\theta} + \sin\phi \tag{4.1.18}$$

where $\theta \equiv \omega_c t \equiv \frac{2e}{\hbar}\frac{I_c}{G}t$ and

$$\beta_c \equiv \frac{\omega_c C}{G} = \frac{2e}{\hbar}\frac{I_c}{G}\frac{C}{G}. \tag{4.1.19}$$

For $C = 0$, and thus $\beta_c = 0$, the average voltage can be written as

$$V = \begin{cases} 0 & \text{for } i < I_c \\ \frac{I_c}{G}\sqrt{\left(\frac{i}{I_c}\right)^2 - 1} & \text{for } i > I_c \end{cases} \tag{4.1.20}$$

and is shown in Figure 4.4.

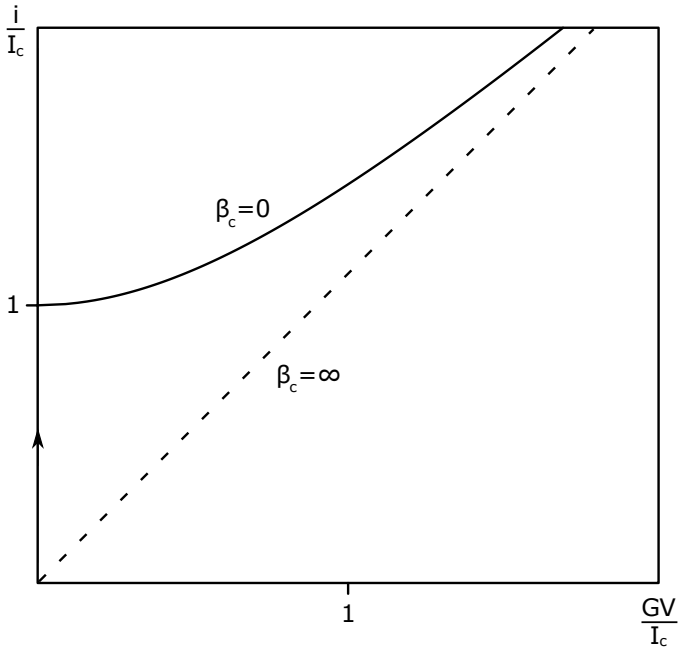

Figure 4.4: I–V behaviour of a fully overdamped (solid line) and highly underdamped (broken line) Josephson junction.

While driving a Josephson junction with $i > I_c$ will result in a voltage across the junction as described by the above mentioned differential equations, the voltage will create an AC current component in accordance with Equation (4.1.12), which will lead to an alternating voltage. These effects compound to create a complex temporal variation of junction voltage.

For a negligible capacitance, the I–V behaviour is non-hysteretic. Larger capacitances and, by extension, larger values of β_c, result in a range between I_c and a lower limit I_{min} in which there are two values of junction voltage, $V = 0$ and $V \neq 0$, depending on whether the current was increased or decreased into the range. An example of a case where $\beta_c \approx 50$ is shown in Figure 4.5 [17]. A Josephson junction is *underdamped* when $\beta_c > 1$ and *overdamped* when $\beta_c < 1$. Junction capacitance depends heavily on the junction type [18].

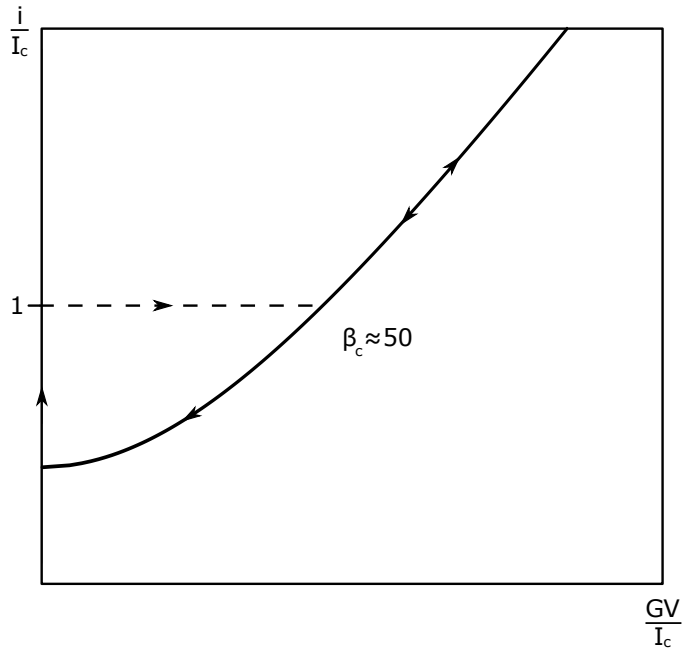

Figure 4.5: I–V behaviour of a Josephson junction with $\beta_c \approx 50$.

4.1.5 AC Effects

Driving a Josephson junction with both DC and AC sources is typical in scenarios where such junctions are used as detectors. The I–V behaviour of such configurations can be easily explained using two limiting cases.

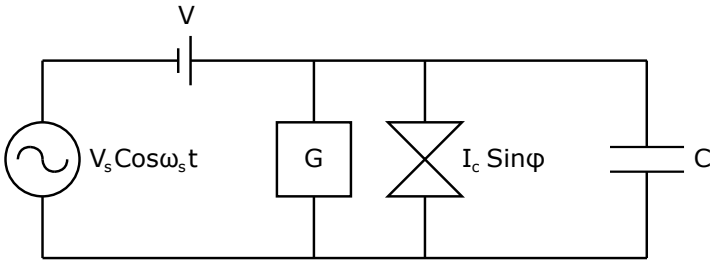

Figure 4.6: Ideal voltage source with zero internal impedance.

In the first case, a Josephson junction is driven by an ideal voltage source with zero internal impedance as shown in Figure 4.6. Using the Josephson relations, i_J can be written as

$$i_J(t) = I_c \sin\left[\int_0^t \frac{2eV(t')}{\hbar} dt' + \phi_0\right]. \tag{4.1.21}$$

$V(t)$ in this case is $V + V_s \cos \omega_s t$, therefore, the above becomes

$$i_J(t) = I_c \sin \left[\frac{2eV}{\hbar} t + \frac{2eV_s}{\hbar\omega_s} \sin \omega_s t + \phi_0 \right] \tag{4.1.22}$$

[17]. Using the Fourier-Bessel series identity

$$e^{jx \sin \theta} = \sum_{n=-\infty}^{\infty} J_n(x) e^{jn\theta} \tag{4.1.23}$$

where J_n is the n-th order Bessel function of the first kind [15], along with standard trigonometric identities, i_J can be written as

$$i_J(t) = I_c \sum_{n=-\infty}^{\infty} (-1)^n J_n \left(\frac{2eV_s}{\hbar\omega_s} \right) \sin \left[(\omega_J - n\omega_s)t + \phi_0 \right] \tag{4.1.24}$$

where $\omega_J = \frac{2eV}{\hbar}$ is the Josephson oscillation frequency. From Equation (4.1.24) it can be observed that values of average voltage V when $\omega_J = n\omega_s$, or

$$V = \frac{n\hbar\omega_s}{2e} \tag{4.1.25}$$

will yield current spikes of maximum amplitude $I_c J_n \left(\frac{2eV_s}{\hbar\omega_s} \right)$, where $\phi_0 = \pi/2$. Each value of DC voltage yields a DC current through the conductance channel, $I_G = GV$. The sum of these currents are shown in Figure 4.7.

In reality, the measurements will not be spikes, but steps, as junction resistances are usually low enough that voltage sources act like current sources, which is discussed next.

The second case involves a Josephson junction driven by a constant current source with infinite internal impedance and is shown in Figure 4.8. Such configurations must be solved numerically, however, the results are much closer to actual experimental data. Typical I–V behaviour for this case is shown in Figure 4.9. The clearly visible steps are known as *Shapiro steps*. The heights of these steps are a very sensitive and definitve test for the Josephson effect [17].

4.2 Types of Josephson Junctions

Josephson junctions can be classified into two distinct overarching types: *extrinsic* and *intrinsic* interfaces. Extrinsic interfaces typically consist of two superconducting electrodes seperated by an artificial barrier, such as a normal metal (N), insulator (I) or semiconductor (Se). Intrinsic interfaces are junctions that naturally occur under certain circumstances.

Extrinsic interfaces are rarely used for high-T_c superconductors. Extrinsic HTS junctions require a fully epitaxial layer structure, unlike LTS junctions. High-T_c

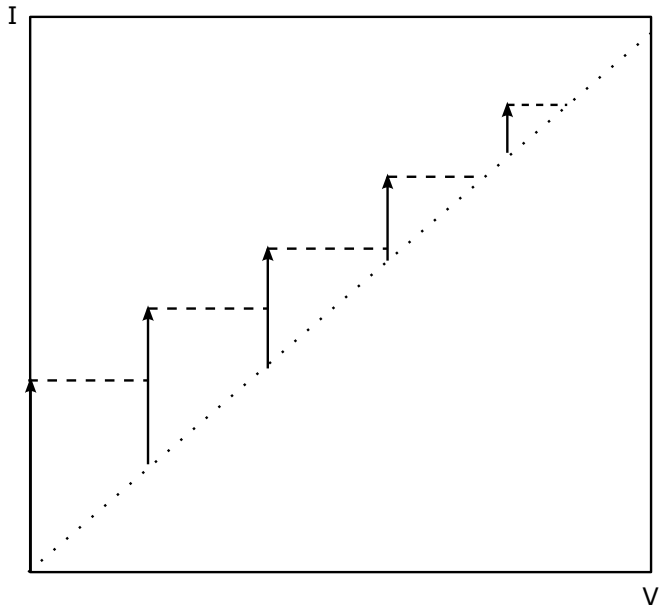

Figure 4.7: I–V behaviour according to the AC voltage source model.

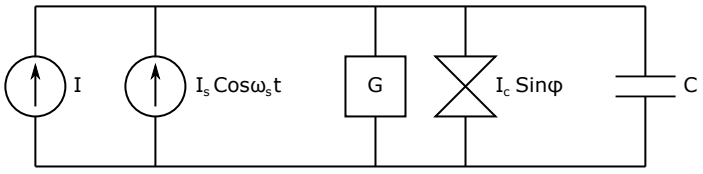

Figure 4.8: Ideal current source with infinite internal impedance.

superconductors are also very sensitive to structural and chemical changes and imperfections. Atomically near-perfect HTS films are required for feasible extrinsic Josephson junctions.

Intrinsic interfaces are therefore preferable for HTS films, however, optimisation and manufacturing control of intrinsic junctions remain difficult enough that worldwide reproducibility is still very low.

The following are examples of some of the Josephson junction types or *topologies*:

- *Junctions without interfaces*: These are junctions created via constrictions such as nanobridges, which is shown in Figure 4.10(a) and weakend structure junctions. They require only a single HTS film layer and therefore are easy to fa-

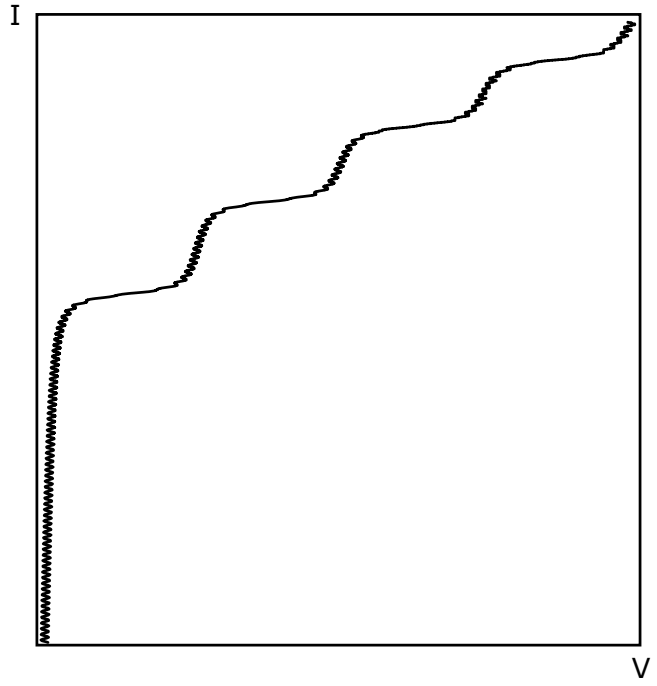

Figure 4.9: A simulation of the I–V behaviour of a Josephson junction according to the AC current source model. The Shapiro steps are clearly visible.

bricate. The Josephson effect is achieved via intrinsic properties despite the fact that technically no single point of interface exists.

- *Junctions with intrinsic interfaces/barriers*: These are junctions formed by grain boundaries such as bicrystals, step-edges, bi-epitaxial layers as well as the specifically named *intrinsic Josephson junctions* (IJ) [19]. Grain boundaries are classified according to the rotation and displacement of the adjoining crystals. Rotational grain boundaries can have the grain rotated around an axis perpendicular or in the plane of the grain boundary. These are known as the *twist* and *tilt* of the misorientation [20].

  – *Bicrystal junctions* (BCJ): Bicrystal substrates consist of two crystals at different orientations fused together, such as the example shown in Figure 4.10(c). Any HTS film deposited on the substrate will have the same orientations and, therefore, the same grain boundary due to epitaxial growth. J_c is dependent on the misorientation angle θ. This allows a certain measure of control over the desired value of J_c upon fabrication. The creation of BCJs is a simple process. One needs simply deposit and etch the HTS film for the junction to be completed. Unfortunately, bi-

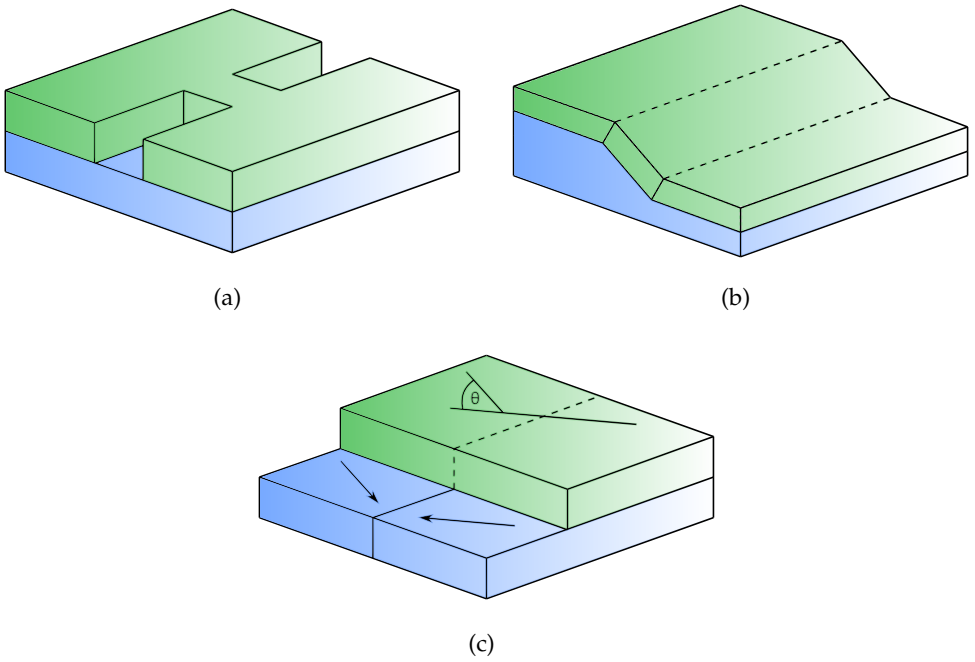

Figure 4.10: A few examples of Josephson junction topologies: (a) nanobridge, (b) step-edge and (c) bicrystal junction. The broken lines in (b) and (c) indicate the grain boundaries where the junctions will form. The arrows in (c) indicate the different grain angles that result in a grain boundary. In each case, blue represents the crystal substrate, and green represents the superconducting thin film.

crystal substrates are comparatively expensive to manufacture and the junctions are limited to the location of the boundary line [19]. The same principle used in the construction of bicrystals can be extended to create tricrystalline, tetracrystalline and polycrystalline substrates and films [20].

– *Step-edge junctions* (SEJ): These junctions are created by milling a step into the substrate, then depositing the HTS film. The junction will be formed at either the upper or lower edge of the step, or both, as shown in Figure 4.10(b). The step angle and height are both important parameters to consider. If either is too low, then the junction will not be formed [19]. SEJs allow greater freedom of junction placement than BCJs, however, they are more complicated to manufacture, as the step itself also needs to be fabricated, either by milling directly into the base substrate, or by depositing and milling a buffer layer. The latter is discussed in Chapter 7.6.

– *Bi-epitaxial junctions* (BEJ): Due to the epitaxial relationships between certain materials, certain films can be grown with a natural grain rotation

between it and the layer/substrate on which it was grown. Thus, carefully prepared template layers can result in controlled rotational grain boundaries at the edges of the template structures. This rotation is typically fixed at 45°. As with SEJs, BEJs provide one with the advantage of freely selecting the junctions' positions. Unfortunately, the misorientation angle cannot be changed. Deviations from 45° have been reported, but these are not reproducible [20].

  - *Intrinsic Josephson junctons* (IJ): Highly anisotropic, layered HTS materials, such as BSCCO, exhibit near ideal underdamped SIS behaviour in the c-axis direction. IJs can be modelled as a stack of coupled SIS junctions.

- *Junctions with extrinsic interfaces*: Extrinsic junctions are most succesfully utilised in LTS applications due to the difficulty in their fabrication for HTS films. Examples of such junctions are ramp-edges, planar sandwiches and step-edge type proximity effect junctions [19].

Chapter 5

SQUIDs

A superconducting loop containing at least one Josephson junction is known as a *Superconducting Quantum Interference Device* (SQUID) or an *interferometer*, so named for the interference of the wavefunctions across the junctions. Single and double junction SQUIDs are also referred to as RF and DC SQUIDs respectively, due to the methods used to bias the devices. The DC SQUID is discussed in more detail below.

5.1 Theory of SQUIDs

An illustration of a SQUID loop is shown in Figure 5.1. The electron pair wave functions of the upper and lower superconducting electrodes weakly interfere through the Josephson junctions. Passing a magnetic flux through the loop changes the phase differences of the respective junctions and, consequently, the critical current of the SQUID as well. Finding an expression for the total current I_t in the SQUID is done by integrating the gradient of phase clockwise around the loop as shown by the broken line. Excluding the junction gaps yields

$$\int_A^B \nabla\theta d\boldsymbol{\ell} + \int_C^D \nabla\theta d\boldsymbol{\ell} = -\frac{2e}{\hbar}\int_A^B \boldsymbol{A} d\boldsymbol{\ell} - \frac{2e}{\hbar}\int_C^D \boldsymbol{A} d\boldsymbol{\ell}. \tag{5.1.1}$$

This can also be written as

$$\oint \nabla\theta d\boldsymbol{\ell} - (\theta_A - \theta_D) - (\theta_C - \theta_B) = -\frac{2e}{\hbar}\oint \boldsymbol{A} d\boldsymbol{\ell} + \frac{2e}{\hbar}\int_D^A \boldsymbol{A} d\boldsymbol{\ell} + \frac{2e}{\hbar}\int_B^C \boldsymbol{A} d\boldsymbol{\ell} \tag{5.1.2}$$

which can be further simplified by writing the guage-invariant phases across the junctions as

$$\phi_1 = \theta_A - \theta_D + \frac{2e}{\hbar}\int_D^A \boldsymbol{A} d\boldsymbol{\ell} \tag{5.1.3}$$

$$\phi_2 = \theta_C - \theta_B + \frac{2e}{\hbar}\int_B^C \boldsymbol{A} d\boldsymbol{\ell}. \tag{5.1.4}$$

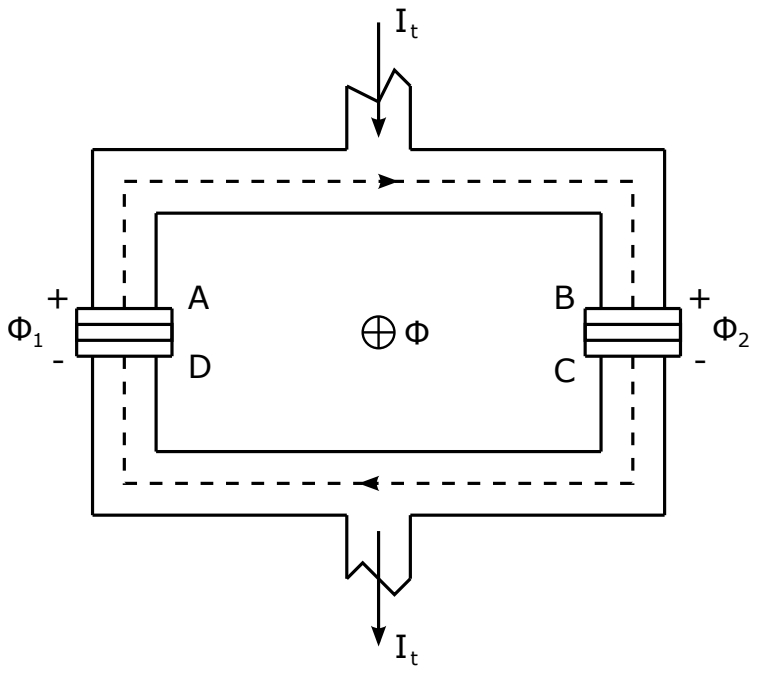

Figure 5.1: The DC SQUID loop. The SQUID is biased with a DC current I_t, and threaded by a magnetic flux Φ.

Considering that the line integral of $\nabla\theta$ is a multiple of 2π, taken for convenience as $-2n\pi$, and the line integral of the vector potential is the flux in the loop, Equation (5.1.2) can now be written as

$$\phi_2 = \phi_1 + 2n\pi - 2\pi\frac{\Phi}{\Phi_0} \tag{5.1.5}$$

where Φ lies between $-\Phi/2$ and $\Phi/2$. The total current through the SQUID can now be written as

$$\begin{aligned} I_t &= I_1 + I_2 \\ &= I_{c1}\sin\phi_1 + I_{c2}\sin\phi_2 \\ &= I_{c1}\sin\phi_1 + I_{c2}\sin\left(\phi_1 - \frac{2\pi\Phi}{\Phi_0}\right) \end{aligned} \tag{5.1.6}$$

where the $2n\pi$ has been omitted, allowing Φ to range over all values [17].

In order to find the maximum current through the SQUID, define γ as

$$\gamma = \phi_1 - \frac{\pi\Phi}{\Phi_0}. \tag{5.1.7}$$

The total current can now be written as

$$\begin{aligned} I_t &= I_{c1}\sin\left(\gamma+\frac{\pi\Phi}{\Phi_0}\right)+I_{c2}\sin\left(\gamma-\frac{\pi\Phi}{\Phi_0}\right) \\ &= I_{c1}\sin\gamma\cos\frac{\pi\Phi}{\Phi_0}+I_{c1}\cos\gamma\sin\frac{\pi\Phi}{\Phi_0}+I_{c2}\sin\gamma\cos\frac{\pi\Phi}{\Phi_0}-I_{c2}\cos\gamma\sin\frac{\pi\Phi}{\Phi_0} \\ &= 2I_{c1}\sin\gamma\cos\frac{\pi\Phi}{\Phi_0} \end{aligned} \tag{5.1.8}$$

for the simplified case where $I_{c1} = I_{c2}$. The maximum current is found when $\sin\gamma = \pm 1$, depending on the sign of I_t, and can be written in absolute terms as

$$I_{Tc} = 2I_c\left|\cos\frac{\pi\Phi}{\Phi_0}\right| \tag{5.1.9}$$

and is shown in Figure 5.2 [21]. The corresponding I–V characteristics of a SQUID

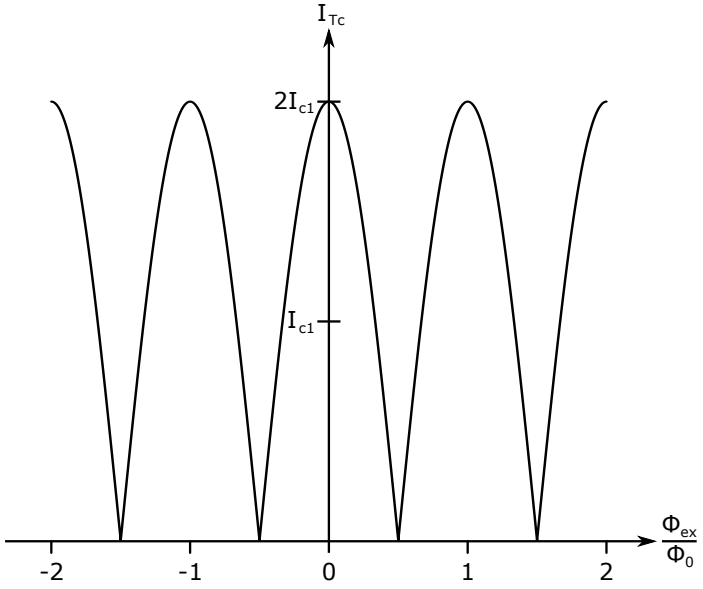

Figure 5.2: The modulation of maximum critical current of a SQUID as a function of externally applied flux.

with symmetric, non-hysteretic junctions are shown in Figure 5.3 for the two extreme cases presented by Equation (5.1.9) where the SQUID loop contains integer and half-integral numbers of flux quanta.

Up to this point the self induced magnetic field caused by currents circulating in the superconducting loop has been neglected. In order to calculate the effect of this magnetic field, assume that the SQUID is physically symmetrical and that $I_{c1} = I_{c2}$. A current of $I_t/2$ will flow through both junctions, leading to the flux in the loop

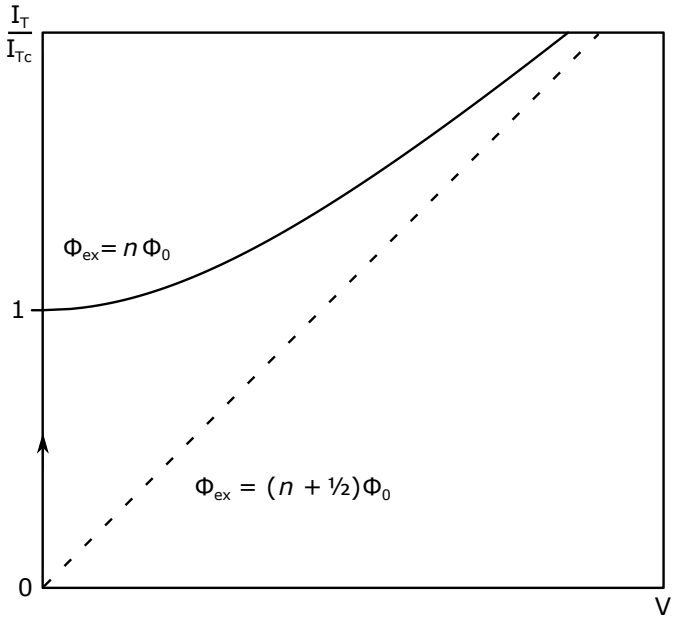

Figure 5.3: The I–V characteristics of a SQUID threaded by integer and half-integral numbers of flux quanta.

being cancelled out. An externally applied flux will result in $I_1 \neq I_2$, leading to a circulating current $I_{circ} = (I_2 - I_1)/2$. From the definition of inductance, the self induced flux is

$$\begin{aligned} \Phi_s &= LI_{circ} \\ &= \frac{1}{2}L(I_2 - I_1) \\ &= \frac{1}{2}LI_{c1}(\sin\phi_2 - \sin\phi_1). \end{aligned} \tag{5.1.10}$$

The total flux in the loop will be

$$\begin{aligned} \Phi_{tot} &= \Phi_{ex} + \Phi_s \\ &= \Phi_{ex} + \frac{1}{2}LI_{c1}(\sin\phi_2 - \sin\phi_1). \end{aligned} \tag{5.1.11}$$

Substituting this into Equation (5.1.5) yields

$$\phi_2 = \phi_1 - \frac{2\pi}{\Phi_0}\left[\Phi_{ex} + \frac{LI_{circ}}{2}(\sin\phi_2 - \sin\phi_1)\right] \tag{5.1.12}$$

where, once again, the $2n\pi$ term has been ommitted to allow Φ to range over all values. Equation (5.1.12) can now be solved for ϕ_2 in terms of ϕ_1 and Φ_{ex}, allowing the calculation of Φ_{tot} and, by extension, I_t. However, solving it must be done numerically.

The depth of modulation shown in Figure 5.2 represents the ideal case where the loop inductance L is practically zero. The minimum value of the modulation is heavily dependent on the inductance. An approximation of this dependence is shown in Figure 5.4. Logically, if the critical current of a SQUID is modulated

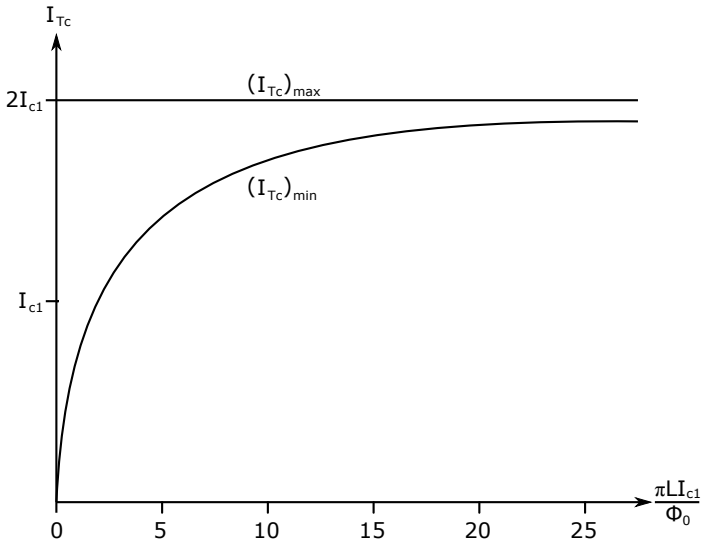

Figure 5.4: Dependence of the maximum and minimum values of the critical current of a SQUID as a function of the SQUID loop inductance. These values determine the modulation depth achievable from an external magnetic field.

by external magnetic fields, then so will the I–V characteristics of the SQUID be modulated. This is the key to flux detection via SQUIDs. The concept is illustrated in Figure 5.5. The modulation of I_{Tc} leads to a variation of the SQUID voltage in the form of $\Delta V \approx R_D \Delta I_{Tc}$, where $R_D = \frac{dV}{dI}$ is the *dynamic resistance* of the SQUID. The voltage variation is periodic with respect to the applied flux with period Φ_0 [17].

Flux detection in SQUIDs presents an interesting problem. Typically, one would desire the SQUID loop to be as large as practically possible, in order to maximise the flux sensitivity. Unfortunately, a large SQUID loop leads to a large loop inductance L which, in turn, leads to increased flux noise. Numerical analysis has indicated that in order to keep the flux noise levels acceptable, the loop inductance must be

$$L < \frac{\Phi_0}{5k_B T} \tag{5.1.13}$$

where k_B is Boltzmann's constant [17]. For SQUIDs cooled in liquid nitrogen, this requires that $L < 804$ pH at 77 K.

In order to compensate for the required small SQUID loop, a pickup loop is utilised to capture external flux and pass it to the SQUID, either by using the pickup

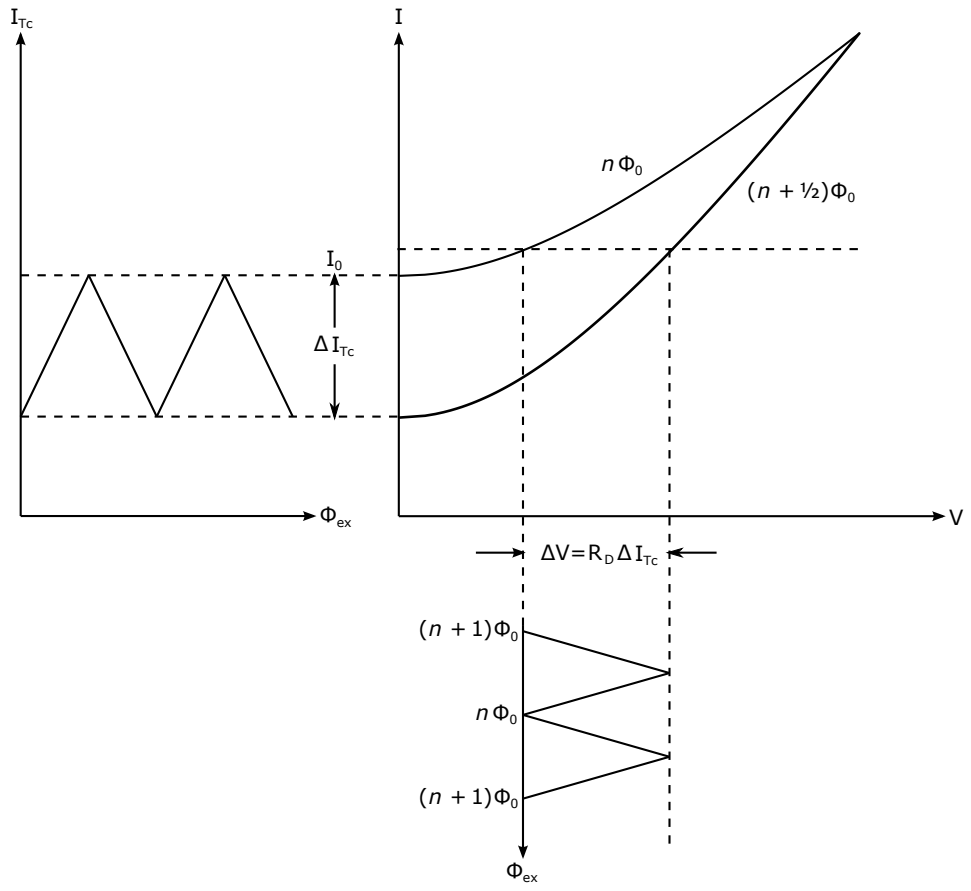

Figure 5.5: Variation of SQUID voltage due to the modulation of the critical current from externally applied flux.

loop as a flux transformer or by directly connecting the pickup loop to the SQUID loop. The direct connection method, known as *direct coupling* or *direct injection*, is reliable and simple to fabricate, as it can be achieved using only a single thin film layer. Flux transformers are more complicated to manufacture and requires precise manual alignment, however, it provides the advantage of allowing multiple turns at the SQUID end of the transformer, resulting in increased flux density coupling [17].

5.2 Gradiometers

5.2.1 Fundamentals

Practical limitations of many applications often prevent one from operating the SQUID itself in a shielded environment. A common solution in these cases is to use the SQUID as a gradiometric sensor, or *gradiometer*. This is achieved by arranging primarily the pickup loop, but preferably also the SQUID loop, in such a way that

will allow it to detect the gradient of a given magnetic field, rather than the field itself. This configuration has the advantage of automatically cancelling out uniform fields such as the earth's magnetic field or fields originating from relatively far away sources.

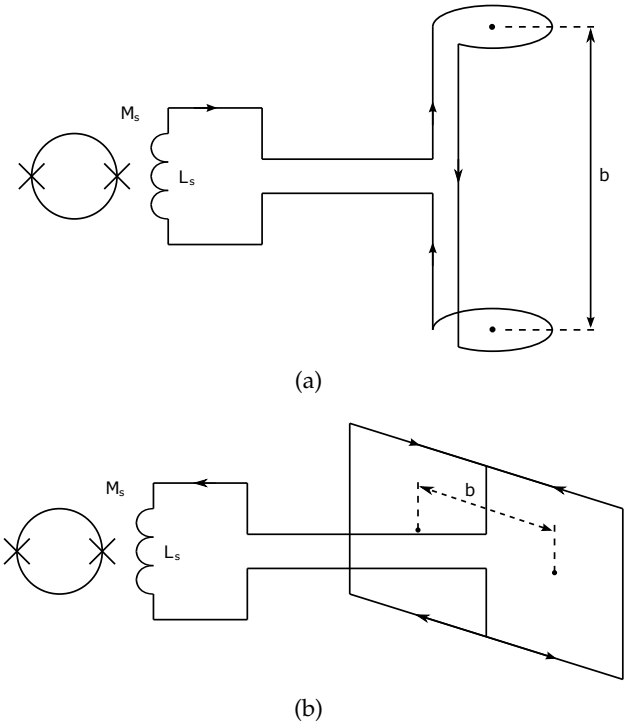

Figure 5.6: Two common pickup loop configurations for SQUID gradiometers, namely (a) axial and (b) planar.

Two basic pickup loop configurations are shown in Figure 5.6. Both layouts are examples of first order gradiometers. First order gradiometers are created by arranging the pickup loop either as two parallel loops or two series loops oppositely wound. The first type is known as an axial gradiometer, shown in Figure 5.6(a), and the second type as a planar gradiometer, shown in Figure 5.6(b). These configurations will couple zero net flux of uniform fields, while non-zero net flux of the gradients of non-uniform fields will be coupled instead. Axial gradiometers will measure the gradient $\frac{\partial B}{\partial z}$, while planar gradiometers will measure off-diagonal gradients, such as $\frac{\partial B}{\partial x}$.

Higher order gradiometers can also be created for the purposes of measuring second or higher order gradients of magnetic fields. A gradiometer of order n would be constructed by using a first order configuration, but where the two opposing loops are already gradiometric of order $n-1$.

Two important figures of merit are the distance of seperation between the pickup coils, known as the baseline b, and the ratio between the response to a uniform field and the response to the gradient of a field, known as the balance. Generally, one should strive to maximise the baseline, and minimise the balance [21].

5.2.2 Design

Single-layer thin film gradiometers (SLG) are limited to planar configurations and, therefore, can only measure off-diagonal gradient components. However, due to the relative simplicity of the fabrication process, SLGs remain an attractive choice for many practical applications.

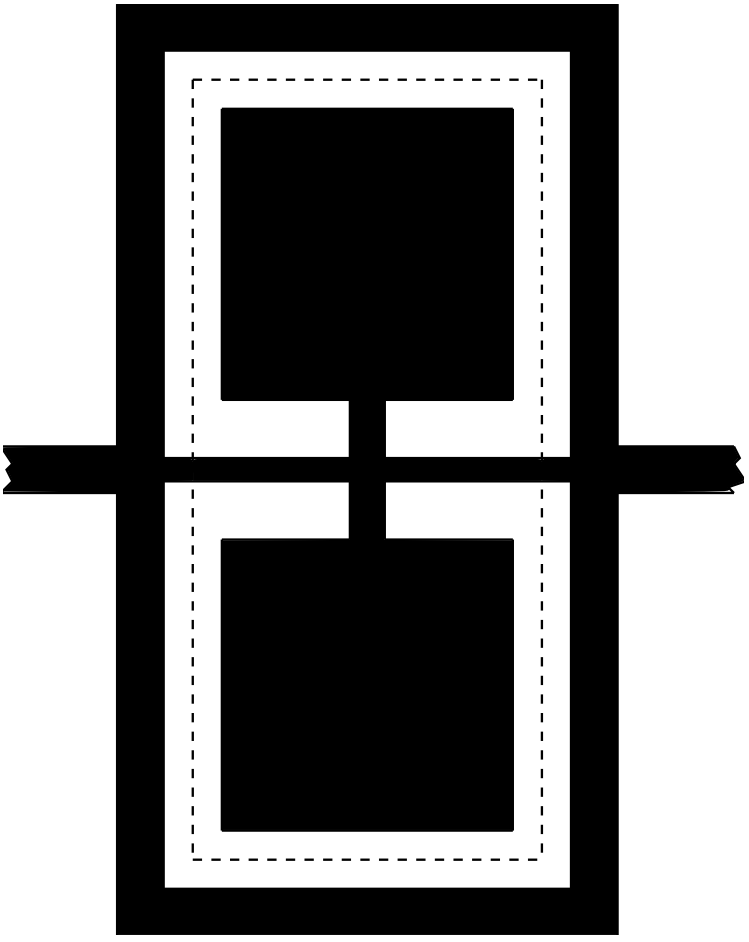

Figure 5.7: The layout schematic of the G-SQUID. The broken line indicate the grain boundary where the Josephson junctions will form. The inner pads are connected to ground and the tracks going out to the sides connect the SQUID to the pickup loops.

Conventional SQUID SLGs suffer from an inherent problem: the SQUID loop remains responsive to uniform magnetic fields. The voltage across the SQUID can be

approximated as

$$V \propto b\frac{\partial B_z}{\partial x}A_{grad} + B_z A_{par} \tag{5.2.1}$$

where b is the baseline, and A_{grad} and A_{par} are the effective area of the device which is sensitive to first order field gradients and the parasitic effective area respectively. The parasitic effective area can be considered as having two components

$$A_{par} \approx A_{SQ} + A_{def} \tag{5.2.2}$$

where A_{SQ} and A_{def} are the uniform field effective areas of the SQUID and any defects in the device respectively. A_{par} must be minimised for effective usage in unshielded environments. The G-SQUID was designed for this purpose [22].

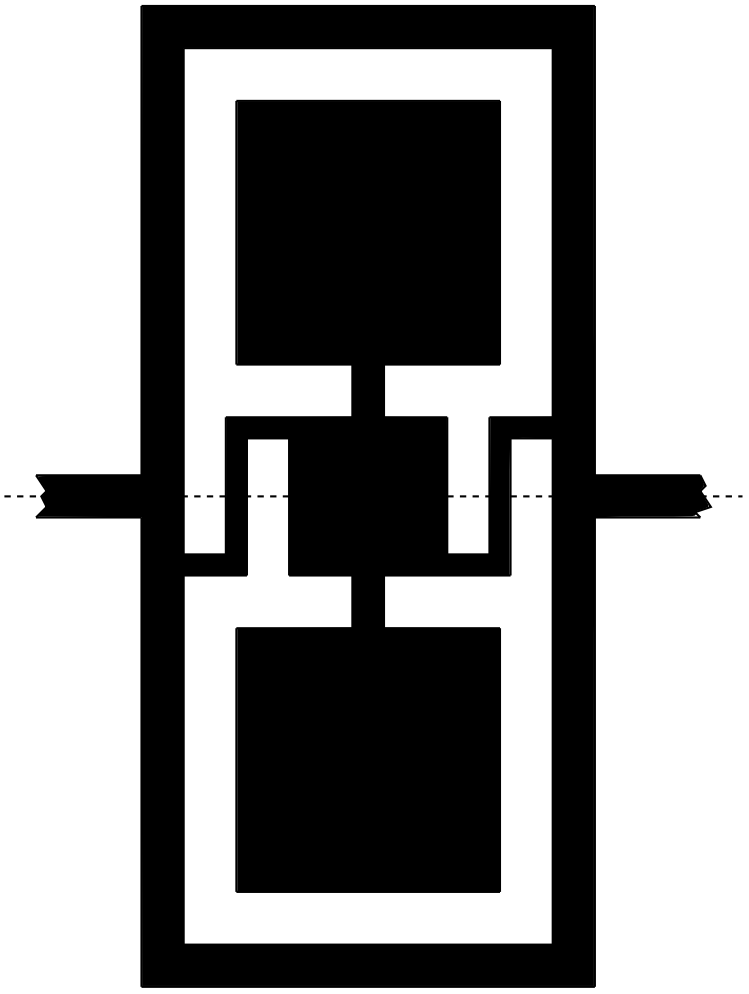

Figure 5.8: An alternative layout schematic of the G-SQUID. The design is intended for use with a single grain boundary, indicated by the broken line, forming both junctions.

The YBCO layout of the G-SQUID is shown in Figure 5.7. The SQUID loop is configured in the same fashion as the pickup loops, resulting in the SQUID loop itself

being sensitive to only field gradients and not uniform fields. The broken line indicates an intended grain boundary to form the Josephson junctions. The design was made with step-edge grain boundaries in mind, however it is also suitable for use with nanobridge junctions. The inner pads are to be connected to ground and the tracks extending to the left and right connect the SQUID to the pickup loops.

A variant of this design was also considered and is shown in Figure 5.8 [23]. The broken line indicates the grain boundary. Originally meant for use with bicrystal substrates, this design is also theoretically feasible using a step-edge grain boundary as well. The practicality of both designs are discussed in Chapter 8.3.

The dimensions of the two designs are shown in Appendix A. The dimensions were chosen based on the fabrication limitations of the laboratories at the Electrical and Electronic department of the Stellenbosch University Engineering Faculty. The dimensions were minimised with these limitations in mind, in order to keep the SQUID loop inductance as low as possible. One such limitation is that the inner contact pads of the SQUID, which must be connected to ground, have to be connected to contact pads outside the SQUID loop. This connection can only be achieved via wirebonding at the time of writing, limiting the inner contact pads to a minimum of 50×50 μm. The width of the YBCO tracks were chosen to be of the same order as existing designs in the faculty laboratory. The inductance of the SQUID loop for the given dimensions were calculated using FastHenry 3.0wr, where the London penetration depth of YBCO was set to 140 nm [24]. The original G-SQUID design was calculated to have a loop inductance of 123 pH, and the variant design had 153.61 pH, well within the limits proposed by Equation (5.1.13). The FastHenry code used in the calculations is given in Appendix C.

Chapter 6

Electronics

A SQUID is suitable as an active device in many applications. This chapter discusses the supporting electronics required for utilising the SQUID as a magnetic field sensor. These electronics include the current source required for biasing the SQUID, the flux-locked loop which is used to linearise the SQUID output, and the application specific output bandpass filter which will isolate the desired signal for detection.

6.1 Flux-locked Loop

6.1.1 Fundamentals

In order to obtain usable linear output directly from a SQUID, it is necessary to operate the SQUID in a small-signal mode around a fixed point W, as shown in Figure 6.1. W is typically chosen to be located on the steepest part of the V–Φ

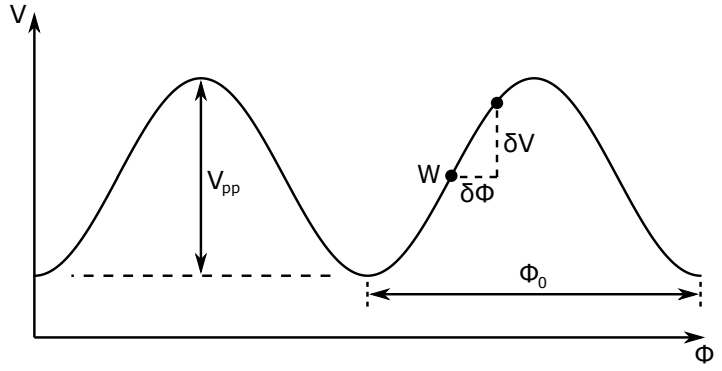

Figure 6.1: The V–Φ characteristic of a SQUID.

characteristic. This configuration will allow a change in applied flux to produce a

corresponding change in the SQUID voltage as

$$\delta V = V_\Phi \delta\Phi \tag{6.1.1}$$

where $V_\Phi \equiv \frac{\partial V}{\partial \Phi}$ is the transfer coefficient for the given working point. However, as can be seen from Figure 6.1, the further $\delta\Phi$ extends from W, the more distorted the output will become. A useful approximation for the acceptable linear flux range of a sinusoidal V–Φ characteristic is

$$\Phi_{lin} = \frac{V_{pp}}{|V_\Phi|} \lesssim \frac{\Phi_0}{\pi} \tag{6.1.2}$$

where V_{pp} is the peak-to-peak voltage of the SQUID. The applied flux Φ is now limited to $\Phi_{lin}/2$, which is only practical for a small number of applications. Stronger signals may require a larger linear range and environmental interferences can easily be orders of magnitude larger, even in shielded environments. Thus, practical SQUID operation requires a method to effectively linearise the SQUID transfer function.

Designing readout electronics does not require knowledge or understanding of SQUID fundamentals. The SQUID can be viewed as a flux-to-voltage converter with a non-linear transfer function. Though a number of linearisation schemes exist, the typical method is to operate the SQUID in a *flux-locked loop* (FLL). There are two basic approaches to building a flux-locked loop: direct readout and flux modulation readout. The direct readout scheme is shown in Figure 6.2. Similar

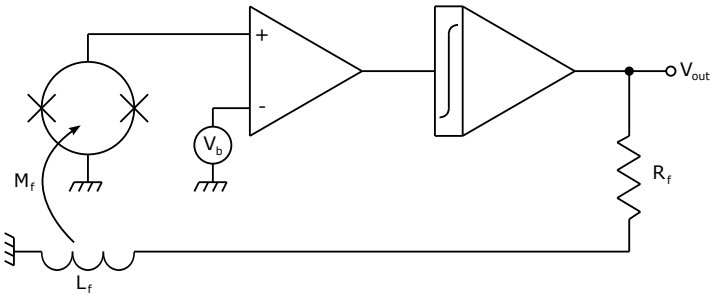

Figure 6.2: The direct readout flux-locked loop. The SQUID and the feedback coil are both cooled at cryogenic temperatures.

to the small signal method previously discussed, the SQUID is biased at a fixed working point W at the steepest part of the V–Φ characteristic. The SQUID output is amplified, integrated, and inductively fed back into the SQUID. The feedback resistance R_f is usually in the kΩ range in order to render the impedance of the feedback coil negligible for a given frequency range. Assuming infinite integrator gain, the flux provided by the feedback coil will counterbalance the applied flux,

resulting in the voltage across the feedback resistor to vary linearly with the applied flux. The primary drawback to direct readout is the low dynamic resistance of the SQUID resulting in low voltage noise [25]. The flux modulation readout scheme is

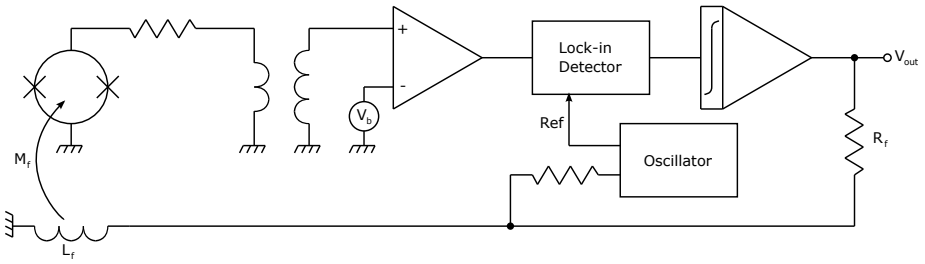

Figure 6.3: The flux modulation readout flux-locked loop. The SQUID, feedback coil and step-up transformer are cooled at cryogenic temperatures.

shown in Figure 6.3. In contrast to direct and small signal readout, the SQUID is periodically switched between two working points W+ and W- at adjacent slopes of the V–Φ sinusoid by applying a square-wave flux signal to the SQUID. This signal is usually between 100 kHz and 500 kHz. The resulting SQUID voltage for this scheme is shown in Figure 6.4. Assuming zero ac voltage across the SQUID for zero applied flux, a positive change in applied flux will result in a square-wave SQUID voltage that is out of phase with the modulation flux. A negative change in flux will yield an in phase square wave voltage. This property of the resultant SQUID voltage, along with the amplitude thereof, can be used to detect the applied flux. The configuration of a flux modulation scheme is as follows: The SQUID

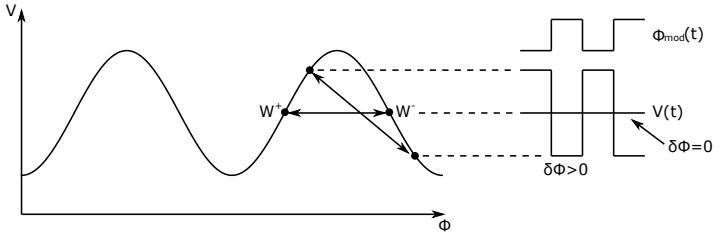

Figure 6.4: The V–Φ characteristic of a SQUID with a flux modulation FLL. The output voltage of the SQUID is shown on the right. The SQUID is switched between working points W^+ and W^-, resulting in an applied flux being reflected as a square wave voltage either in phase or out of phase with the modulation signal, depending on whether the applied flux was positive or negative.

voltage is amplified first via a step-up transformer, which is cooled along with the SQUID, then via a preamplifier at room temperature. The amplified signal is then

fed into a lock-in detector, the output of which will display an image of the V–Φ characteristic. From this point the scheme is similar to direct readout: The signal from the lock-in detector output is integrated, then fed back to the SQUID via a feedback resistor and coil in order to counterbalance the applied flux. The voltage across the feedback resistor is once again linearly dependent on the applied flux. It is important to note that a small resistance must be placed between the SQUID and the step-up transformer in order to prevent the SQUID from being shorted. The turn ratio of the transformer must be chosen to match the dynamic resistance of the SQUID to the optimum source resistance of the preamplifier.

Flux modulation allows for an efficient method of achieving high quality V–Φ characteristics, however, the frequency of the modulation flux signal limits the achievable system bandwidth. Noise levels may also increase if the SQUID exhibits strong resonance distorted V–Φ characteristics. Direct readout does not have this problem, allowing for a higher system bandwidth. This makes direct readout a good choice for wideband or multichannel applications [25].

6.1.2 Additional Improvement Schemes

The output of a flux-locked loop can be improved via certain optional additions to the circuitry. The two additions discussed here are *additional positive feedback* (APF) and *bias reversal*. Additional positive feedback is a scheme intended for use

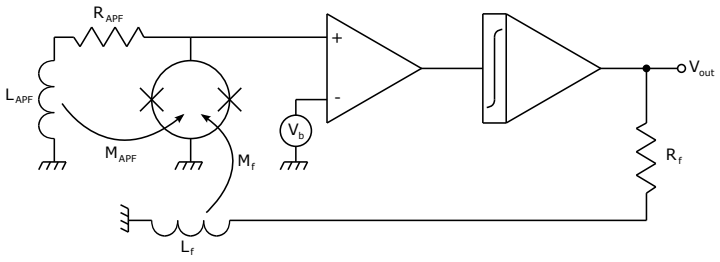

Figure 6.5: The direct readout flux-locked loop with additional positive feedback. The SQUID, feedback coil, APF coil and resistor are all cooled at cryogenic temperatures.

with direct readout electronics and is shown in Figure 6.5. The circuit consists of a resistor and feedback coil connected in series. This circuit is connected in parallel with the SQUID, where the feedback coil is coupled to it. The resistor is typically cooled along with the SQUID in order to minimise noise.

Assuming once more that the SQUID is biased at a working point W on the positive slope of the V–Φ characteristic, a positive change in flux will result in a positive change in voltage. This will form a corresponding current in the APF

circuit, inducing an additional positive flux in the SQUID. This further increases the SQUID voltage and enhances the transfer coefficient V_Φ. If W is on the negative slope, then V_Φ is lowered, resulting in an asymmetric V–Φ characteristic as shown in Figure 6.6. The APF circuit can be represented as a small-signal amplifier, an

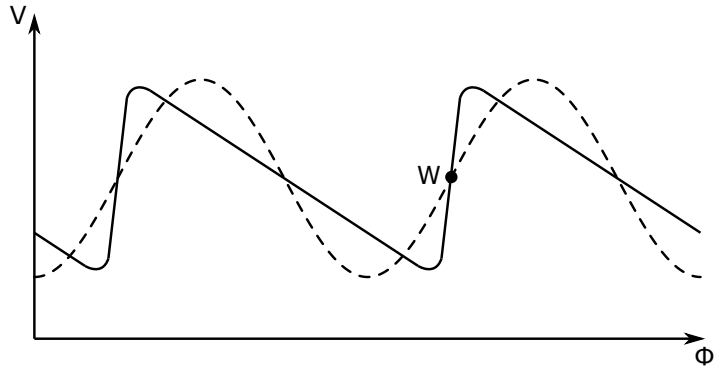

Figure 6.6: The V–Φ characteristic of a SQUID with a FLL with APF. The effect of the APF increases the transfer coefficient on the positive slope of the characteristic, and lowers it on the negative slope.

equivalent circuit of which is shown in Figure 6.7. The amplifier gain can be written as

$$G_{APF} = \frac{1}{1 - \beta_{APF}} \tag{6.1.3}$$

where

$$\beta_{APF} = \frac{V_\Phi M_{APF} - R_{dyn}}{R_{APF}} \lesssim 1. \tag{6.1.4}$$

is the feedback coefficient and V_Φ is the transfer coefficient of the SQUID without APF. The gain G_{APF} represents the increase of the flux-to-voltage coefficient. The output resistance $G_{APF}R_{dyn}$ represents the dynamic resistance of the SQUID with APF. The voltage source $V_{N,APF}$ at the amplifier input is used to represent the noise

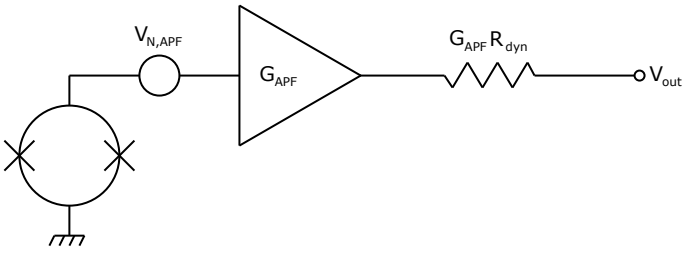

Figure 6.7: The equivalent small-signal amplifier which can be used to represent the APF circuit.

contribution of the APF resistor. The spectral density of the noise source is given as

$$S_{V,APF} = 4k_B T R_{APF} \beta_{APF}^2 \approx 8k_B T R_n \tag{6.1.5}$$

where the right-hand side of the equation has been obtained for realistic parameters $G_{APF} = 10$ and $R_{APF} = 2.5R_n$, where R_n is the normal resistance of the SQUID. It is clear that lowering R_{APF} will lower the noise contribution, however the APF resistor acts as an extra shunt at low frequencies, lowering the peak-to-peak voltage V_{pp}. For this reason, R_{APF} must be chosen such that $R_{APF} \gg R_n/2$. The APF noise contribution is acceptably lower than the SQUID contribution of approximately $16k_B T R_n$. By increasing the transfer coefficient, the APF reduces the effect of the preamplifier voltage noise, which is commonly the dominant noise contribution in a direct readout FLL [25].

The second FLL improvement, bias reversal, can be applied to both direct and flux modulation readouts. Bias reversal was developed to lessen the effects of low-frequency fluctuations in both I_c and R_n. These fluctuations are typically too weak to be a noticeable contribution in the low-frequency noise of LTS SQUIDs, however, they are a dominant source of such noise in HTS SQUIDs. These fluctuations,

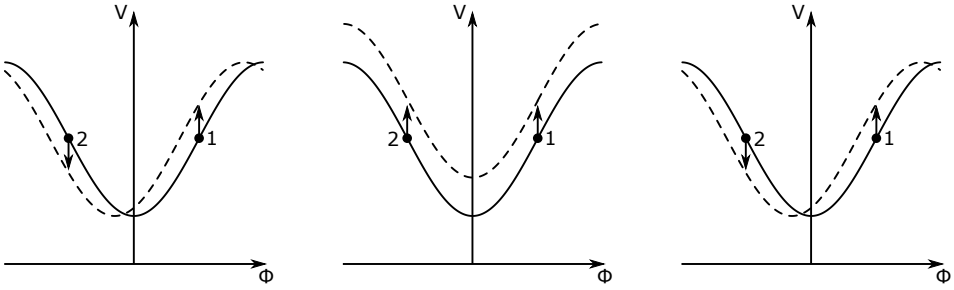

(a) Applied flux $\delta\Phi$. (b) In-phase fluctuations. (c) Out-of-phase fluctuations.

Figure 6.8: The effects of applied flux to the V–Φ characteristic of the SQUID compared to the effects of I_c,R_n fluctuations for a positive SQUID bias. The solid lines indicate the unaltered characteristic and the broken lines indicate the affected cases.

collectively referred to as I_c,R_n fluctuations, can be defined as having two parts: in-phase and out-of-phase contributions. Assume a SQUID with identical Josephson junctions. In-phase fluctuations will result in both critical currents changing identically, leading to a voltage fluctuation δV^* across the SQUID. Out-of-phase fluctuations will result in changes in the critical currents of the same size, but different polarities, resulting in an apparent flux $\delta\Phi^*$ in the SQUID. Resistance fluctuations have similar results, but are usually less significant. Figure 6.8 shows the two fluctuation contributions compared to an actual change in applied flux $\delta\Phi$ in

the SQUID. A SQUID with a direct readout FLL is biased at the fixed working point 1. The effects of the fluctuations are indicated by the vertical arrows. It is clear that for direct readout, the effect of $\delta\Phi$ is indistinguishable from both types of fluctuations. A flux modulated configuration will have the SQUID bias periodically switch between points 1 and 2. In this case, $\delta\Phi$ can be distinguished from the in-phase fluctuations, but not from the out-of-phase fluctuations, which are dominant in HTS SQUIDs. The effect of I_c,R_n fluctuations, both in-phase and out-of-phase,

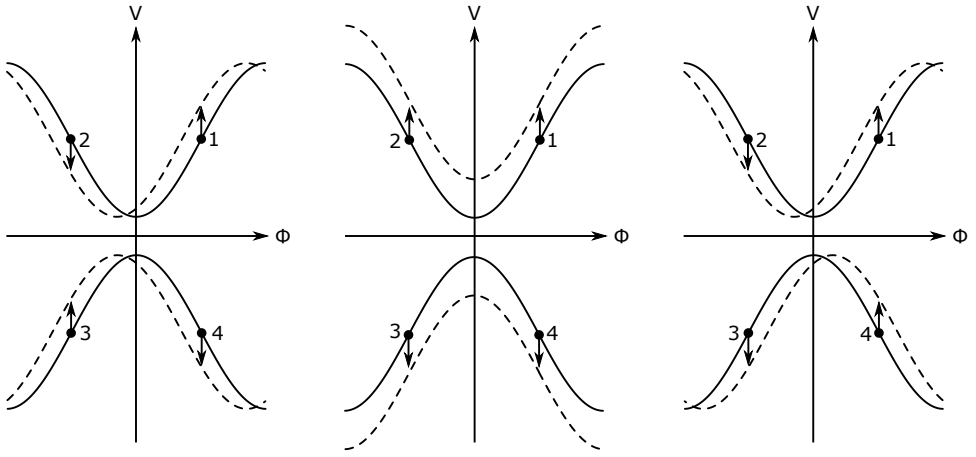

(a) Applied flux $\delta\Phi$. (b) In-phase fluctuations. (c) Out-of-phase fluctuations.

Figure 6.9: The effects of applied flux to the V–Φ characteristic of the SQUID compared to the effects of I_c,R_n fluctuations for both a positive and negative SQUID bias. The solid lines indicate the unaltered characteristic and the broken lines indicate the affected cases.

can be reduced by applying bias reversal. The effects are shown in Figure 6.9. Periodically reversing the SQUID bias will result in the working point switching between points 1 and 3 for direct readout, and additionally, points 2 and 4 for flux modulation readout. The response of the working point pairs $1 \leftrightarrow 3$ and $2 \leftrightarrow 4$ for applied flux differs from that of the I_c,R_n fluctuations. The overall result is that the net effect of the I_c,R_n fluctuations are zero while the SQUID sensitivity to applied flux is unaffected [25].

6.1.3 Simulation

In order to obtain a proof of concept for the readout electronics, a direct readout FLL with APF was simulated in *WRSPICE*, a specialised version of SPICE designed to include support for superconductive circuitry. The schematic of the simulated circuit is shown in Figure 6.10 and the SPICE code is given in Appendix B.1. For

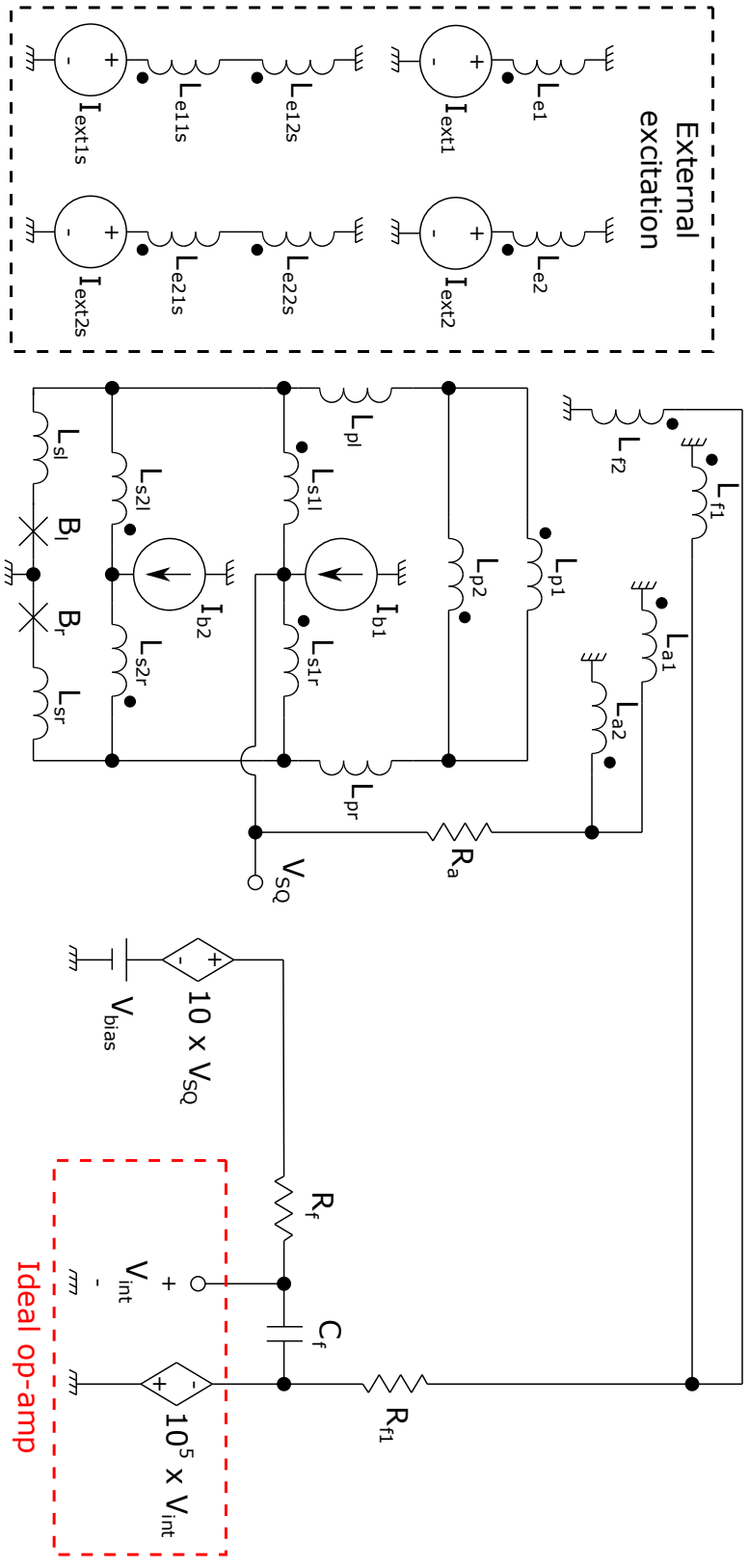

Figure 6.10: The schematic of the FLL proof of concept simulation.

clarity, the mutual inductance couplings are not shown. These are listed instead in Table 6.1.

Le1 – Lp1	1
Le2 – Lp2	1
Le11s – Ls1l	1
Le12s – Ls1r	1
Le21s – Ls2l	1
Le22s – Ls2r	1
Lf1 – Lp1	0.520
Lf2 – Lp2	0.520
La1 – Lp1	0.451
La2 – Lp2	0.451

Table 6.1: The mutual inductance coupling factors of the schematic in Figure 6.10.

The objective of the simulation was to include the spatial effects of the gradiometer, while keeping the electronic components of the FLL at an ideal level. The spatial offset of a signal across the gradiometer loops is modelled by coupling the excitation signal I_{ext1} to one side of the pickup loop, and coupling the same signal with a slight delay, I_{ext2}, to the other side of the loop. The same was done for the SQUID loop with the signals I_{ext1s} and I_{ext2s}. The excitation signals were meant to represent the typical magnetic field strength found approximately 1 metre above ground below an overhead transmission line. A typical value for the mean magnetic field density below a 115 kV line is approximately 3 μT [26].

The external excitation signal was modelled as a current source and an inductor in series. The inductor is perfectly coupled to the pickup and SQUID loops. In order to simulate a given magnetic flux density, the following relation is used:

$$LI = \Phi = BA \tag{6.1.6}$$

where L is the inductance of the circuit representing the excitation signal, I is the signal itself, B is the magnetic flux density being simulated and A is the area being threaded by the flux of the excitation signal. From Appendix A, the area of the gradiometer pickup loop can be determined as $A_p = 29.16 \times 10^{-6}$ m^2 and that of the SQUID loop as $A_s = 10.01 \times 10^{-9}$ m^2. Choosing the inductance $L = 10$ nH, then, for a magnetic flux density of $B = 3$ μT, the current I representing the excitation signal is calculated as 8.748 mA for the pickup loop and 3.003 μA for the SQUID loop.

As mentioned above, the spatial offset of the excitation signal was modelled by coupling the signal to both sides of either the SQUID loop or pickup loop, and

adding a delay to one side of the loops. The delay is calculated as

$$t_d = \frac{b}{v} \tag{6.1.7}$$

where b is the baseline of the pickup or SQUID loop and v is the velocity of propagation of the signal, which is essentially equal to the speed of light in overhead transmission lines [27, 28, 29]. For the pickup loop baseline of 2.7 mm and SQUID loop baseline of 71.5 μm (for the original G-SQUID), the delays are $t_d \approx 9$ ps and 238.5 fs respectively.

The remaining inductances and mutual inductances of the circuit were determined via FastHenry. All the feedback loops couple to the pickup loop only. The inductive couplings between the feedback loops and the SQUID loop were omited as the coupling constants were less than 0.01 and including them would have needlessly complicated the simulation. For simplicity's sake, the mutual inductances between the feedback coils of the FLL and APF were also ignored, although these should be included in more accurate simulations as the coupling factor was calculated to be quite large at 0.63.

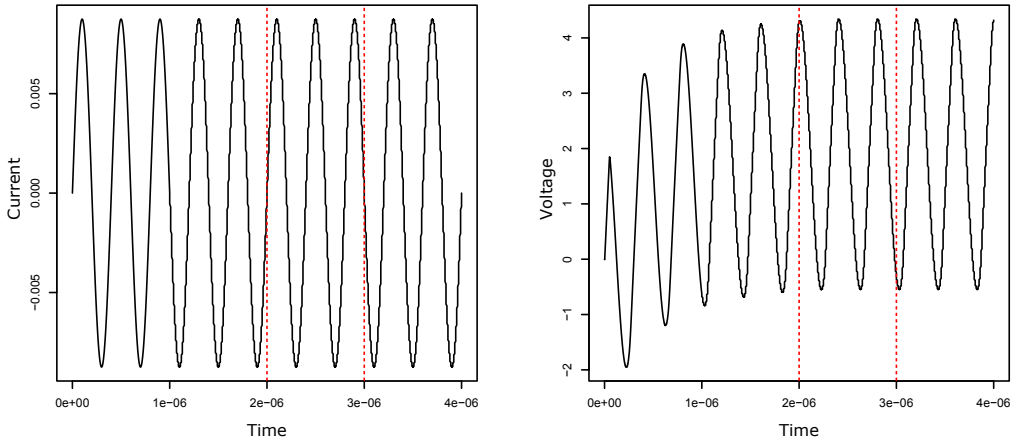

(a) The excitation signal.

(b) The output voltage of the FLL.

Figure 6.11: Simulation of a direct readout FLL with APF. The external excitation signal represents a 3 μT magnetic field oscillating at 2.5 MHz.

The simulations were performed using ideal components in order to eliminate the frequency dependency of the circuit. The components indicated by the red box in Figure 6.10 represent an ideal op-amp. Because of the high frequency effects of the SQUID, the simulations were performed using small timesteps of 1 ns. Numerous simulations were attempted with 50 Hz excitation signals, however, in order to see

the gradiometric effects, several cycles of the output signal need to be observed in order to allow the output to stabilise. Unfortunately, *WRSPICE* is not capable of performing simulations of the necessary length at the required time step resolution to be able to see the gradiometric effects on a 50 Hz signal. For this reason, a number of higher frequency signals were simulated. These signals would still be sufficient as a proof of concept since the gradiometric effects would not be frequency dependent if ideal components were used.

Two of the signals that were simulated and their results are shown in Figures 6.11 and 6.12. The first signal is a 2.5 MHz sinusoidal wave which also represents a 3 μT magnetic field. The second signal is a 1 MHz triangle wave with a peak-to-peak current swing of 20 mA. The triangle wave had to be piecewise defined.

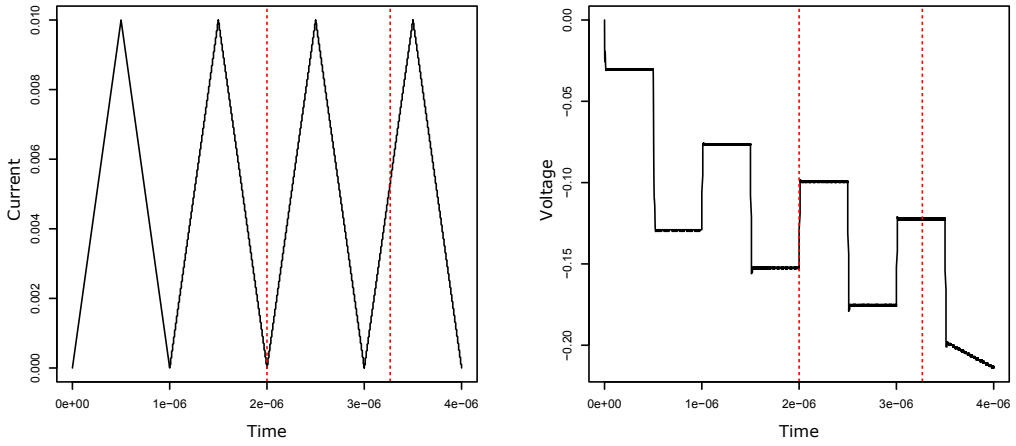

(a) The excitation signal.

(b) The output voltage of the FLL.

Figure 6.12: Simulation of a direct readout FLL with APF. The external excitation signal represents a triangle wave oscillating at 1 MHz.

The reason why waves of different shapes were simulated was to eliminate the possibility that the results of the circuit on sinusoidal waves were only phase shifts. Comparing the positions of both the input and output signals at the red lines indicated in both Figures 6.11 and 6.12 make it clear that the output of the circuit is indeed the derivative of the input.

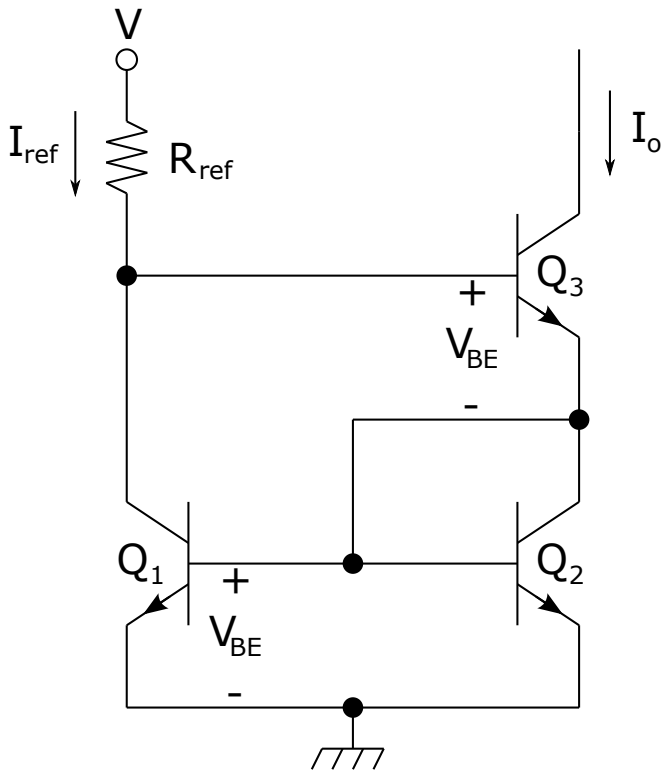

Figure 6.13: A Wilson current source. The three transistors Q_1, Q_2 and Q_3 are assumed to be identical.

6.2 Current Source

As can be seen in Figure 5.5, the voltage modulation required for flux detection only occurs when the SQUID is biased beyond its total critical current I_{Tc}. For a portable SQUID system, it is preferable that the bias current be provided by simple, compact circuitry rather than a regulated power source. A possible candidate is the Wilson current source, shown in Figure 6.13 and discussed further below, however it should be kept in mind that the type of current source utilised should be chosen based on the specifics of the application for which the SQUID is designed. Assuming that the three transistors Q_1, Q_2 and Q_3 are identical, the output current I_o is calculated to be

$$I_o = I_{ref} \times \frac{1}{1 + \frac{2}{\beta(2+\beta)}} \tag{6.2.1}$$

where β is the common-emmiter current gain [30]. The reference current I_{ref} can be calculated as

$$I_{ref} = \frac{V - 2V_{BE}}{R_{ref}} \tag{6.2.2}$$

where the base-emitter voltages V_{BE} are assumed to be equal. The resistor R_{ref} is thus the defining component of this circuit.

Consider a SQUID with two identical Josephson junctions, each with a critical current of $I_c = 100\ \mu$A. It is decided to bias the SQUID with a current of $I_{Tc} = 250\ \mu$A from a Wilson current source. Assuming that three identical 2N2222 bipolar transistors are used, each with a DC current gain of 200 and base-emitter voltage of $V_{BE} = 0.6$ V which are typical values for such transistors [31], and that the current source is powered by a 9 V battery, the resistor can be calculated as $R_{ref} \approx 31.2\ \text{k}\Omega$, which is a reasonable value.

6.3 Output Filter

In order to assist in isolating the desired 50 Hz signal, a bandpass filter can be applied to the output of the flux-locked loop. A general design for such a filter is shown in Figure 6.14 [32] and further discussed, although it should once again be noted that more specific filter designs should be implemented if more information can be aquired about the specifics of the device application and the physical properties of the SQUID.

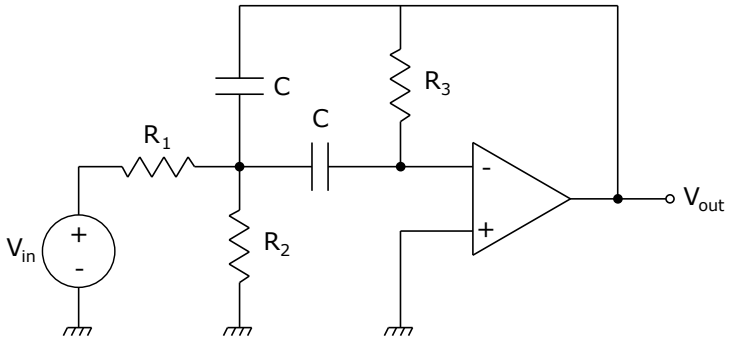

Figure 6.14: A narrowband bandpass filter.

Although it is possible to design a bandpass filter by utilising high-pass and low-pass filters in cascade, such filters typically have low *quality factors* (the ratio of the filter's centre frequency to its bandwidth). Designing the filter for a given frequency requires that one decide on the quality factor Q and the passband gain K in order to determine the values of the resistors. Capacitors are typically chosen to be a convenient, readily available value.

The resistors are calculated as follows [32]:

$$R_1 = \frac{Q}{K} \tag{6.3.1}$$

$$R_2 = \frac{Q}{2Q^2 - K} \tag{6.3.2}$$

$$R_3 = 2Q. \tag{6.3.3}$$

Note that these values are not scaled for the desired parameters. Resistors are scaled by multiplying their impedance values by a factor k_m, such that $R' = k_m R$, where R is the unscaled resistance as calculated from the above equations and R' is the adjusted value. Capacitors are also scaled in this fashion, however, since the impedance of capacitors are also affected by frequency, an additional scaling factor k_f is also required such that $C' = \frac{C}{k_m k_f}$, where C is the unscaled capacitance of 1 farad at 1 Hz and C' is the desired capacitance. The value of k_f is simply the chosen

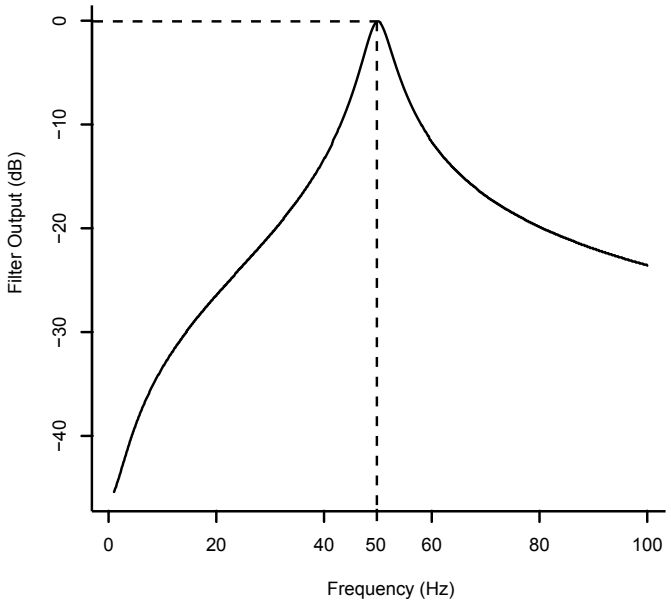

Figure 6.15: The output of the bandpass filter as a function of frequency. The unity gain at 50 Hz, although less than expected, is still sufficient for the SQUID output.

frequency of the filter in radians. Thus, k_m can easily be calculated via substitution and subsequently the resistances as well [32]. The final values of the filter is given in Table 6.2.

The filter was simulated in WRSPICE and the results are shown in Figure 6.15. The passband gain is less than that for which the circuit was designed, a fault most

Centre frequency	50 Hz
Quality factor (Q)	10
Passband gain (K)	2
C	1 μF
R_1	15.915 kΩ
R_2	160.763 Ω
R_3	63.662 kΩ

Table 6.2: The final scaled values of the bandpass filter.

likely attributable to the LF351 op-amp. It is nonetheless still sufficient. The SPICE code is given in Appendix B.2.

Chapter 7

Manufacturing of a SQUID

This chapter deals with the processes involved in the fabrication of a thin film superconducting device. The fundamental processes are first discussed, followed by the specific fabrication aspects of the project design.

7.1 Photolithography

Photolithography can be described as the process wherein an image or pattern is transferred from a mask onto a thin film. The basic steps are illustrated in Figure 7.1. They consist of resist application, exposure, development, etching and resist removal.

- *Resist application*: The first step in the process, shown in Figure 7.1(a), is to deposit a thin layer of photoresist onto the film. This is typically performed by applying a few drops onto the film, then spinning the film at a high speed, typically 1500 - 8000 rpm, in order to uniformly distribute the resist across the film surface. The speed used is dependent on the photoresist being used and the desired thickness. An emperical expression for the thickness T is

$$T = \frac{KC^{\beta}\eta^{\gamma}}{\omega^{\alpha}} \tag{7.1.1}$$

  where C is the polymer concentration in a g/100 mℓ solution, η is the intrinsic viscosity, ω is the rotations per minute and K is the overall calibration constant [33]. α, β and γ are exponential factors that must also be determined. After the spin coating, the film must be soft baked or prebaked to remove any remaining solvents, of which there can be up to 15%, and built in stresses, as well as improve the adhesion of the resist.

- *Exposure*: The film is now transferred to an exposure system. Care must be taken to properly align the mask with the film, especially if the current pho-

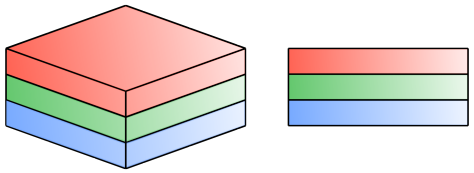

(a) Photoresist application.

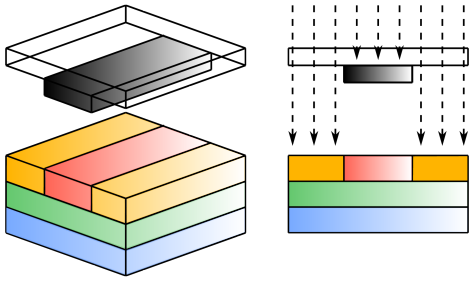

(b) Exposure.

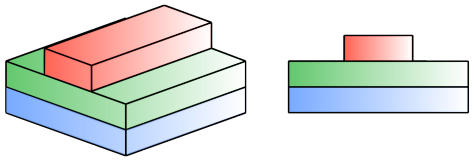

(c) Development.

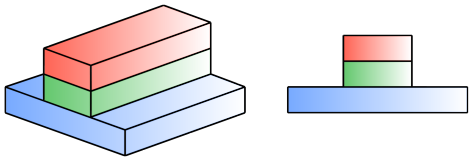

(d) After etching.

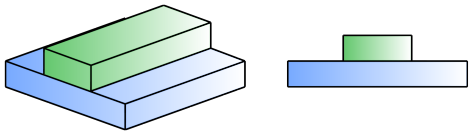

(e) Photoresist removal.

Figure 7.1: The basic steps involved in the photolithography process. In all cases, the substrate is indicated in blue, the superconducting film in green, and the photoresist in red. The mask is indicated in (b) as a transparent plate with an opaque pattern. The broken lines indicate the UV radiation. Finally, the exposed parts of the resist is indicated in orange.

tolithography process is intended for the second or later layer of a multilayer device. The alignment system must preferably be capable of an alignment resolution of a fraction of the smallest feature size on the mask. The exposure system consists of a UV lamp that illuminates the film through the mask, as shown in Figure 7.1(b). More advanced exposure systems may contain lenses to improve the process. The exposed areas of the resist will undergo a che-

mical reaction due to the radiation. This will alter the solubility of the resist. Postexposure treatments may be required, depending on the development method and type of resist used. Such treatments include postexposure baking, vacuum treatment, exposure to other types of radiation and reactive gas treatment. Calibration of the exposure system is crucial, as proper intensity, directionality, spectral characteristics and uniformity across the film of the UV light is essential for perfect pattern transfer.

- *Development*: The development phase is where the image is formed in the resist as a relief pattern, as can be seen in Figure 7.1(c). This is accomplished by selective dissolving of the resist. Whether it is the exposed or unexposed areas of the resist that dissolve depends on whether positive or negative tone resist is being used. The exposed areas of positive tone resist will dissolve and the unexposed areas will remain. This is reversed for negative tone resist. If any unwanted resist remain after development, one may consider de-scumming, a mild oxygen plasma treatment that removes the unwanted resist.

  After development, the film must be postbaked, or hardbaked. This process removes any residual solvents and anneals the film to improve the resist adhesion which may have been weakened by the developer. Depending on the etching method utilised, it may be necessary to periodically interrupt the etching process to further hardbake the film for a few minutes in order to prolong the resist lifetime during the entire etching process.

- *Resist removal*: Once the film has been etched, as shown in Figure 7.1(d), the final step in the photolithography process is to remove the remaining photoresist from the film. This process is also known as stripping, the result of which is shown in Figure 7.1(e). It is important that the resist be removed without damaging the film. A variety of liquid strippers are available for this purpose. Acids, such as H_2SO_4, organic solvent strippers and alkaline strippers are all possibilities depending primarily on how it would affect the film. Acetone can also be used, but it will not be effective if the postbake was too long or at too high a temperature.

  As an alternative to using liquid strippers, it is also possible to use dry stripping or oxygen plasma stripping, also referred to as ashing. Dry stripping is more controllable than liquid stripping and presents less toxic or otherwise hazardous materials to be disposed.

Many types of photoresist exist, but the basic concept remain the same. Photoresist consists of a polymer, a casting solvent, and optionally, a sensitiser. Radiation

changes the structure of the exposed polymer. The solvent allows the formation of thin layers via spinning. Sensitisers control the photochemical reactions in the polymeric phase. The selection of resist type depends on the application for which it is to be used.

As most are polymers, photoresists have a glass temperature T_g, above and below which they exhibit different behaviours. Below T_g, the polymer behaves as a glass. Above T_g, it behaves as a rubber. Softbaking is easier when the resist is in the rubber state, as it becomes easier to remove the solvent from the polymer matrix. However, it is also easier for the resist to pick up impurities in the rubber state, therefore, photolithography must be performed in a clean working environment, preferably a clean room.

Various methods of transferring the image from the mask onto the photoresist exist. The masks are typically designed for a given method. *Hard contact* masks, or simply *contact masks*, make direct physical contact with the resist. These have the shortest lifetime due to wear and are not suitable for VLSI applications. *Soft contact* masks, also known as *proximity masks*, are slightly raised above the resist during exposure, in the range of 10 - 20 μm. The methods employing hard and soft contact masks are collectively known as *shadow printing*. A more reliable method than shadow printing is to project an image of the mask onto the resist via a high-resolution lens system. This is known as *projection printing* and yields the longest mask lifetime, limited only by operator handling [33].

7.2 Thin Film Deposition

7.2.1 YBCO

The superconducting material used throughout this work is $Y_1Ba_2Cu_3O_{7-\delta}$, also known as YBCO, which is the most popular High-T_c superconductor used today. A variety of methods can be employed to deposit YBCO thin films. Regardless of the method chosen, two important idiosyncrasies of YBCO need to be considered when performing the deposition: the substrate temperature must be 690° or higher for proper c-axis growth [34] and YBCO is sensitive to oxygen diffusion which, if not addressed during deposition, will result in a high δ [35]. Higher values of δ lead to lower critical temperatures. If δ becomes too high, YBCO becomes a semiconductor [36].

7.2.2 Sputter Deposition

Sputter deposition is defined as a process wherein atoms are ejected from a condensed matter source via momentum exchange from impinging energetic particles

(*sputtering*) which are used as the source material for thin film growth [37]. Sputtering processes can be divided into four major categories: DC, RF, reactive and magnetron. There are variants in each category as well as hybrids between them, such as DC magnetron. The configuration common to all of these processes is the diode configuration consisting of an anode and cathode. The target material forms the cathode [38].

The simplest of the sputtering techniques is DC sputtering. The schematic of a basic DC sputtering system is depicted in Figure 7.2. The chamber is initially

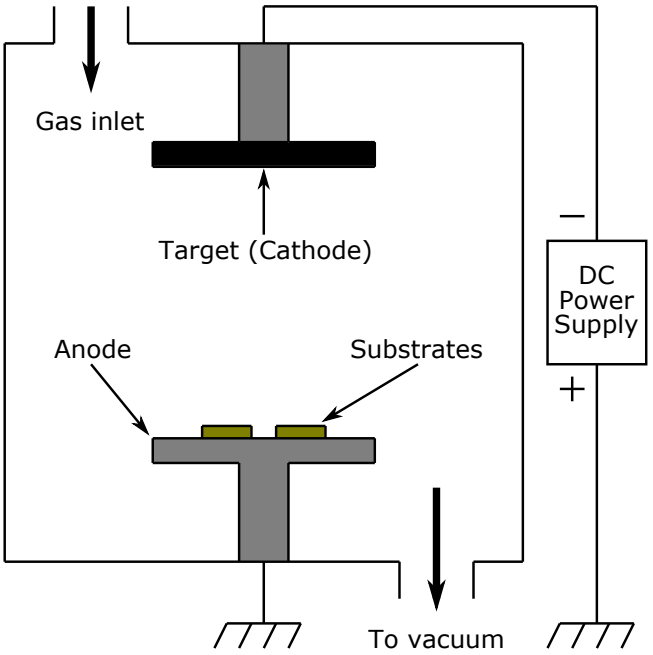

Figure 7.2: A basic DC sputtering configuration.

brought under vacuum, after which a specific gas is fed into the chamber. The elctrodes are connected to a dc power supply, typically capable of supplying up to several kilovolts. Electrons are ejected from the target surface which collide with the gas atoms, thereby ionising the gas. The positive gas ions created in the plasma bombard the surface of the target, ejecting atoms of the target material via a physical momentum exchange process. These atoms then condense of the substrate surface, causing the film growth.

Inert gases are typically chosen to create the plasma, as they do not react with the sputtering target. Argon is a popular choice, due to its low cost, although xenon and krypton may give higher sputtering yields.

DC sputtering suffers from the limitation that the sputtering target must be an electrical conductor. In order to sputter non-conductive materials, RF sputtering must be utilised. The physical setup is similar to a DC sputtering configuration, with the only difference being that the DC source is replaced by an RF source with a matching network. Electrons are reflected back and forth between the electrodes, which causes the ionisation of the gas [37].

Pure DC sputtering is not a practical technique for thin film production, as the deposition rates are very low [38]. A variety of options exist to increase the deposition rates, the most popular of which is DC magnetron sputtering, which is also employed at the laboratories of the Engineering Faculty of the University of Stellenbosch. The magnetic field introduced by the magnetron confines the plasma discharge close to the target surface [39].

Figure 7.3: The inverted cylindrical magnetron (ICM) sputtering deposition chamber used to deposit YBCO at the Engineering Faculty.

As previously mentioned, YBCO deposition is prone to oxygen loss. In order to prevent this, oxygen is also introduced during the sputtering process alongside argon as a reactive gas. This introduces a new problem. The oxygen may form O^- ions that accelerate away from the cathode and impinge upon the substrate where resputtering of the deposited material may occur [40]. This could potentially damage the crystal structure of the film. The problem can be overcome by placing

the substrate perpendicular to the face of the sputtering target [39]. This off-axis configuration, when used with a hollow cylindrical target, as is the case at Stellenbosch, is known as an *inverted cylindrical magnetron* (ICM) configuration. The ICM chamber used in this thesis is pictured in Figure 7.3.

7.2.3 Pulsed Laser Deposition

Pulsed laser deposition (PLD) is one of the simplest techniques available for thin film deposition. It can be used to deposit almost any kind of material, although its popularity only started to rise when it was found to be a simple and efficient method of depositing HTS films, whereas other methods at the time imposed strong limitations as to the quality of such films.

The two primary components of PLD are a pulsed laser source and a deposition chamber. An advantage of PLD is that the laser and deposition chamber remain seperate. It is not necessary to have the two components integrated as one piece of hardware. The laser must be placed to allow the laser beam to focus onto the surface of the target. The angle of the beam is typically 45°, although this value is not critical [1].

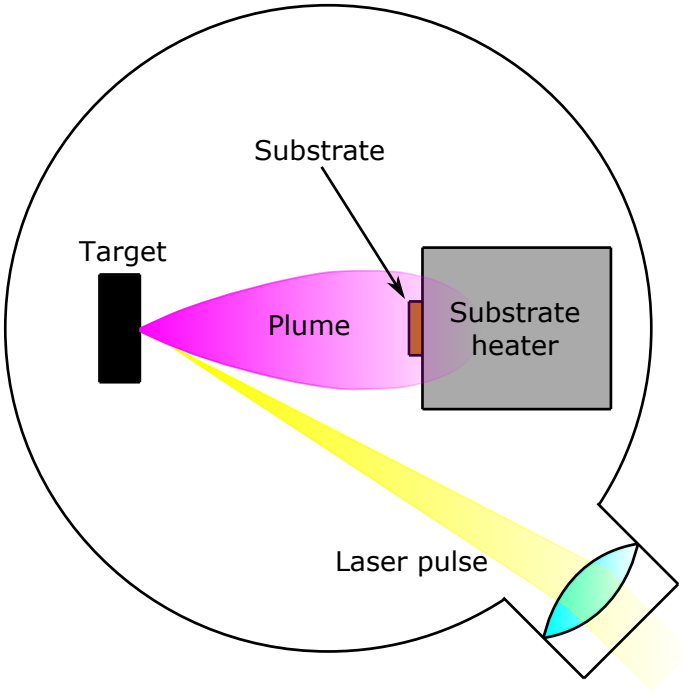

Figure 7.4: Basic operation of a PLD.

Figure 7.4 displays the basic operation of a PLD. The laser is focused via lenses onto the target surface, converting a thin layer of the target into the vapor phase, forming a highly directional plume of ablated material. This plume is propelled towards the substrate, allowing film growth to take place [38]. The substrate is located in the same chamber as the target, typically placed parallel to each other. The substrate holder may consist of a controlled heater, to accommodate the necessary crystal growth conditions. The target must be continuously rotated or otherwise moved during the deposition to ensure that it is being evenly utilised [1]. The PLD used at the University of Stellenbosch is shown in Figure 7.5.

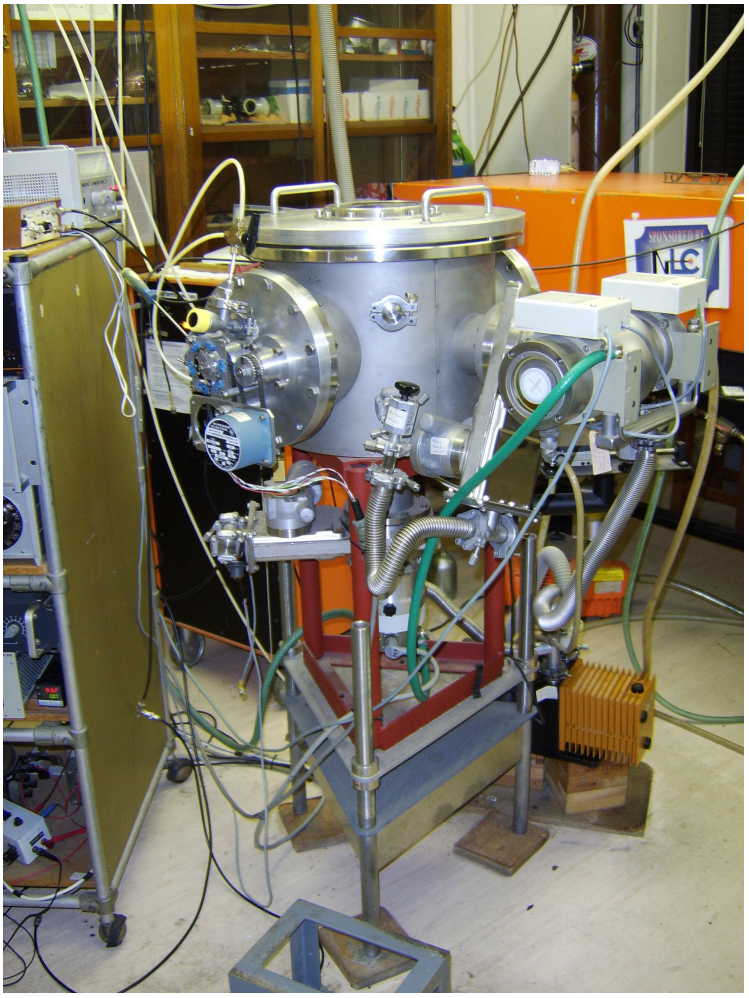

Figure 7.5: The pulsed laser deposition system used at the University of Stellenbosch.

7.3 Atomic Force Microscopy

The imaging of individual atoms only first became possible with the invention of the *scanning tunneling microscope* (STM) in 1981. The STM operates by allowing a tunneling current to form between its biased tip and the sample. This method of operation presents an obvious flaw: the sample must be conductive. Fortunately, early experiments indicated that if the tip was close enough to the sample to allow a tunneling current to flow, significant forces would act collaterally with the current. These forces would then form the basis of the *atomic force microscope* (AFM). AFMs have the significant advantage of being able to create an image of the surface of any sample, regardless of conductivity. The AFM used at the University of Stellenbosch, a Nanosurf *easyScan 2* AFM, is pictured in Figure 7.6.

The primary difference between an AFM and an STM is the probe tip. Therefore, the principles of AFM operation are best described by comparison to that of STMs. The tip of an STM is mounted on a scanning device capable of scanning in the x, y and z directions with subatomic precision. The sample is biased with a voltage V_t. When the tip is brought close enough to the sample, typically in the range of several angstroms, a tunneling current I_t will flow between the tip and the sample which is used as a feedback signal. Images are created in one of two ways: *topographic mode* or *constant-height mode*. In topographic mode, the surface is scanned in the x–y plane, while z is adjusted to keep I_t constant. In constant-height mode, the scanning is performed faster than the feedback is capable of following the atomic corrugations, resulting in z remaining constant. The atoms will cause I_t to vary, which is used to form the image. The two three-dimensional images are $z(x, y, I_t \approx \text{constant})$ or $I_t(x, y, z \approx \text{constant})$.

In an AFM, the tip typically consists of a force-sensitive cantilever, although many other tips exist that are made for AFMs. Two modes of operation are used with AFMs: *static force* and *dynamic force*. When operated in static force mode, the deflection of the cantilever that is caused by the force acting between the tip and the sample is used as the feedback signal. When dynamic force operation is utilised, the cantilever is subjected to vibration. Elastic and inelastic interactions between the tip and the sample will change the amplitude and phase of the vibrating cantilever relative to that of the driving signal. It is these changes that form the feedback signal [41].

7.4 Argon Ion Mill

Etching can be defined as pattern transfer via chemical or physical removal of material from a substrate. Ion beam etching/milling (IBE/IBM) is a form of etching

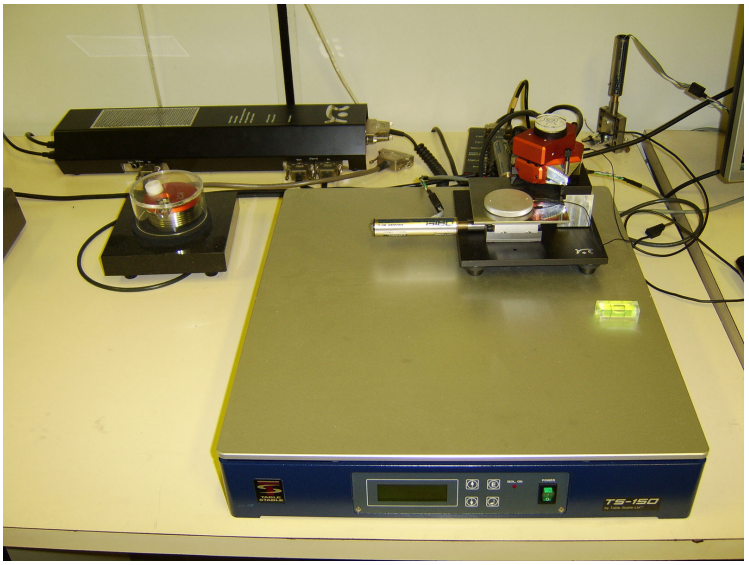

Figure 7.6: The Nanosurf easyScan 2 AFM.

that utilises a triode configuration where plasma is generated in a specific chamber. Ions are extracted from this chamber via an extraction grid system and directed in a beam toward the substrate in a seperate chamber. The dual chamber setup is illustrated in Figure 7.7.

Both DC and RF plasma sources can be used. RF plasma sources function in the same way as mentioned in Section 7.2.2. The RF frequency used almost universally is 13.56 MHz, a frequency that does not interfere with radio transmitted signals. Magnets are used to help confine the plasma to the centre of the chamber via magnetic fields, preventing electron loss to the chamber walls.

In order for etching to take place, the kinetic energy of the bombarding particles must fall within a specific range. Below 3 eV, the particles will be reflected or physisorbed. From 4 to 10 eV, surface migration and damage occurs. In the range of 10 to 5000 eV, the substrate becomes heated, and surface damage and material ejection occurs. Ion implantation (doping) takes place from 10 keV onward. The effects are summarised in Table 7.1.

Ion energy (eV)	Effect
<3	Physical adsorption
4 – 10	Minor surface sputtering
10 – 5000	Sputtering
>10000	Implantation

Table 7.1: Energy requirements of different effects of ion bombardment.

The etching process is subject to various phenomena that may result in imperfect

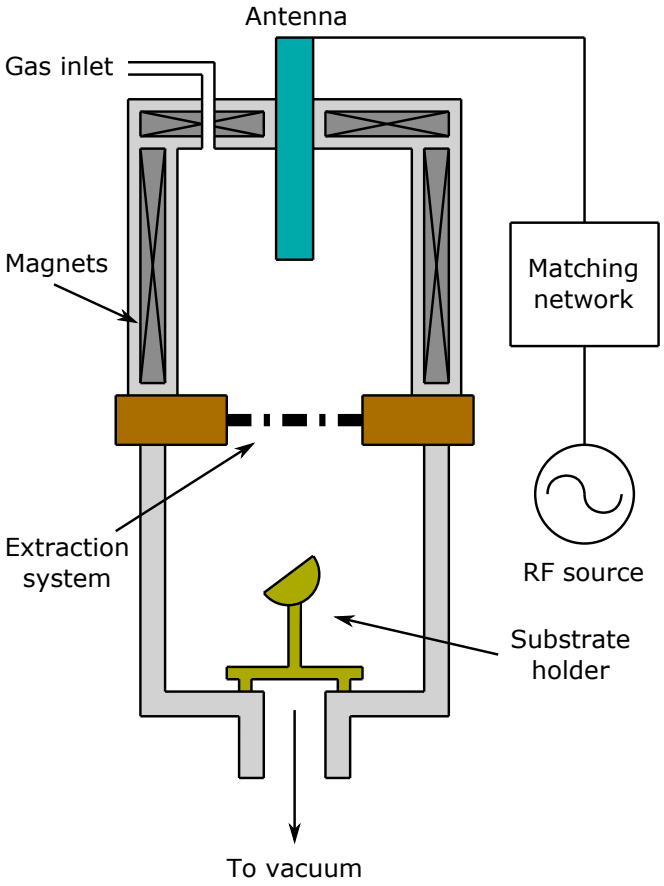

Figure 7.7: A schematic of an ion mill in a triode configuration using an RF plasma source [1].

pattern transfer. A number of these phenomena are listed below:

- *Faceting*: Even perfectly vertical mask walls will have a slightly rounded corner that etches faster than the rest of the mask. This leads to the development of facets in the mask edges, as shown in Figure 7.8(a). These facets cause subsequent facets to form in the etched substrate features as well.
- *Trenching*: Mask walls that are not perfectly vertical will have ions collide at glancing angles leading to a local increase in the etch rate and, subsequently, the formation of trenches along the walls, as shown in Figure 7.8(b).
- *Redeposition*: Involatile species that were sputtered from the bottom of an etched feature may settle on the mask sidewalls. The result is pictured in Figure 7.8(c).

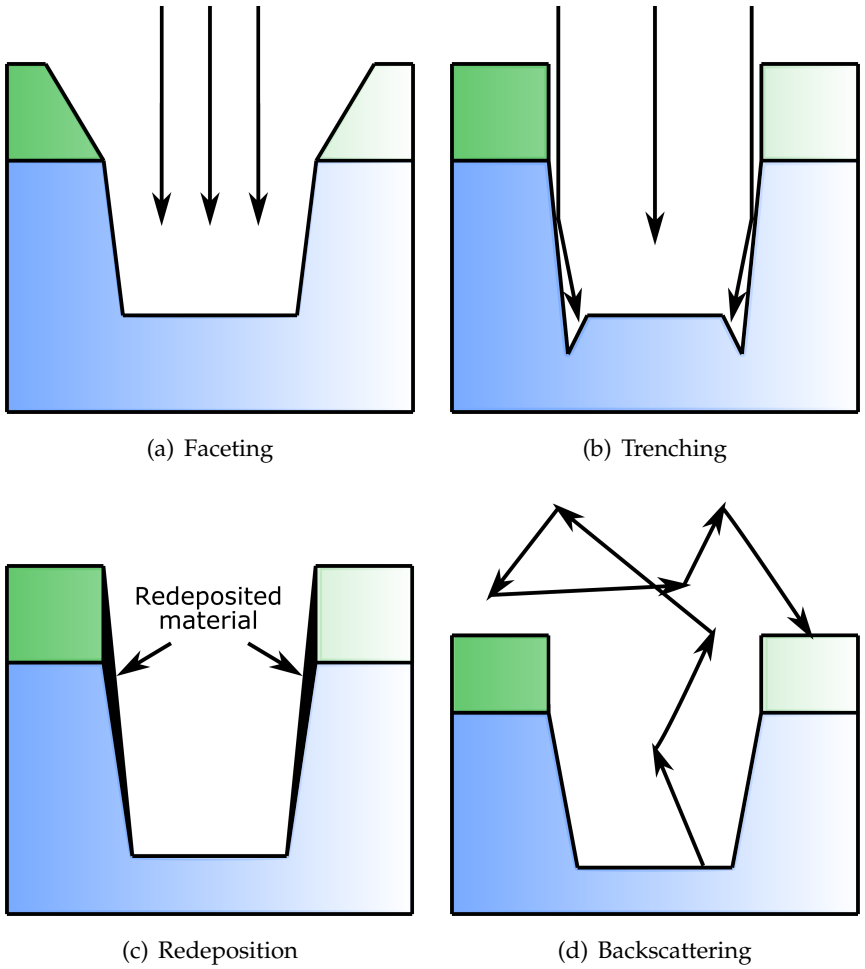

(a) Faceting (b) Trenching

(c) Redeposition (d) Backscattering

Figure 7.8: Examples of the various imperfections that may occur during etching. In all examples, the substrate is indicated in blue, and the mask in green.

- *Backscattering*: Backscattering is a form of redeposition where a fraction of the sputtered species from the surface undergoes several collisions with the gas phase species and then backscatters onto the substrate. The effect is shown in Figure 7.8(d). This form of redeposition may include contaminants from the vacuum chamber walls or fixtures.

The effects that cause these imperfections are normally detrimental to the overall etching process, however they can be exploited for certain applications [33].
The mill used at the University of Stellenbosch is shown in Figure 7.9. Comparison with Figure 7.3 will reveal that the chamber in which the substrate is located is the same one used in the ICM. This chamber is interchangeably used for both systems. The ICM and argon ion mill both exist as seperate chamber "heads". Converting from one system to another merely requires that the head and substrated holder be

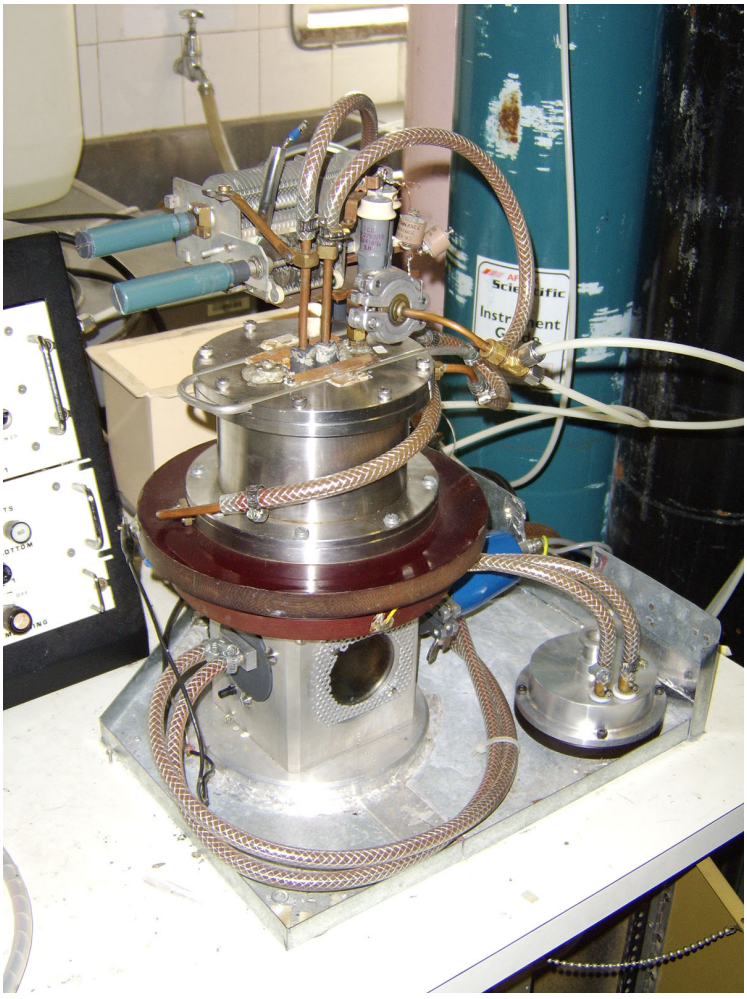

Figure 7.9: The Argon Ion Mill used at the University of Stellenbosch.

swapped out for the other. The mill head also contains the matching network for the RF source. Operation of the mill requires an RF shield to be placed over the mill during an etching process. The RF source is connected to the matching network via connecting wires in the shield.

7.5 Specific Manufacturing Processes of Different Types of SQUIDs

7.5.1 Step-edge Junction Fabrication

Step-edge junctions are a very attractive choice of Josephson junction due to the topological freedom that they allow, while being comparatively simple to manufacture. The standard model used when fabricating a step-edge junction is pictured in Figure 7.10. The important angles to consider are the substrate holder tilt

angle α, the substrate rotation angle β, the off-normal angle of the ion beam with the photoresist γ, and the side wall angle of the photoresist χ. The effects of each of these angles depend on whether the orientation of the resist edges are parallel or perpendicular to the ion beam, although, in general, it is desirable to have χ as close to 90° as possible, regardless of the orientation. Different materials have different etch rates, therefore, carefully choosing the orientation and angles is critical when creating step-edges.

In the parallel orientation, where β is held constant, only the etch rate of the substrate can be varied (by α) as γ is always constant regardless of α. Certain values of α may lead to the formation of trenches or redeposited material which could result in extra misorientation angles in the step-edges, which result in increased junction noise.

In the perpendicular orientation, where the resist side wall faces the ion beam, γ is inversely proportional to α. β will now also have an effect on γ, allowing for further fine tuning. The angles must be chosen such that the substrate etch rate does not become too low relative to the photoresist etch rate. When this happens, the photoresist will be etched away before a decent step is created [42].

Both gradiometer designs shown in Figures 5.7 and 5.8 are eligible for step-edge junctions along the broken lines. The second design is the easiest to implement, as it requires only a simple step down the centre of the substrate. The first design is not as simple to realise. Since the two Josephson junctions need to be identical, the only way to implement the step-edges is by milling the step in the parallel orientation discussed above, limiting the available options for improving the step

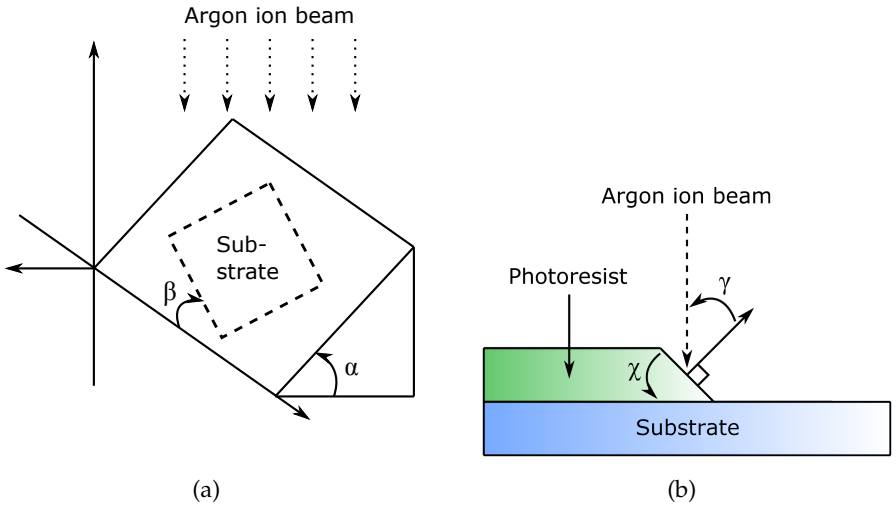

Figure 7.10: The important angles during step-edge fabrication.

angles. Chapter 8 discusses the viability of using step-edges in these designs.

7.5.2 Bridge Constriction Junction Fabrication

Both gradiometer designs are once again eligible for bridge constriction junctions, or nanobridges, although the original G-SQUID design is a better candidate due to its simpler layout.

Two fabrication methods were attempted. The first method involved using a laser provided by the Stellenbosch University Department of Geology to cut the restrictions into the YBCO tracks. Unfortunately, the laser was severely uncalibrated at the required resolution and could not be recalibrated for a considerable time. The second method involved using the nanolithography functionality of the Nanosurf *easyScan 2* AFM to scratch the constrictions into the YBCO tracks.

The AFM scratching method involved two approaches. First was to scratch the YBCO after the tracks had been milled, and second was to scratch the photoresist pattern before the YBCO was milled.

The first approach had been attempted once before by Elkaseh [43], however this was done using a different AFM and different AFM tips. Therefore, the process had to be attempted without prior guidelines. The second approach had not been attempted before at Stellenbosch University. The testing methodology involved using different types of photoresist with varying parameters during the photolithography process. Of primary importance was minimising the thickness of the

Spinning speed	9000 - 1000 rpm
Softbake time	60 - 80 seconds
Softbake temperature	90°C
Exposure time	30 seconds
Development time	50 - 60 seconds

Table 7.2: General parameter set used during testing of photoresist AFM constriction junctions.

photoresist layer, since it becomes too difficult to scratch through the entire layer if it is too thick. The AFM tip could also be damaged by attempting to scan features that are too large.

The parameter set utilised for photoresist AFM scratching is given in Table 7.2. The results of both AFM lithography approaches are given in Chapter 8.2.2.

7.6 Buffer Layer

A problem that often occurs when attempting to fabricate step-edge junctions is that the substrate into which the step has to be etched has too low an etch rate for a proper step to be formed. The result is that either the step angle, step height, or both are too low for a Josephon junction to form. A common solution to this problem is to first deposit a buffer layer into which the step can be etched, as illustrated in Figure 7.11. It is important that the buffer layer allow further epitaxial growth of the intended superconductor, in this case YBCO.

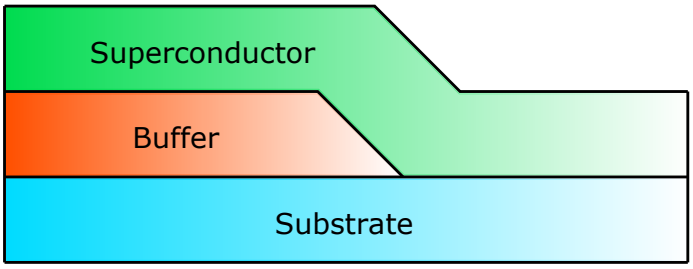

Figure 7.11: A buffer layer is used to create the epitaxial template for a step-edge junction.

The materials considered for buffers for this thesis was $PrBa_2Cu_3O_{7-\delta}$, also known as PBCO, which was successfully implemented as a buffer layer for step-edge junctions by Van Staden [44] as well as YBCO itself. As PBCO is not an electrical conductor, deposition had to be performed via PLD.

An attempt was made to convert the existing ICM system to allow RF sputtering, which would allow non-conductive material sputtering at the engineering laboratory. This attempt involved removing the RF matching network from the argon ion mill chamber head, and attaching it to the RF shield, allowing the network to be available to both the argon ion mill and ICM chamber heads. Unfortunately, the difference in length of the connecting wires between the matching network and the two chamber heads compared to the original lengths for just the argon ion mill resulted in a severe impedance mismatch that could not be addressed by the matching network alone. It was deemed that, although possible, the RF conversion could not be performed without a major redesign of the chamber setup, the replacement of which would have inconvenienced many researchers at that time.

YBCO was also considered for a buffer layer. These attempts involved oxygen depleted YBCO, which was deposited without oxygen and without the annealing phase. This decision was based on the idea that the buffer layer does not need to

be superconducting itself, and that the process would save oxygen reserves. The results are discussed in Chapter 8.2.1.

Chapter 8

Results

This chapter discusses the results of various aspects of the thesis, as well as detailing many of the problems that were encountered along the way.

8.1 YBCO Deposition

Only the ICM was used to deposit YBCO. The films were deposited at a total gas pressure of 280 mTorr consisting of both argon and oxygen in a 1:1 ratio. The substrate was heated to 740 °C. Deposition lasted 75 – 80 minutes, followed by an annealing phase of 30 minutes at 460 °C and 1 atm pressure. The substrate temperature was controlled using a heater controller, with the heater profile shown in Figure 8.1.

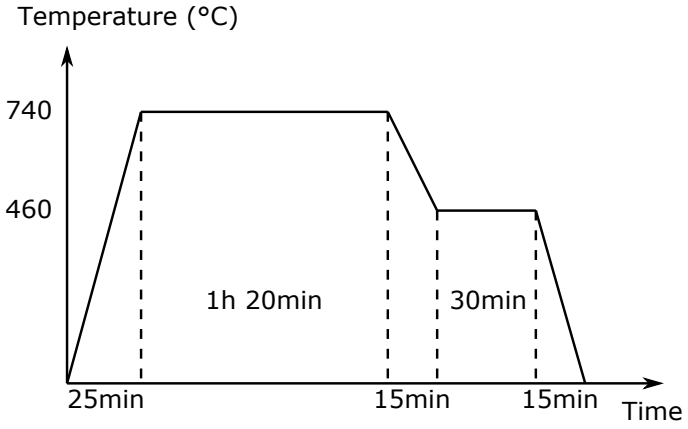

Figure 8.1: The substrate heater profile used during YBCO deposition.

Conductive silver paste was used to maximise the heat conduction to the substrate,

however care had to be taken when applying the paste, as too little would result in uneven deposition, and too much would risk the paste bubbling over onto the substrate, as well as making it difficult to remove the substrate without breaking it. An attempt was made to eliminate the necessity of the silver paste by coating the substrate holder with gold before each deposition, however this proved fruitless as the surface of the holder became less even after each deposition.

Three of the deposited samples are shown in Figure 8.2. These three samples were deposited under the exact same conditions, yet from the reflections it can be seen that the surface profile of the rightmost sample differs greatly from the remaining two. It is currently unknown as to what exactly causes these inconsistencies during deposition, however a possible cause has been identified. Observing the pressure gauge while the substrate is heating up to 740 °C reveals that the vacuum weakens by a few milliTorr. It is speculated that some part of the substrate heater, possibly a connecting wire, might be singeing during the heating phase, causing unreliable pressures in the deposition chamber.

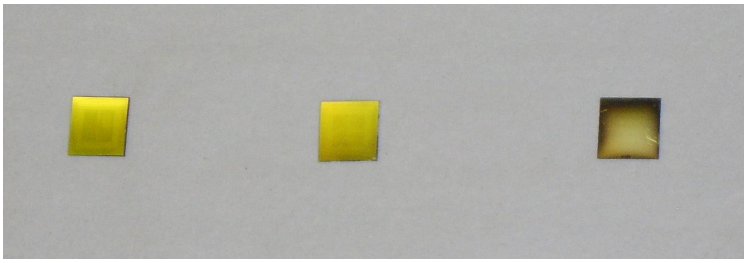

Figure 8.2: Three YBCO samples deposited under the same conditions. From the reflections it can be seen that the sample surfaces vary greatly, despite being deposited under identical conditions.

The susceptibility tests for the three samples are shown in Figure 8.3. It should be noted that the temperature sensor circuitry of the susceptibility meter was faulty, resulting in incorrect temperature measurements below 115 K. Therefore, it is uncertain as to the exact critical temperatures of the three samples. It was assumed that the fault only resulted in a temperature offset, with the relative temperature differences being accurate. In this case, the transitions from the normal to superconductive state of the three samples are very good, with a transition of 80 – 0% susceptability in approximately 0.5 K for the first sample.

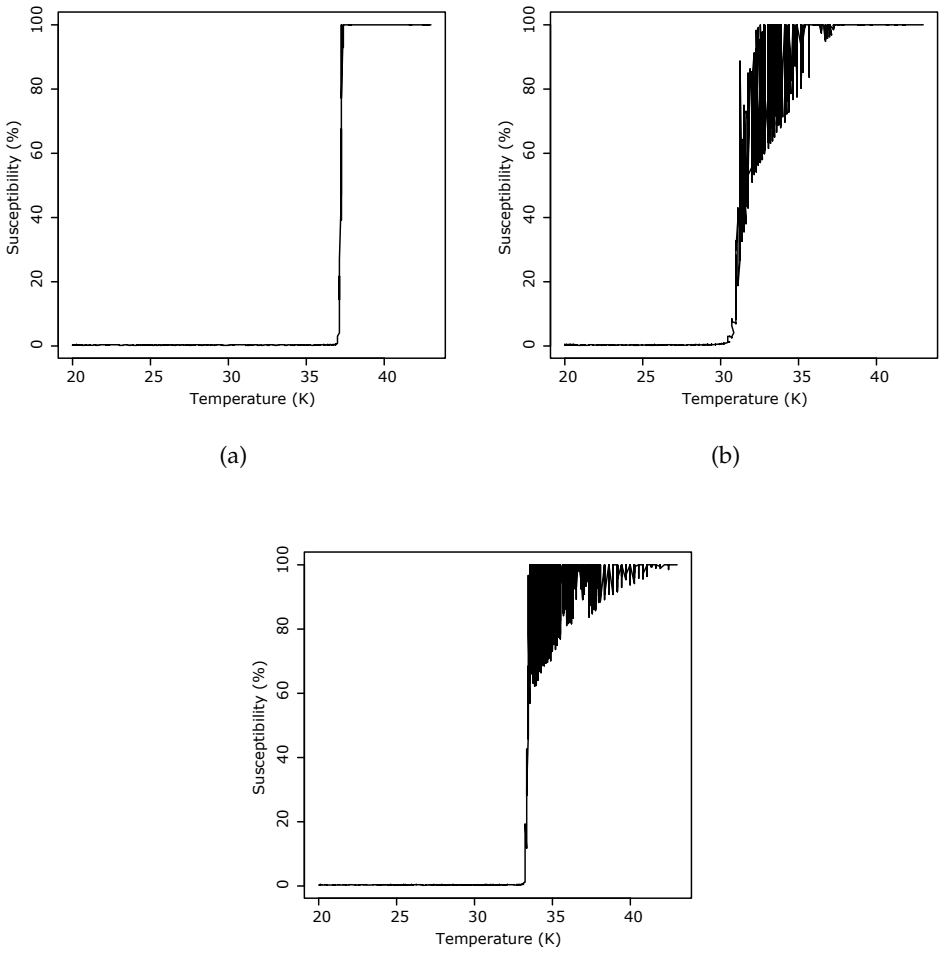

(a) (b)

(c)

Figure 8.3: The susceptibility tests of the three samples shown in Figure 8.2. The susceptibility meter had faulty temperature sensor circuitry, resulting in incorrect temperature measurements below 115 K.

8.2 Josephson Junctions

8.2.1 Step-edge Junctions

The first step-edge fabrication tests were performed on the readily available MgO substrates. The etch rate of the substrates was simply too low, achieving typical step angles of only 2 – 3 degrees. It was therefore decided to use a buffer layer. PBCO was first chosen as buffer material due to the promise it showed in Van Staden's work [44]. Initial tests were disappointing, resulting in step profiles as seen in Figures 8.4 and 8.5, which were meant for use with the original and alternative G-SQUID designs respectively. The profile of the step in Figure 8.4 is very uneven,

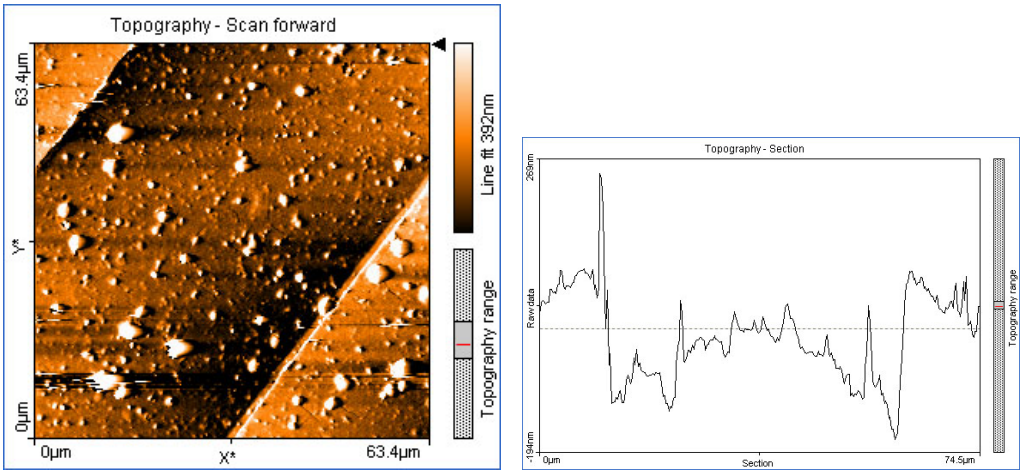

(a) (b)

Figure 8.4: AFM scan showing the step profile of an early PBCO sample intended for use with the original G-SQUID design.

making it difficult to measure the step angles. The step was approximated to be 10 degrees, much less than that reported by Van Staden. Trenching is also visible. The

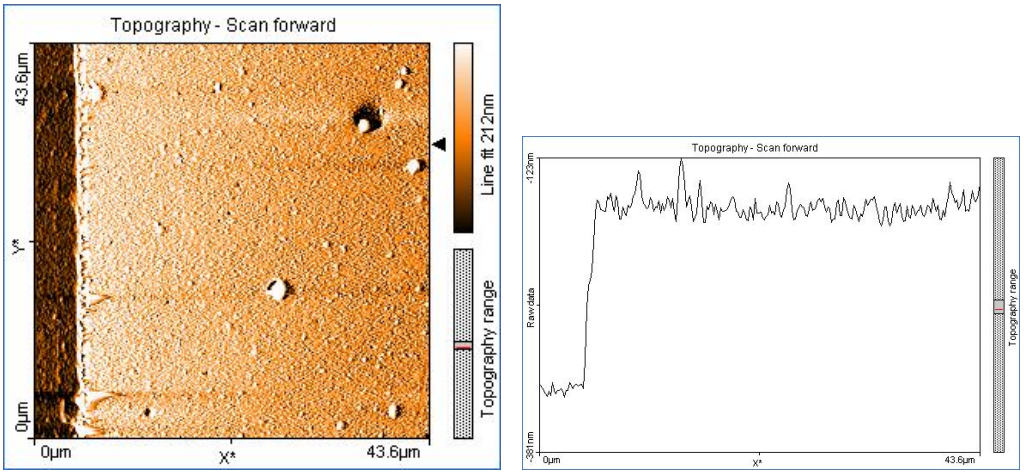

(a) (b)

Figure 8.5: AFM scan showing the step profile of an early PBCO sample intended for use with the alternative G-SQUID design.

profile of the step in Figure 8.5, while better defined, is also unsatisfactory. Step angles varied from 8 – 14 degrees with traces of redeposition in certain areas.

The behaviour of the mill had changed since it was last characterised by Van Staden due to its continuous usage and maintenance. It was concluded that the mill would need to be recharacterised, however, due to the PLD only being available for

two days a week, it was decided not to use PBCO for this task. YBCO was to be tested as a buffer layer, and PBCO would only be returned to if necessary.

Since the buffer layer does not need to be superconductive, oxygen depleted YBCO was next to be tested as a buffer layer. This approach had the benefit of prolonging oxygen reserves. Steps for both G-SQUID designs were tested, however the results were not better, with step angles in the range of 8 – 10 degrees. Oxygen rich YBCO yielded inconsistent results, with step angles ranging from 10 to approximately 40 degrees when etched under identical conditions. Characterising the mill was made difficult due to the fact that parts of the mill was continually being maintained and improved during the process, voiding many of the results. Before the characterisation process could be completed, a fundamental problem with the G-SQUID designs were identified which made the use of step-edge junctions impractical. This problem is further discussed in Section 8.3. The decision was made to focus on bridge constriction junctions instead, and further characterisation was not performed.

8.2.2 Bridge Constriction Junctions

As mentioned in Chapter 7.5.2, the two approaches used in bridge constriction junction fabrication involved the use of an AFM to physically scratch the constrictions into the superconducting tracks. Attempting to scratch the YBCO itself yielded no results. Numerous attempts under varying scratching parameters were attempted, yet no change in the surface of the YBCO could be seen. It was concluded that the tip was insufficient for the task, and that a diamond coated tip would be required. Unfortunately, such a tip could not be aquired for the Nanosurf AFM at the time.

Scratching the photoresist before milling the tracks showed initial promise, however this approach was marred by its own problems. The effects of the scratching were very inconsistent. An attempt on a given sample could, for instance, display decent results, whereas another attempt using an identical sample would display no effect at all. Another problem that occurred was that the scans would deteriorate rapidly around the areas where scratching was performed. An example of this is shown in Figure 8.6. This would become particularly problematic when attempting to fine tune a given junction, as the readout would become increasingly unreliable.

The technique also demonstrates a problematic lack of process control. Figure 8.7 shows one of the test samples before and after milling. Three different shapes were scratched into the photoresist. The effect of the milling was far more pronounced than expected around the scratched areas. This lack of predictability, coupled with the glitches that occur around the scratched areas and general inconsistency

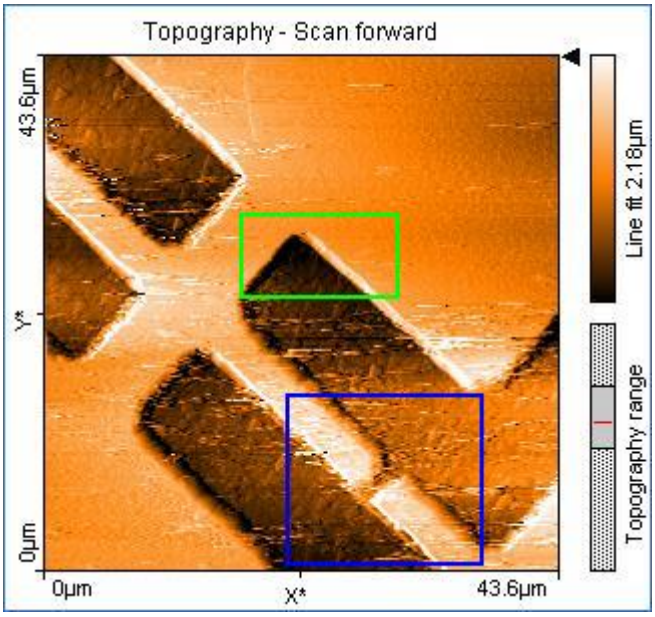

Figure 8.6: An AFM surface scan of a sample in which a constriction junction is scratched. The junction is located in the centre of the blue rectangle, the area of which exhibits significant image noise compared to the area indicated in green.

of the scratching effects, makes it extremely difficult to establish a reproducible process of junction fabrication using AFM lithography.

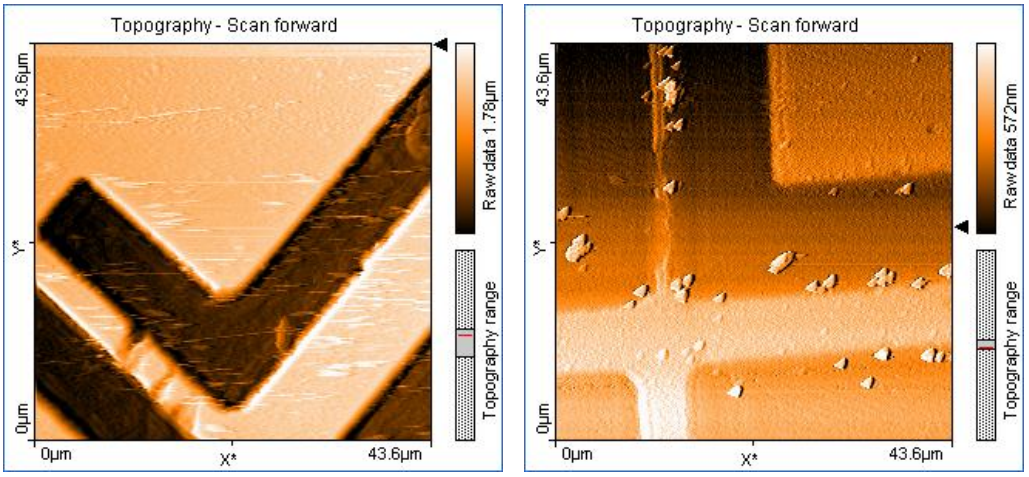

(a) Before milling. (b) After milling.

Figure 8.7: One of the scratching test samples before and after milling.

It should be noted that many of the photoresists and developers used were already past their expiry dates. This may have contributed towards the inconsistency of

the scratching effects. Nonetheless, the process does show promise, however it will require a greater amount of characterisation than could be applied in this work.

8.3 Gradiometer Designs

The two gradiometer designs, while viable in their own right, presented a problem during the photolithography process. Certain alignments necessary for Josephson junction creation, as well as silver pad deposition, require a higher level of alignment control than the existing UV exposure machine can provide.

The original G-SQUID design requires a rectangular step to be milled into the underlying substrate/buffer layer into which the inner part of the SQUID loop is to be aligned, as seen in Figure 5.7. When performing this alignment, the substrate must be brought as close to the mask as possible without touching it. The focus of the microscope must then be adjusted between two levels in order to focus on the mask and the substrate respectively. Figure 8.8 shows the differences between the two levels of focus. The step is located to the upper left of the SQUID loop. It

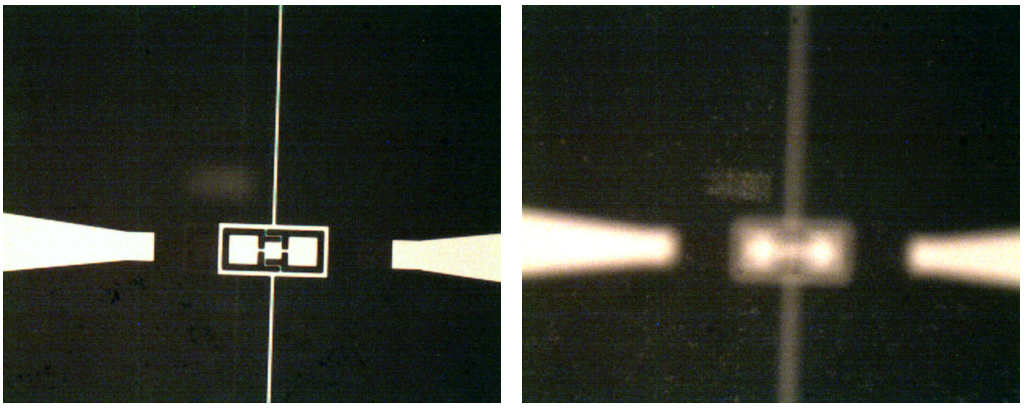

(a) (b)

Figure 8.8: The difference between the two levels of focus required when aligning the circuit pattern with the step. The incorrect version of the G-SQUID was unintentionally used in this alignment, however the purpose of the image was to demonstrate the difficulty of the alignment, which is still the same.

is already barely visible, even when in focus, however the greater problem lies in the loss of edge definition when the focus is shifted. If the step is in focus, then it becomes impossible to determine where exactly the edges of the mask pattern begins and ends. The blurring effect also makes it difficult to see the step in the substrate as it is brought closer to the pattern edge. In Figure 8.9, the step has been moved to directly under the centre part of the pattern. Here the step needs to be

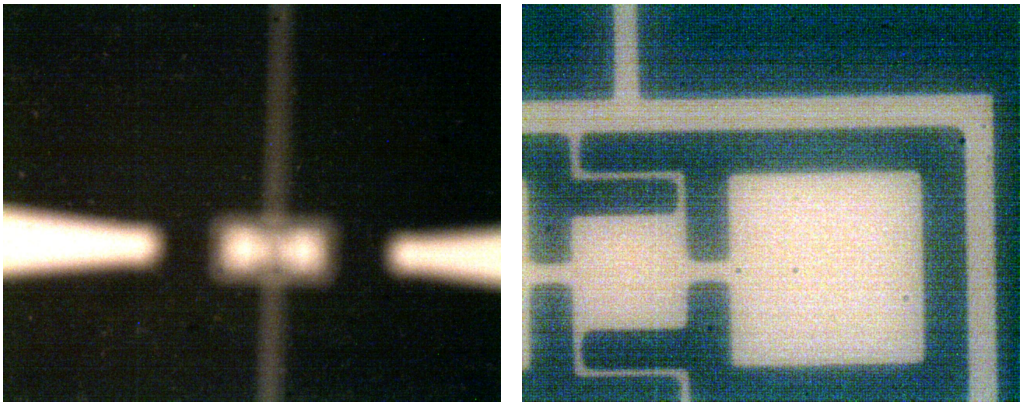

(a) (b)

Figure 8.9: Here the step is directly below the pattern in the centre. The blurring effect renders proper alignment of the step to the pattern impossible. Even at higher magnification the step cannot be seen.

aligned as indicated by the broken line in Figure 5.7, however the blurring effect renders this task impossible as the step is entirely obscured. Even at the highest level of magnification, the step cannot be seen. Improper alignment will result in asymmetry, as well as the possibility of Josephson junctions forming on tracks that were not meant to cross the steps.

The same problem is present with the alternative G-SQUID design as shown in Figure 8.10. In this case, the step must remain in the centre of the two tracks that

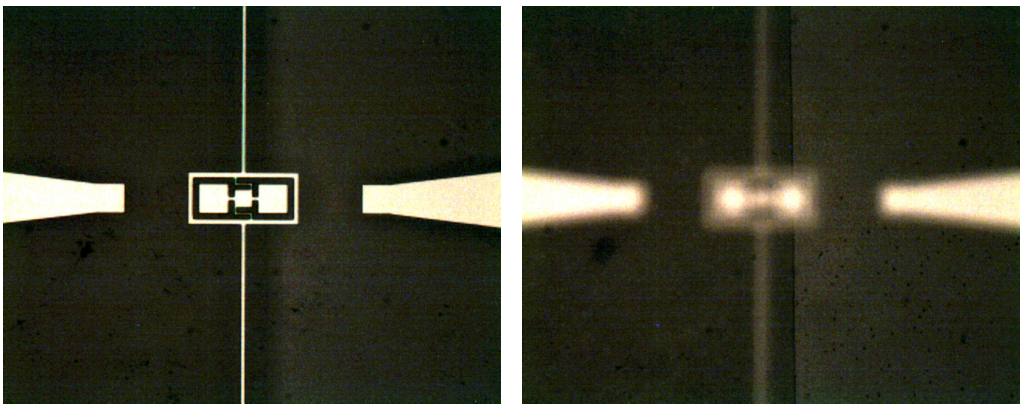

(a) (b)

Figure 8.10: The alternative G-SQUID design is also affected by the same problem. Here the step must remain in the centre of the two tracks that connect the SQUID loop to the pickup loop. The step is currently shown crossing the rightmost pad.

connect the SQUID loop to the pickup loop. These tracks are only 8 μm wide. An unreasonable amount of effort is required to ensure that the step remains in the

centre of the tracks throughout the width of the entire substrate, which is already made difficult due to the loss of edge definition. The alternative G-SQUID design was originally intended for use with bicrystal substrates, however, due to the alignment difficulties and the high cost of such substrates, a bicrystal SQUID was not attempted.

These problems resulted in the G-SQUID designs only being reproducibly usable with constriction junctions. Nonetheless, a number of attempts using step-edges were made and was meant to be tested, however a final hurdle was encountered that rendered both step-edge and constriction samples untestable. Normally, silver pads are deposited using a copper mask. The 50×50 μm pads located inside the SQUID loops of both G-SQUID designs are too small, therefore, photolithography had to be used to create the mask. Unfortunately, the same edge definition

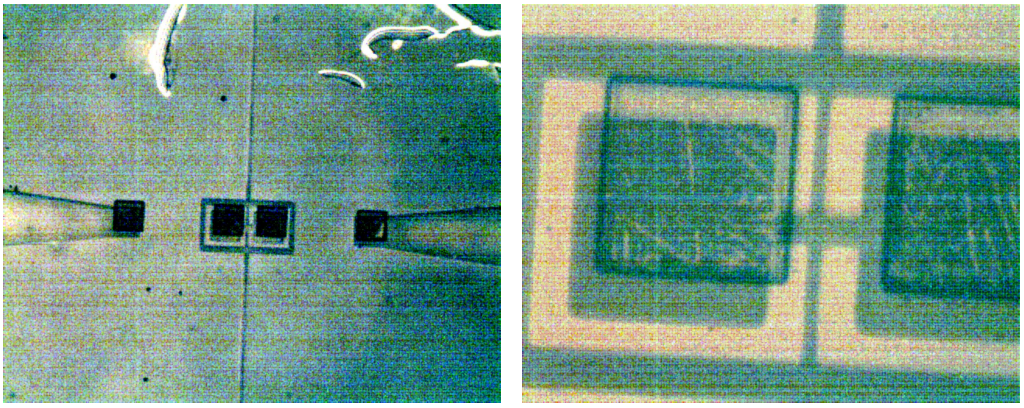

(a) (b)

Figure 8.11: The result of attempting to align the mask required for silver pad deposition with the YBCO pattern.

problem occured. The problem was made worse due to the fact that the chrome shadow mask was entirely reflective except where the pads were located. This resulted in the image from the microscope being oversaturated from the reflected light, leaving the small dark areas underexposed, making it even more difficult to see the substrate beneath the mask. Figure 8.11 shows the best of numerous attempts to align the mask with the pads. The pads still made contact with the SQUID loop, rendering the result unusable. A proper alignment would be accidental at best. Reproducible results could not be obtained.

Chapter 9

Conclusions and Recommendations

Despite not being able to fabricate a fully functional device as set forth by the project goals, the simulations show a definite viability of the device. Many areas have been identified where improvements can be made, both in the design and manufacturing processes.

The designs of the G-SQUID, despite the problems discussed in Chapter 8.3, can still be used to manufacture a gradiometer. If a reproducible method of constriction junction creation can be ensured, then the original G-SQUID design is still suitable without modification. The alternative design can be improved by widening the two tracks that connect the SQUID loop to the pickup loop, allowing for a greater margin of error when attempting to align a step or bicrystal boundary along the centre.

Many aspects of the manufacturing processes need to be reviewed. At the time of writing, a new substrate holder has been designed for the ICM which will allow consistent YBCO depositions without the need for silver paste. This improvement alone should already greatly improve the number of successful YBCO films per deposition. Another improvement that is currently being implemented is an alternative chamber meant exclusively for the deposition of metals. Dedicating an ICM chamber to YBCO and PBCO deposition, or at least minimising the amount of materials that are allowed to be sputtered in a given chamber, will minimise the possibility of contaminants and inconsistencies during deposition. The possibility of equipping the chamber for RF sputtering should also be revisited, as it would make research into buffer layer usage much easier.

It is heavily recommended that the expired photoresists and developers be replaced if possible. This is not too urgent an improvement as the existing photoresists still perform adequately for pattern etching where edge profiles are not impor-

tant, and certain photoresists can be rather expensive. However, it will be required if constriction junctions using AFM lithography is to become a reality. Despite not being successful in this work, AFM lithography is a very promising prospect, as it would make the creation of constriction junctions much easier than having to rely on an outside department's laser. However, this will require consistent, reliable performance of the photoresist, something that cannot be guaranteed if the photoresist and developers are past their expiry dates.

Finally, the argon ion mill will have to be recharacterised. It should, however, be kept in mind that the current fabrication system as a whole is constantly being altered and improved, and even the slightest change, or simply routine maintenance, may greatly alter the characteristics of any given system in the fabrication process. Any given system should be periodically tested to see if it performs as expected.

Success in a project such as this will rely on proper planning. When designing a SQUID, it is best not to spend too much time on the electronics until a working SQUID has been created. This was one of the failure points of this project. Had more time been spent focusing on the manufacturing processes, it may have been possible to achieve reproducible Josephson junctions for the G-SQUID designs.

Nonetheless, achieving a working SQUID at the University of Stellenbosch is merely a matter of time and a methodical approach. The facilities available at the Engineering Faculty make the creation of a SQUID without the reliance on outside departments a definite reality.

Appendices

Appendix A

Gradiometer Schematics

This appendix contains the schematics of the two G-SQUID designs, as well as that of the pickup and feedback loops.

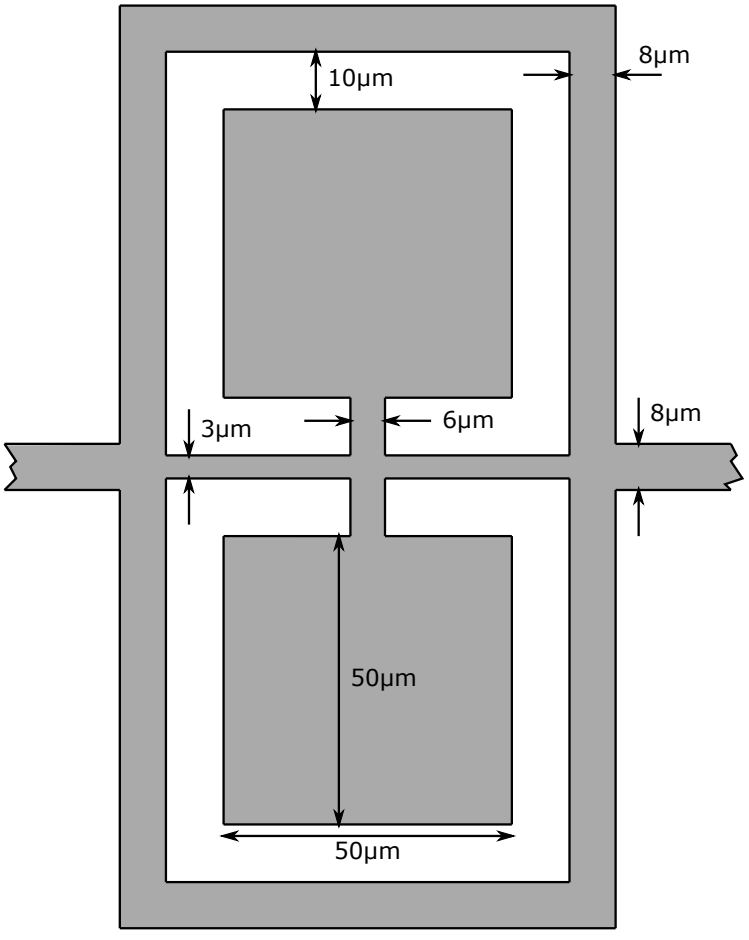

Figure A.1: Dimensions of the original G-SQUID design. The tracks extending toward the left and right connect the SQUID loop to the pickup loop.

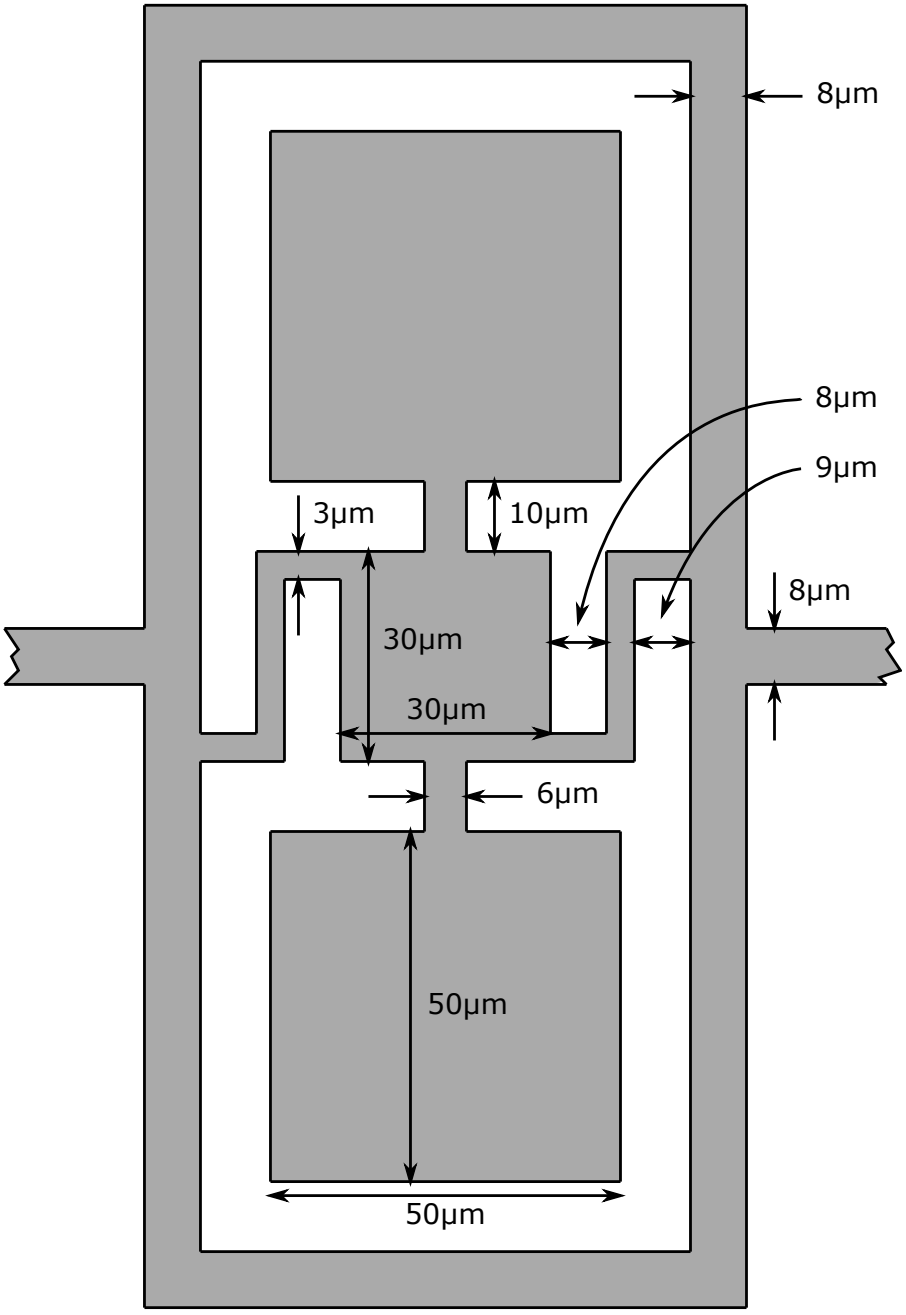

Figure A.2: Dimensions of the variant G-SQUID design. The tracks extending toward the left and right connect the SQUID loop to the pickup loop.

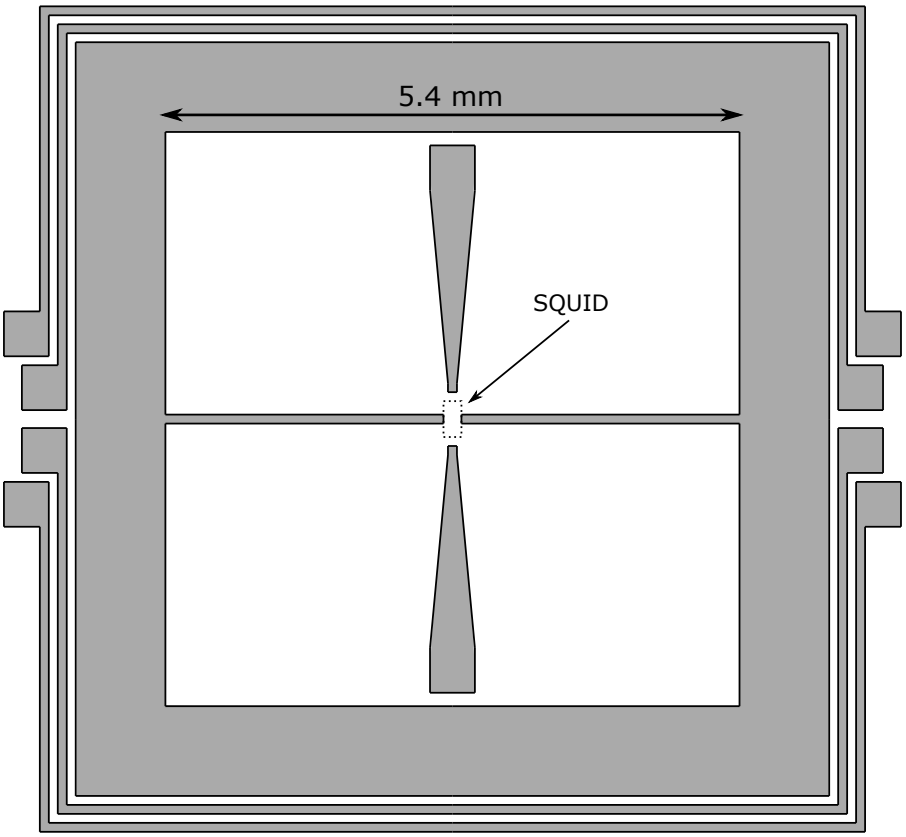

Figure A.3: Schematic of the pickup and feedback loops. The outermost and innermost feedback loops are used for the APF and the FLL respectively. Either SQUID is located in the centre of the layout.

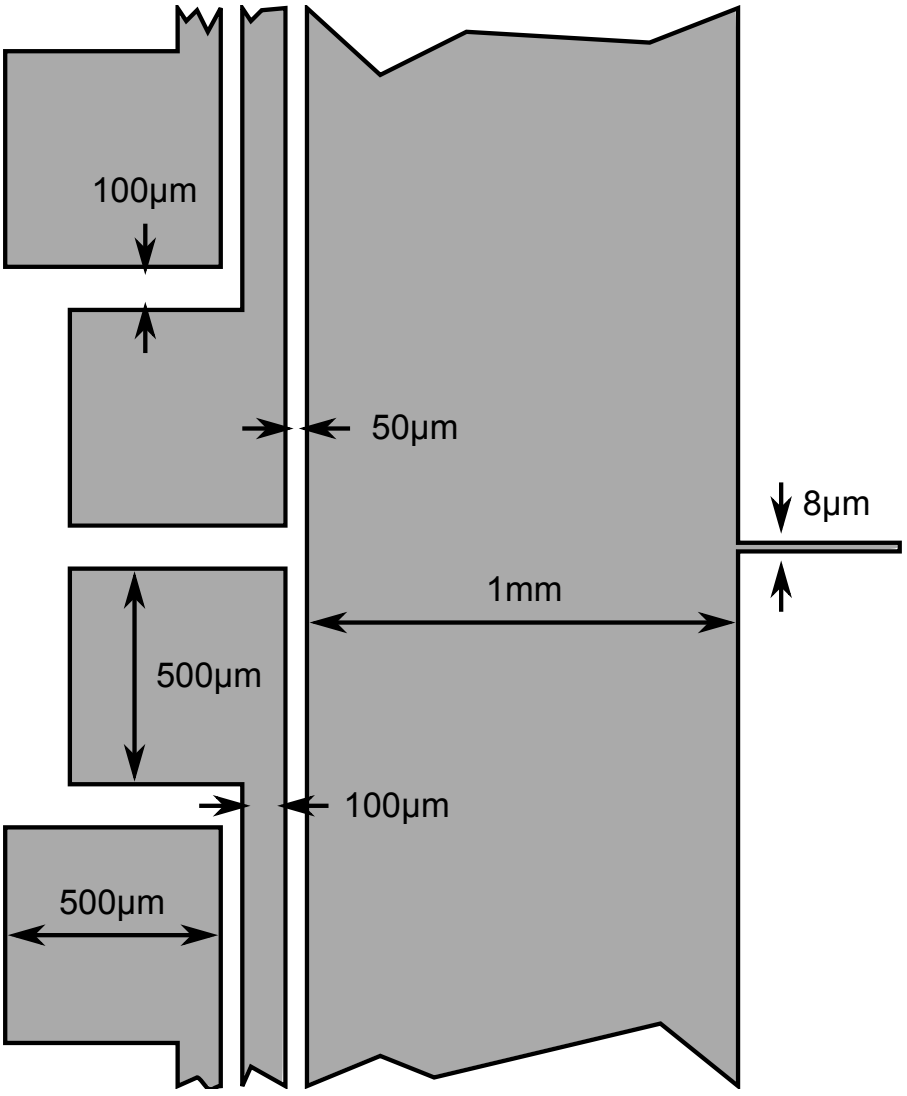

Figure A.4: Dimensions of the pickup and feedback loops, as well as the connection pads. The track extending to the right connects the pickup loop to the SQUID loop. Both feedback loops are 100 μm wide and 50 μm apart. The pickup loop is 1 mm wide.

Appendix B

WRSPICE Code

B.1 Flux-locked Loop Proof of Concept

```
Gradiometer Draft

*Gradiometric SQUID utilised. Parameters updated. APF included.

*Primary Excitation to Pickup Loops
Iext1 0 1 pwl(0 0 500n 10m 1000n 0 1500n 10m 2000n 0 2500n 10m
+3000n 0 3500n 10m 4000n 0)
Iext2 0 2 pwl(0 50u 5n 0 505n 10m 1005n 0 1505n 10m 2005n 0
+2505n 10m 3005n 0 3505n 10m 4000n 50u)
*Iext1 0 1 sin(0 8.748m 2.5meg 0)
*Iext2 0 2 sin(0 8.748m 2.5meg 9p)
Le1 1 0 10n
Le2 2 0 10n

*Secondary Excitation to SQUID Loops
Iext1s 0 70 pwl(0 0 500n 3.433u 1000n 0 1500n 3.433u 2000n 0
+2500n 3.433u 3000n 0 3500n 3.433u 4000n 0)
Iext2s 0 72 pwl(0 16.38n 5n 0 505n 3.433u 1005n 0 1505n 3.433u
+2005n 0 2505n 3.433u 3005n 0 3505n 3.433u 4000n 16.38n)
*Iext1s 0 70 sin(0 3.003u 2.5meg 0)
*Iext2s 0 72 sin(0 3.003u 2.5meg 238.5f)
Le11s 70 71 5n
Le12s 71 0 5n
Le21s 72 73 5n
Le22s 73 0 5n
```

```
*Pickup Loop
Lp1 200 201 6.54n
Lp2 201 200 6.54n
Lpl 200 3 4.51n
Lpr 4 201 4.51n

*SQUID
Ib1 0 5 DC 112.5u
Ib2 0 6 DC 112.5u
Ls1l 3 5 72.23p
Ls1r 5 4 72.23p
Ls2l 6 3 72.23p
Ls2r 4 6 72.23p
Lsl 3 100 30.12p
Lsr 4 102 30.12p
Bl 100 0 ybco
Br 102 0 ybco

*APF
Ra 5 400 5
La1 400 0 13.54n
La2 0 400 13.54n

*Mutual Inductances
Kep1 Le1 Lp1 1
Kep2 Le2 Lp2 1
Kes11 Le11s Ls1l 1
Kes12 Le12s Ls1r 1
Kes21 Le21s Ls2l 1
Kes22 Le22s Ls2r 1
Kf1 Lf1 Lp1 0.597
Kf2 Lf2 Lp2 0.597
Ka1 La1 Lp1 0.494
Ka2 La2 Lp2 0.494

Efilt 51 0 5 0 1
Rfilt 51 50 50
```

```
Cfilt 50 0 200p

*Readout Electronics
Vbias 300 0 DC -420u
Ef 9 300 5 0 10
Rf 9 10 1
Cf 10 11 10p
Efb 11 0 0 10 100k
Rf1 11 12 200
Lf1 12 0 13.18n
Lf2 0 12 13.18n

.model ybco jj(rtype=1, cct=1, icon=10m, vg=2.8m, delv=0.08m,
+icrit=100u, r0=1, rn=1, cap=0.1p)

.tran 1ns 4us UIC

.end
```

B.2 Output Bandpass Filter

```
Buttorworth Bandpass Filter, 50Hz, Q = 10, K = 2

Vin 1 0 AC 1

Vp 98 0 DC 10
Vn 99 0 DC -10

R1 1 2 15.915k
R2 2 0 160.763
R3 3 4 63.662k

*R1 1 2 2k
*R2 2 0 20k
*R3 3 4 7k

C1 2 3 1u
C2 2 4 1u
```

```
X1 0 3 98 99 4 LF351N



* Opamp LF351N, National Semiconductour, JFET, Wideband ft=4MHz
*LF351 Wide Bandwidth JFET-Input OP-AMP MACRO-MODEL
*
* connections:    non-inverting input
*                 |   inverting input
*                 |   |   positive power supply
*                 |   |   |   negative power supply
*                 |   |   |   |   output
*                 |   |   |   |   |
*                 |   |   |   |   |
.SUBCKT LF351N    1   2  99  50  28
*
*Features:
*Low supply current =               1.8mA
*Wide bandwidth =                   4MHz
*High slew rate =                  13V/uS
*Low offset voltage =               10mV
*
*INPUT STAGE
*
IOS 2 1 25P
*^Input offset current
R1 1 3 1E12
R2 3 2 1E12
I1 99 4 100U
J1 5 2 4 JX
J2 6 7 4 JX
R3 5 50 20K
R4 6 50 20K
*Fp2=12 MHz
C4 5 6 3.31573E-13
*
*COMMON MODE EFFECT
```

```
*
I2 99 50 1.7MA
*^Quiescent supply current
EOS 7 1 POLY(1) 16 49 5E-3 1
*Input offset voltage.^
R8 99 49 50K
R9 49 50 50K
*
*OUTPUT VOLTAGE LIMITING
V2 99 8 2.13
D1 9 8 DX
D2 10 9 DX
V3 10 50 2.13
*
*SECOND STAGE
*
EH 99 98 99 49 1
F1 9 98 POLY(1) VA3 0 0 0 1.0985E7
G1 98 9 5 6 1E-3
R5 98 9 100MEG
VA3 9 11 0
*Fp1=40.3 HZ
C3 98 11 39.493P
*
*POLE STAGE
*
*Fp3=42 MHz
G3 98 15 9 49 1E-6
R12 98 15 1MEG
C5 98 15 3.7894E-15
*
*COMMON-MODE ZERO STAGE
*
G4 98 16 3 49 1E-8
L2 98 17 31.831M
R13 17 16 1K
*
*OUTPUT STAGE
```

```
*
F6  99 50 VA7 1
F5  99 23 VA8 1
D5  21 23 DX
VA7 99 21 0
D6  23 99 DX
E1  99 26 99 15 1
VA8 26 27 0
R16 27 28 35
V5  28 25 0.1V
D4  25 15 DX
V4  24 28 0.1V
D3  15 24 DX
*
*MODELS USED
*
.MODEL DX D(IS=1E-15)
.MODEL JX PJF(BETA=1.25E-5 VTO=-2.00 IS=50E-12)
*
.ENDS



.AC lin 1000 1 100

.END
```

Appendix C

FastHenry Code

C.1 Original G-SQUID

```
*Gradiometric SQUID Loop - SEJ Design
.units um
.default z=0 h=0.2
.default nhinc=5 nwinc=7
.default lambda=0.14

*SQUID
n1 x=0 y=0
n2 x=18 y=0
n3 x=39 y=0
n4 x=39 y=75.5
n5 x=-39 y=75.5
n6 x=-39 y=0
n7 x=-39 y=-75.5
n8 x=39 y=-75.5
n9 x=-18 y=0
n10 x=-0.01 y=0
n11 x=0 y=11.5
n12 x=0 y=61.5
n13 x=-0.01 y=-11.5
n14 x=-0.01 y=-61.5
* Pickup Loop
n15 x=3200 y=0
n16 x=3200 y=3200
n17 x=-3200 y=3200
```

```
n18 x=-3200 y=0
n19 x=-3200 y=-3200
n20 x=3200 y=-3200
* Feedback Upper
n21 x=3800 y=50
n22 x=3800 y=3800
n23 x=-3800 y=3800
n24 x=-3800 y=50
* Feedback Lower
n25 x=-3800 y=-50
n26 x=-3800 y=-3800
n27 x=3800 y=-3800
n28 x=3800 y=-50
* APF Upper
n29 x=3950 y=650
n30 x=3950 y=3950
n31 x=-3950 y=3950
n32 x=-3950 y=650
* APF Lower
n33 x=-3950 y=-650
n34 x=-3950 y=-3950
n35 x=3950 y=-3950
n36 x=3950 y=-650

* SQUID
*e1 n1 n2 w=3
e2 n2 n3 w=3
e3 n3 n4 w=8
e4 n4 n5 w=8
e5 n5 n6 w=8
e6 n6 n7 w=8
e7 n7 n8 w=8
e8 n8 n3 w=8
e9 n6 n9 w=3
*e10 n9 n10 w=3
*e11 n1 n11 w=6
*e12 n11 n12 w=50
*e13 n10 n13 w=6
```

```
*e14 n13 n14 w=50
* Pickup Loop
*e15 n3 n15 w=8
*e16 n15 n16 w=1000
*e17 n16 n17 w=1000
*e18 n17 n18 w=1000
*e19 n18 n19 w=1000
*e20 n19 n20 w=1000
*e21 n20 n15 w=1000
*e22 n18 n6 w=8
* Feedback Loop Upper
*e23 n21 n22 w=100
*e24 n22 n23 w=100
*e25 n23 n24 w=100
* Feedback Loop Lower
*e26 n25 n26 w=100
*e27 n26 n27 w=100
*e28 n27 n28 w=100
* APF Upper
*e29 n29 n30 w=100
*e30 n30 n31 w=100
*e31 n31 n32 w=100
* APF Lower
*e32 n33 n34 w=100
*e33 n34 n35 w=100
*e34 n35 n36 w=100

*.external n2 n3
*.external n6 n9
*.external n3 n6
*.external n3 n15
*.external n6 n18
*.external n15 n18
.external n2 n9
*.external n21 n24
*.external n29 n32

.freq fmin=10e9 fmax=10e9 ndec=1
```

```
.end
```

C.2 Variant G-SQUID

```
*Gradiometric SQUID Loop - BCJ Design
.units um
.default z=0 h=0.2
.default nhinc=5 nwinc=7
.default lambda=0.14

n1 x=0 y=75
n2 x=0 y=25
n3 x=0 y=15
n4 x=0 y=0
n5 x=0 y=-15
n6 x=0 y=-25
n7 x=0 y=-75
n8 x=25.5 y=-15
n9 x=25.5 y=13.5
n10 x=39 y=13.5
n11 x=39 y=87
n12 x=-39 y=87
n13 x=-39 y=0
n14 x=-39 y=-13.5
n15 x=-39 y=-87
n16 x=39 y=-87
n17 x=39 y=0
n18 x=-25.5 y=-13.5
n19 x=-25.5 y=15
n20 x=2700 y=0
n21 x=2700 y=2700
n22 x=-2700 y=2700
n23 x=-2700 y=0
n24 x=-2700 y=-2700
n25 x=2700 y=-2700
n26 x=25.5 y=0
n27 x=-25.5 y=0
```

```
*e1 n1 n2 w=50
*e2 n2 n3 w=10
*e3 n3 n4 w=30
*e4 n4 n5 w=30
*e5 n5 n6 w=10
*e6 n6 n7 w=50
*e7 n5 n8 w=3
*e8 n8 n26 w=3
e9 n26 n9 w=3
e10 n9 n10 w=3
e11 n10 n11 w=8
e12 n11 n12 w=8
e13 n12 n13 w=8
e14 n13 n14 w=8
e15 n14 n15 w=8
e16 n15 n16 w=8
e17 n16 n17 w=8
e18 n17 n10 w=8
e19 n14 n18 w=3
e20 n18 n27 w=3
*e21 n27 n19 w=3
*e22 n19 n3 w=3
*e23 n17 n20 w=6
*e24 n20 n21 w=1000
*e25 n21 n22 w=1000
*e26 n22 n23 w=1000
*e27 n23 n24 w=1000
*e28 n24 n25 w=1000
*e29 n25 n20 w=1000
*e30 n23 n13 w=6

.external n26 n27
.freq fmin=10e9 fmax=10e9 ndec=1
.end
```

Bibliography

[1] Yves Pauleau, editor. *Materials Surface Processing by Directed Energy Techniques*. Elsevier Ltd, 2006.

[2] I. K. Kominis, T. W. Kornack, J. C. Allred, and M. V. Romalis. A subfemtotesla multichannel atomic magnetometer. *Nature*, 422:596–599, April 2003.

[3] P. J. Ford and G. A. Saunders. *The Rise of the Superconductors*. CRC Press, 2004.

[4] V. L. Ginzburg and E. A. Andryushin. *Superconductivity*. World Scientific, 1994.

[5] F. London and H. London. The electromagnetic equations of the supraconductor. *Proceedings of the Royal Society of London*, A149:71–88, March 1935.

[6] Nobelprize.org. http://nobelprize.org/nobel_prizes/physics/laureates/1972/.

[7] Gerald Burns. *High-Temperature Superconductivity, An Introduction*. Academic Press, 1992.

[8] J. G. Bednorz and K. A. Müller. Possible high Tc superconductivity in the Ba-La-Cu-O system. *Zeitschrift für Physik B Condensed Matter*, 64:189–193, 1986.

[9] M. K. Wu, J. R. Ashburn, C. J. Torng, P. H. Hor, R. L. Meng, L. Gao, Z. J. Huang, Y. Q. Wang, and C. W. Chu. Superconductivity at 93 K in a new mixed-phase Y-Ba-Cu-O compound system at ambient pressure. *Physical Review Letters*, 58(9):908–910, March 1987.

[10] Vladimir Z. Kresin, Stuart A. Wolf, and Yu.N. Ovchinnikov. Exotic normal and superconducting properties of the high-T_c oxides. *Physics Reports*, 288:347–354, 1997.

[11] Jeffrey W. Lynn. *High Temperature Superconductivity*, chapter 1. Springer-Verlag, 1990.

[12] V. V. Schmidt. *The Physics of Superconductors*. Springer, 1997.

[13] Michael Tinkham. *Introduction to Superconductivity*. McGraw-Hill International Editions, second edition, 1996.

[14] Vladimir Z. Kresin and Stuart A. Wolf. *Fundamentals of Superconductivity*. Plenum Press, 1990.

[15] Terry P. Orlando and Kevin A. Delin. *Foundations of Applied Superconductivity*. Addison-Wesley Publishing Company, 1991.

[16] A. A. Abrikosov. On the magnetic properties of superconductors of the second group. *Soviet Physics JETP*, 5:1174 – 1182, 1957.

[17] T. van Duzer and C. W. Turner. *Principles of Superconductive Devices and Circuits*. Prentice Hall PTR, second edition, 1999.

[18] Werner Buckel and Reinhold Kleiner. *Superconductivity Fundamentals and Applications*. Wiley-VCH, second edition, 2004.

[19] R. Gross, L. Alff, A. Beck, O. M. Froehlich, D. Koelle, and A. Marx. Physics and technology of high temperature superconducting Josephson junctions. *IEEE Transactions on Applied Superconductivity*, 7(2):2929–2935, 1997.

[20] H. Hilgenkamp and J. Mannhart. Grain boundaries in high-Tc superconductors. *Reviews of Modern Physics*, 74:485–549, 2002.

[21] John Clarke and Alex I. Braginski, editors. *The SQUID Handbook*. WILEY-VCH, 2004.

[22] A. J. Millar, E. J. Romans, C. Carr, A. Eulenburg, G. B. Donaldson, and C. M Pegrum. Step-edge Josephson junctions and their use in HTS single-layer gradiometers. *IEEE Transactions on Applied Superconductivity*, 11(1):1351–1354, March 2001.

[23] P. Seidel, F. Schrey, L. Dörrer, K. Peiselt, F. Schmidl, and C. Steigmeier. Development and investigation of novel single-layer gradiometers using highly balanced gradiometric SQUIDs. *Superconductor Science and Technology*, 15:150–155, 2002.

[24] U. Sinha, P. F. Mcbrien, S. H. Menemma, D. Zhang, D. S. Pinker, Gavin Burnell, Z. H. Barber, and E. J. Tarte. Device fabrication and optimisation for josephson broadband spectroscopy of ferroelectric thin films. *Ferroelectrics*, 329:125–130, 2005.

[25] D. Drung. High-Tc and low-Tc dc SQUID electronics. *Superconductor Science and Technology*, 16:1320 to 1336, October 2003.

[26] NIEHS. Emf questions and answers. http://www.niehs.nih.gov/health/docs/emf-02.pdf, June 2002.

[27] J. D. Glover and M. S. Sarma. *Power System Analysis and Design*. Brooks/Cole, 2002.

[28] C. L. Wadhwa. *Electrical Power Systems*. New Age International, 2006.

[29] K. C. Agrawal. *Industrial Power Engineering and Applications Handbook*. Butterworth-Heinemann, 2001.

[30] Donald A. Neamen. *Electronic Circuit Analysis and Design*. McGraw-Hill, 2001.

[31] Philips Semiconductors. 2N2222; 2N2222A NPN switching transistors datasheet, May 1997.

[32] James W. Nilsson and Susan A. Riedel. *Electric Circuits*. Pearson Prentice Hall, seventh edition, 2005.

[33] Marc J. Madou. *Fundamentals of Microfabrication: The science of miniaturization.* CRC Press, 2 edition, 2002.

[34] B. C. Chung, C. H. Tsai, S. S. Hsu, C. C. Yu, C. H. Lin, and I. N. Lin. Epitaxial-like $Y_1Ba_2Cu_3O_{7-\delta}$ superconducting thin films synthesized by plasma enhanced chemical beam deposition techniques. *Physica C*, 227:357 – 364, July 1994.

[35] S. P. Pai, R. Pinto, P. R. Apte, C. P. D'Souza, A. G. Chourey, and D. Kumar. Oxygen incorporation during *in situ* growth of YBCO films on both sides of substrates. *Bulletin of Materials Science*, 16(6):685 – 692, December 1993.

[36] Neeraj Khare, editor. *Handbook of High-Temperature Superconductor Electronics*. Marcel Dekker, Inc, 2003.

[37] K. S. Sree Harsha. *Principles of Physical Vapor Deposition of Thin Films*. Elsevier Ltd., 2006.

[38] Milton Ohring. *Materials Science of Thin Films*. Academic Press, second edition, 2002.

[39] Zoe H. Barber. The control of thin film deposition and recent developments in oxide film growth. *Journal of Materials Chemistry*, 16:334 – 344, 2005.

[40] C. Blue and P. Boolchand. In situ preperation of superconducting $Y_1Ba_2Cu_3O_{7-\delta}$ thin films by on-axis rf magnetron sputtering from a stoichiometric target. *Applied Physics Letters*, 58:2036 – 2038, May 1991.

[41] Franz J. Giessibl. Advances in atomic force microscopy. *Revies of Modern Physics*, 75:949 – 983, July 2003.

[42] C. P. Foley, E. E. Mitchell, S. K. H. Lam, B. Sankrithyan, Y. M. Wilson, D. L. Tilbrook, and S. J. Morris. Fabrication and characterisation of YBCO single grain boundary step edge junctions. *IEEE Transactions on Applied Superconductivity*, 9(2):4281 – 4284, July 1999.

[43] Akram A. Elkaseh. Fabrication of high-temperature superconducting nanobridges using atomic force microscopy. Master's thesis, University of Stellenbosch, 2006.

[44] W. F. van Staden. The fabrication of PBCO buffered step-edge Josephson junctions. Master's thesis, University of Stellenbosch, December 2006.